
**3-D Time-dependent Simulation of Void formation
in Metallization Structures**

Vom Fachbereich Elektrotechnik und Informationstechnik

der Universität Hannover
zur Erlangung des akademischen Grades

Doktor-Ingenieur

Genehmigte Dissertation

von **DEA-DESS David Dalleau**

geboren am 28 August 1974 in Saint-Denis, Réunion.

2003

1.Referent: Prof. Dr.-Ing. J. Graul

2. Referent: Prof. Dr.-Ing. H. Grabinski

Gutachter: Prof. Y. Danto

Vorsitz: Prof. Dr.-Ing. E. Barke

Tag der Promotion: 02. April 2003

Abstract (*keywords: Void, Simulation, Reliability*)

David, Dalleau

3-D Time-depending Simulation of Void Formation in Metallization Structures.

The reliability of integrated circuits has been of particular interest for the microelectronic industry during the last decades. Today integrated circuits need to have a high quality and should be more reliable due to consumers requirements as well as to their working conditions. In parallel, these requirements lead to the strong integration of microelectronic components followed by an increase in the power per unit area. In this situation, strong current densities, high temperatures and temperature gradients as well as induced thermomechanical stress are able to occur and can lead to the complete destruction of the integrated circuits functions. If the circuits particularly run under severe conditions, the appearance potential of induced degradation phenomena such as the electromigration, the thermomigration as well as the stressmigration on metallization structures becomes important. This can be a problem particularly if these circuits are working in an environment area where reliability remain a fundamental aspect. Consequently, a study of their reliability is imposed.

The investigations in the domain of reliability evaluation for metallization structures are generally performed using accelerated stress tests. Different failure mechanisms appear in the degradation process of the metallization structures depending on their operating conditions until they fail. Nevertheless, a change in the failure mechanism under stress tests conditions compared to normal environment running conditions is expected. The approach consisting in their extrapolation to working conditions may then be wrong. To remedy this problem, an approach by simulation should permit to withdraw the controversy. Also, a better understanding of the different failure mechanisms by void simulation formation is possible.

The aim of this work consist in the study of the time-dependency phenomena of void formation in the metallization structures running under strong conditions (above $1\text{MA}/\text{cm}^2$). The time-depending formation of void is analysed by experimental observations. Some guidelines and some hypothesis about their time-dependent development are extracted. A new method using the finite element analysis is implemented in an algorithm, giving the opportunity to predict the 3-D evolution of void formation within metallization structures running under strong operating conditions. A method to calculate the TTF (Time-To-Failure) is developed based on the use of the maximum value evolution of the massflux divergence when the void growth is simulated. The failure mechanisms appearing during the void formation is simulated with a Meander and a SWEAT structure. For the both structures, the results obtained by the simulation of the void formation are found in good agreement with the experimental observations. Out of the simulations, the TTF of the structures were determined for the first time. Also, the calculated TTF and the results obtained by the measurements show a good correspondence.

The different degradation mechanisms have been identified. The tool offers the possibility to simulate the void formation and to get more information about the matter migration phenomena at the weakest part of the structure. The method can also be used for the optimisation of interconnect structures by comparing their calculated lifetime following different working conditions.

Kurzfassung (Schlagworte: Loch, Simulation, Zuverlässigkeit)

David, Dalleau

3-dimensionale zeitabhängige Simulation von Lochbildung in Metallisierungsstrukturen

Die Bedeutung der Zuverlässigkeit integrierter Schaltungen hat während der letzten Jahrzehnte stark zugenommen. Aufgrund der gestiegenen Anforderungen der Konsumenten an die Leistungsfähigkeit und erschwerten Betriebsbedingungen müssen integrierter Schaltungen heute eine höhere Qualität aufweisen und damit zuverlässiger sein. Parallel steigt die Integrationsdichte mikroelektronischer Komponenten und damit die Leistungsdichte auf dem Chip. Aus diesem Grund werden hohe Stromdichten, hohe Temperaturen und Temperaturgradienten sowie induzierter mechanischer Stress insbesondere in den Metallisierungsstrukturen auftreten, die zum Ausfall der Schaltungen führen können. Das Auftreten derartiger Degradierungsphänomene wird als Elektromigration, Thermomigration und Stressmigration in Metallisierungsstrukturen bezeichnet. Diese Phänomene nehmen im Fall erschwerten Betriebsbedingungen wie z.B. in der automotiven Elektronik zu und die Zuverlässigkeit muß als fundamentaler Aspekt berücksichtigt werden.

Die Zuverlässigkeitsuntersuchung von Metallisierungsstrukturen wird im allgemeinen mit Hilfe von beschleunigten Belastungstests durchgeführt. In Abhängigkeit von den Belastungsbedingungen führen unterschiedliche Fehlermechanismen zur Degradierung der Metallisierungsstrukturen. Ein Wechsel der Fehlermechanismen unter höherer Belastungsbedingung im Vergleich zu Betriebsbedingungen ist deshalb möglich. Die Extrapolation der Ergebnisse der Belastungstest zur Einschätzung der Ergebnisse unter Betriebsbedingungen ist in diesem Fall fehlerbehaftet. Mit Hilfe von zeitabhängigen Simulationen kann eine Differenzierung der verschiedenen Fehlermechanismen erfolgen.

In dieser Arbeit wird die Zeitabhängigkeit der Materialwanderung in Metallisierungsstrukturen bei hohen Belastungen (mehr als $1\text{MA}/\text{cm}^2$) untersucht. Die zeitabhängige Lochbildung wird mit Hilfe von experimentellen Untersuchungen verifiziert. Richtlinien und Hypothesen zur zeitabhängigen Simulation der Lochbildung wurden extrahiert. Ein neuer Algorithmus zur Lochbildungssimulation wurde unter zur Hilfenahme der Finite Element Methode entwickelt. Damit kann die 3-dimensionale Lochentwicklung in Metallisierungsstrukturen unter starken Belastungen vorhergesagt werden. Eine neue Methode zur Berechnung der Lebensdauer der Metallisierungsstrukturen wird ebenfalls eingesetzt und damit die Entwicklung der Massenflussdivergenzwerte während der Lochbildungssimulation berücksichtigt.

Der Einfluss der Fehlermechanismen während der Lochentwicklung wurde anhand einer Mäander- und eine SWEAT-Struktur untersucht. In beiden Fällen wurde die Simulation der Lochentwicklung im Vergleich zum experimentellen Ergebnis erfolgreich verifiziert. Dabei wurden die unterschiedlichen Migrationsmechanismen abhängig vom Belastungsstrom bestimmt. Die Lebensdauer der Strukturen wird dabei erstmals aus den simulierten Daten mit guter Übereinstimmung zum Experiment bestimmt.

Das Programm bietet die Möglichkeit 3-dimensionale Lochbildungen in Metallisierungsstrukturen zu simulieren, und präsentiert mehr Informationen über das Materialwanderungsphänomen am Fehlerort. Die präsentierte Methode kann im Rahmen der Optimierung von Metallisierungsstrukturen im Vergleich zu den gerechneten Werten der Lebensdauer unter unterschiedlichen Belastungsbedingungen verwendet werden.

CONTENTS

| | |
|--|----|
| Abbreviations and symbols directory | I |
| Introduction | 1 |
| 1 Reliability experiment results and diffusion mechanisms induced failure | 4 |
| 1.1 Reliability experiments..... | 4 |
| 1.1.1 Reliability test procedure: accelerated ageing test method for metallization structures..... | 4 |
| 1.1.2 Geometry description of the investigated samples..... | 5 |
| 1.1.3 Experimental observations and measurement results..... | 7 |
| 1.2 Diffusion mechanisms in aluminum metallization structures..... | 10 |
| 1.2.1 Bulk diffusion mechanisms..... | 10 |
| 1.2.2 Surface and interface diffusion..... | 11 |
| 1.2.3 Grain boundary diffusion..... | 12 |
| 2 Theoretical background of matter migration in interconnects | 14 |
| 2.1 Physical aspects of migration..... | 14 |
| 2.2 Mathematical modelling of ions massflow in interconnects..... | 15 |
| 2.2.1 Modelling of the electromigration..... | 15 |
| 2.2.2 Modelling of the thermomigration..... | 16 |
| 2.2.3 Modelling of the stressmigration..... | 16 |
| 2.2.4 Modelling of the concentration distribution effect..... | 18 |
| 2.3 Time-dependency modelling of the phenomena..... | 19 |
| 2.3.1 Massflow divergence due to the electromigration..... | 19 |
| 2.3.2 Massflow divergence for the thermomigration..... | 19 |
| 2.3.3 Massflow divergence for the stressmigration..... | 20 |
| 2.3.4 Massflow divergence due to the concentration distribution..... | 21 |
| 3 Thermophysical properties of the used materials | 23 |
| 3.1 General physical constants for aluminum..... | 23 |
| 3.2 Thermophysical properties investigations of the used materials..... | 24 |

| | | |
|----------|--|-----------|
| 3.2.1 | The effective charge number Z^* for aluminum..... | 24 |
| 3.2.2 | The specific heat of transport Q^* for aluminum..... | 25 |
| 3.2.3 | The self-diffusion coefficient D_0 for aluminum..... | 26 |
| 3.2.4 | The activation energy E_A for aluminum..... | 27 |
| 3.3 | Aluminum thin films electrical characterization of the samples..... | 29 |
| 3.4 | Thermal conductivities of the used materials..... | 30 |
| 3.5 | Mechanical and thermomechanical properties of the used materials..... | 31 |
| 4 | Static analysis and failure location determination..... | 32 |
| 4.1 | Static analysis flowchart for the massflux divergence value distribution..... | 32 |
| 4.2 | Thermoelectrical behaviour analysis by FEM..... | 34 |
| 4.2.1 | Influence of the current density on the metallization temperature... .. | 37 |
| 4.2.2 | Influence of the current density on the temperature gradient in the metallization structure..... | 37 |
| 4.2.3 | Influence of the temperature on the electrical parameters..... | 38 |
| 4.3 | Thermomechanical simulation over the metallization structures..... | 39 |
| 4.3.1 | Thermomechanical simulation of the structures..... | 40 |
| 4.3.2 | Determination of the gradient of the thermomechanical hydrostatic stress..... | 41 |
| 4.3.3 | Influence of the applied current on the thermomechanical stress..... | 42 |
| 4.4 | Failure location determination over the investigated structures..... | 44 |
| 4.5 | Influence of the different migration effects..... | 46 |
| 5 | Study of the time-dependency: development of a void formation simulator..... | 49 |
| 5.1 | Analysis of the experimental observations..... | 49 |
| 5.2 | Experimental based extracted guidelines and simulation method..... | 50 |
| 5.3 | Method description of the void formation simulation..... | 51 |
| 5.4 | Time-dependency calculation of the void simulation..... | 54 |
| 5.5 | Time-dependency algorithm presentation of void simulation..... | 56 |
| 5.6 | Algorithm implementation on computing systems for simulation..... | 58 |
| 6 | 3-D Time-dependent void simulation formation in metallization structures..... | 59 |
| 6.1 | Void formation simulation for the meander structure..... | 59 |
| 6.2 | Analysis of the different migration mechanisms during the void simulation growth..... | 64 |

| | | |
|----------|--|-----------|
| 6.3 | Time-dependence determination of the electrical resistance evolution..... | 66 |
| 6.4 | Comparison of the calculated TTF with experimental results..... | 68 |
| 6.5 | Variation of the number of deleted element during void growth simulation.. | 69 |
| 6.6 | Influence of the physical parameters on the calculated TTF..... | 70 |
| 6.6.1 | Variation of the substrate temperature..... | 70 |
| 6.6.2 | Influence of Q^* , Z^* and E_A on the calculated TTF..... | 71 |
| 6.7 | Time-dependent investigations on the SWEAT structure..... | 73 |
| 6.7.1 | Void formation simulation over the SWEAT structure..... | 74 |
| 6.7.2 | Analysis of the different migration mechanisms during the void growth..... | 76 |
| 6.7.3 | Electrical characteristic under different load..... | 78 |
| 6.7.4 | Comparison of the lifetime calculation with measurement results... | 79 |
| 6.8 | Discussion of the simulation results..... | 80 |
| 7 | Integration of the simulation results in the reliability modelling..... | 81 |
| 7.1 | Matter migration induced failure degradation law for electromigration..... | 81 |
| 7.2 | Integration of the characterisation results in the reliability modelling..... | 82 |
| | Conclusion..... | 85 |
| | Zusammenfassung..... | 89 |
| | References..... | 93 |

Abbreviations and symbols directory

Abbreviations

| | |
|--------------------------------|--|
| AMD | Advanced M icro D evelopments |
| Al | Aluminum |
| Al ₂ O ₃ | Aluminum O xide |
| a.u. | Arbitrary U nit |
| avg | Average |
| APDL | Ansys P arametric D esign L anguage |
| CTE | C oefficient of T hermal E xpansion |
| Cr | Chrome |
| Cu | Copper |
| DOS | D isk O perating S ystem |
| ESD | E lectrical S tatic D ischarge |
| FEM | F inite E lement M ethod |
| IC | I ntegrated C ircuit |
| Max | Maximum |
| MB | Megabytes |
| Min | Minimum |
| Mg | Magnesium |
| MTF | M ean T ime-to- F ailure |
| Ni | Nickel |
| PC | P ersonal C omputer |
| RAM | R andom A ccess M emory |
| SEM | S canning E lectron M icroscopy |
| Si | Silicon |
| SiO ₂ | Silicon Dioxide |
| SWEAT | S tandard W afer-level E lectromigration A ccelerated T est |
| TCR | T emperature C oefficient of R esistance |
| Ti | Titan |
| TiN | T itan N itride |
| TTF | T ime- T o- F ailure |

| | |
|------|--|
| REM | R aster E lectron M icroscopy |
| VLSI | V ery L arge S cale I ntegration |

Symbols

| | |
|--|---|
| α | Temperature coefficient of resistivity |
| α_l | Coefficient of thermal expansion |
| $\beta, \gamma, \varphi, \chi$ | User defined constants |
| d | Grain length |
| δ | Grain width |
| D | Diffusion coefficient |
| D_0 | Self-diffusion coefficient |
| $Divja$ | Massflux divergence value of the electromigration |
| $Divth$ | Massflux divergence value of the thermomigration |
| $Divsh$ | Massflux divergence value of the stressmigration |
| $Divtot$ | Massflux divergence value of the all effects |
| e | Electrical charge unit |
| $\varepsilon_{xx}, \varepsilon_{yy}, \varepsilon_{zz}$ | Normal strain components |
| E | Young Modulus |
| \vec{E} | Electrical field |
| E_A | Activation energy |
| F, F_i | Parametric function of the divergence value |
| \vec{F}_{ion} | Direct ionic force |
| \vec{F}_e | "Wind-effect" force |
| \vec{F}_{eff} | Effective force value |
| g, h | Widths of the metallization structure |
| $gradN$ | Atomic concentration gradient |
| $gradT$ | Temperature gradient |
| H_f, H_m | Molar enthalpies |
| I | Electrical current |
| \vec{j} | Local current density vector |

| | |
|---|---|
| \vec{J}_A | Massflux of the electromigration |
| \vec{J}_C | Massflux due to the atomic concentration distribution |
| \vec{J}_S | Massflux of the stressmigration |
| \vec{J}_{th} | Massflux of the thermomigration |
| \vec{J}_{Tot} | Total massflux vector |
| κ | Thermal conductivity |
| k_B | Constant of Boltzmann |
| K_{corr} | Correction factor |
| l, l_0 | Length |
| N, N_0 | Atomic concentration |
| ν | Poisson ratio |
| Ω | Atomic volume |
| Q^* | Specific heat of transport |
| ρ, ρ_0 | Specific electrical resistivity |
| R, r | Radius |
| R_n | Reduced electrical resistance of interconnects |
| R_0 | Room temperature electrical resistance |
| R_b, R_i, R_f | Electrical resistance |
| σ | Mean value of the surface of ions diffusion |
| σ_H | Mechanical hydrostatic stress |
| σ_l | Critical mechanical stress level |
| σ_{th} | Thermomechanical induced stress |
| σ_v | Mechanical stress (Von Mises) |
| $\sigma_{xx}, \sigma_{yy}, \sigma_{zz}$ | Mechanical normal component stress |
| S_t | Mechanical stress tensor |
| τ | Mean value of the transition time |
| $\tau_{xy}, \tau_{yz}, \tau_{zx}$ | Mechanical shear component stress |
| T, T_0 | Temperature |
| T_s | Substrate temperature |

| | |
|--------------------|--|
| T_i | Volumetric element deletion time |
| u, v, w | Displacements respectively in the x, y, and z directions |
| V | Electrical potential |
| v_l | Mean value of the electron velocity |
| Z^* | Effective charge number |
| Z, K, S, P | User defined constants |
| Z_{dir}, Z_{ion} | Direct atomic charge number |

Introduction

During the past decades, the microelectronic technology has been among one of the fastest growing technology of the industry. Several factors have contributed to this expansion, such as the development of telecommunication technologies, the large integration of services, the strong diversification in computer technologies, the massive presence of electronic systems within the automation process of production, the massive use in the automobile industry, etc...

Obviously, microelectronic is a fully integrated part of technology in the society. Its relation with today's human life is now established. Moreover, the tremendous use of electronic systems has incited the industry to integrate them as better as possible. This philosophy has conducted to a decrease of areas and dimensions in the integrated system, where all the integrated components such as the sensors, the signal amplifiers, the information processing circuits and the converters are integrated in a single chip and living together within a thin silicon layer. The operating conditions of load such as the voltage supply, the need in the amount of electrical current, and the constant increase of the utilisation frequency have an important impact in the dissipated energy of the chip. In parallel, the conditions of use (submarine, ground or spatial environments) can sometimes affect the functionality of complex integrated systems. The massive integration of components in thin single layers induces high current density in the metallization structures, followed by an increase of their running temperature as well as a strong level of power density on the chip. As a consequence, the degradation of the metallization structure by electromigration is possible. Furthermore, the use of materials with different thermophysical properties induces the presence of high temperature gradients inducing a degradation of the metallization structure due to thermomigration. As a consequence, the effects of these different operating conditions can initiate some mechanical degradation process such as chip delamination, cracks in the interconnection between the chip and the substrate, or more frequently some matter displacement induced failure in chip-level interconnects more known as stressmigration phenomenon. All of these degradation phenomena act negatively on the reliability of the IC systems and have to be taken into account carefully when the systems are designed and developed. In order to predict the reliability of integrated systems under working conditions, the behaviour of these systems are generally studied using accelerated ageing tests. The results of the tests are extrapolated for the evaluation of their reliability under working conditions. This process remains useful although a controversy exists about its reliability

because of the existence of some physical phenomena during the accelerated ageing tests which do not occur when the systems are running under working conditions.

One of the major causes of failure that occur within integrated circuits concerns the matter migration induced failure within chip-level interconnects caused by Electrical Static Discharge (ESD). The increase of the integration rate in the microelectronic components and at interconnect level makes the phenomenon to remain a big concerns for the next coming years. The failure of electrical interconnects is generally caused by the presence of important level of current density at the failure location within them or still due to voiding phenomenon induced by thermomechanical stress. The theory and the modelling of the different effects participating to the degradation phenomenon is known and has been studied experimentally during the last decades. Some studies have been performed to improve the knowledge available and for a better control of the phenomenon. Among them, I.A. Blech demonstrated the existence of a critical length under which the phenomenon of electromigration can be compensated by the effect of mechanical stress driven by diffusional backflows of ions [1]. Moreover, a correlation between grain boundary activities and the Blech length has also been studied to know more about stressmigration in these regions [2]. In addition, several works concerning the influence of temperature and temperature gradients as well as current density distribution and the influence caused by the induced thermomechanical stress have been carried out by the use of FEM calculation over interconnect structures [3,4]. Their effect in the determination of the failure location has been verified by simulation with simplified tested metallization structures. In the same time, the increase in computing capabilities have permitted to approach the degradation phenomenon by simulations [5,6]. Later, some simulations in two and three dimensions area have been performed to study the time-dependency of atomic migration within grain boundaries [7,8]. Until today, the existence of grain boundary regions in chip-level metallization structures remains the most important area of investigation for engineers and scientists and the problem of matter migration induced failure in metallization structures and interconnects is not solved. One of the next challenges in this domain remains the problem of the failure time prediction for systems under normal running conditions and a lot of work is on the way in order to improve the reliability of the interconnects to be implemented within the next generations of integrated circuits.

The improvement of the reliability of products in several domains of the industry is today more studied by the use of computing capacities and simulation. The theory related to

metallization structures degradation of microelectronic systems has been revealed during several past studies. In order to participate to the improvement and to the better understanding of the matter migration induced failure in the integrated circuits, some investigations about the time-dependency of the phenomenon are presented in this work. The work presented here is based on previous results established and based on the static analysis work where the determination of failure location has been performed, taking into account the phenomena of electromigration, the thermomigration and the stressmigration [9].

In the first chapter, the results of reliability experiments over two metallization structures are presented. In the same chapter, the most important diffusion mechanisms induced failure in metallization structures are provided. The following chapter presents the theoretical background of the different effects that act in the degradation phenomenon. The mathematical models defining the massflux due to the phenomena of electromigration, thermomigration and stressmigration are provided and their relationship with the degradation time is given. Then, in the third chapter, the results obtained from an important literature investigation are summarised work, in order to determine the thermophysical properties of the different material used. Furthermore, the application of the method of the massflux divergence distribution for the failure location determination is presented through a non-linear static analysis over a meander and a SWEAT structure. The results are presented in details and a characterisation work to determine the role of the different effect in the degradation process is added. In the following chapter 5, the time-dependency of the phenomenon is studied and a methodology for 3-D void formation simulation based on the path taken by the evolution of the maximum massflux divergence value distribution is suggested. In the same time, an algorithm for the implementation of the simulation methodology is detailed. In chapter 6, the void simulation results for the investigated metallization structures are presented and compared to experimental observations. In addition, the possibility to obtain the evolution of the interconnect electrical resistance by this methodology is provided, which play an interesting role as degradation indicator for metallization structures. Moreover, a methodology to calculate the time-dependency of the void growth is presented and the possibility to determine the Time-To-Failure due to the void growth simulation is given. Also, a comparison between experimental results and observations with the solutions provided by the developed simulation tool is provided. The last chapter is dedicated to the modelling of reliability based on the characterisation work results provided by simulation. A relation resulting on simulation data is exposed and the existing correlation between theory and experiments extracted modelling is discussed.

1. Reliability experiment results and diffusion mechanisms induced failure

The different materials used for the fabrication of metallization structures in very large scale integrated circuits can have an important impact on the reliability of the integrated functions implemented into chips. In this case these different materials need to be well-known and well characterised by the engineers and scientists which are working in the semiconductor industry. These aspects becomes particularly important when the material properties are needed for investigations by the use of simulation.

The goal of this work consists in the development of a simulation tool for the contribution of a better understanding of the degradation phenomenon caused by the appearance of voids in chip-level metallization structures. The simulation tool should predicts the void evolution formation and the development of the corresponding electrical parameters within the metallization structures. The development work is based on the analysis of experimental results and on the interpretation of the experimental observations.

In this chapter, the experiments related to the reliability investigations of two different metallization structures are presented. First, the reliability test procedure used to perform some electromigration accelerated ageing tests is introduced. Then, a geometry description of the test samples themselves is given. Afterwards, the experimental observations on a meander structure being degraded under strong load level are provided. Further, the experimental results for different test conditions such as the determination of the lifetime are exposed. To finish with, the different diffusion mechanisms which take place in the degradation induced failure of chip-level metallization structures will be presented.

1.1 Reliability experiments

1.1.1 Reliability test procedure: accelerated ageing test method for metallization structures

The procedure to evaluate the reliability of the metallization structures is generally made by accelerating the degradation of the samples under strong running conditions. In order to achieve this goal, two different test methods are available: the PLR (Package Level Reliability) test method or the use of the WLR (Wafer Level Reliability) test method. In the case of the PLR investigation, the fabricated samples are simply mounted within a package,

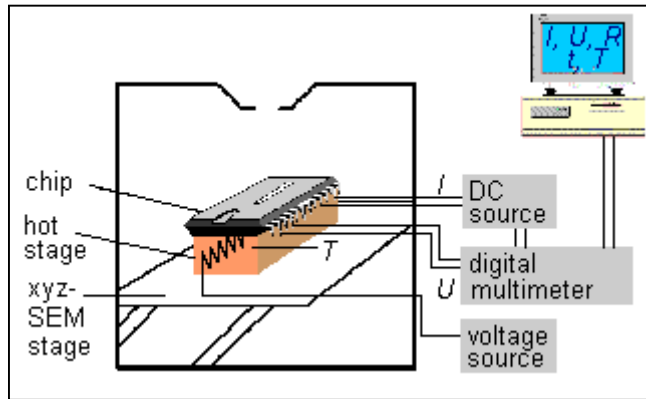


FIGURE 1.1. Accelerated ageing test diagram for metallization structures reliability study.

and the structures are supplied electrically by the package pin interconnections like represented by the picture provided in figure 1.1. During the experiments, a current density average value above $1\text{MA}/\text{cm}^2$ is set within the metallization structures. The temperature of the substrate is generally taken above 100°C , so that the temperature can participate to the

degradation during the accelerated test phase. The samples considered in this work have been tested using the WLR method. In this method, the chip containing the metallization structures is fixed on a substrate where the temperature can be chosen. The supply of the metallization structures is made through the use of switches. In the case of the meander structure, a variation of the substrate temperature was performed by making the test at 180°C , 130°C and 150°C . The applied current was also varied and taken to be 50mA , 70mA , 100mA and 200mA . When the degradation goes on, the migration phenomenon induced voids formation causes a change in the electrical resistance of the metallization. At the location of degradation, the cross-section of the metallization is reduced, and let place to a local temperature elevation. Then, this temperature elevation induces some variation in the resistance evolution of the structure since the electrical resistivity is temperature-dependent. The experiment continues until the electrical interconnection formed by the metallization structure fails. At this time, the electrical interconnection is broken and no more insured, and the corresponding time defines the lifetime or the TTF (Time-To-Failure) for the metallization structure for these particular conditions of load.

1.1.2 Geometry description of the investigated samples

We considered two different structures in our investigation, which were a meander and a SWEAT non-passivated structures. These metallization structures were chosen for their simplicity and their capability to provide strong temperature level as well as important current densities and temperature gradients values for high current densities ($J > 1\text{MA}/\text{cm}^2$). The silicon substrate is $500\mu\text{m}$ thick, on which a thermal silicon dioxide layer was grow. A thick

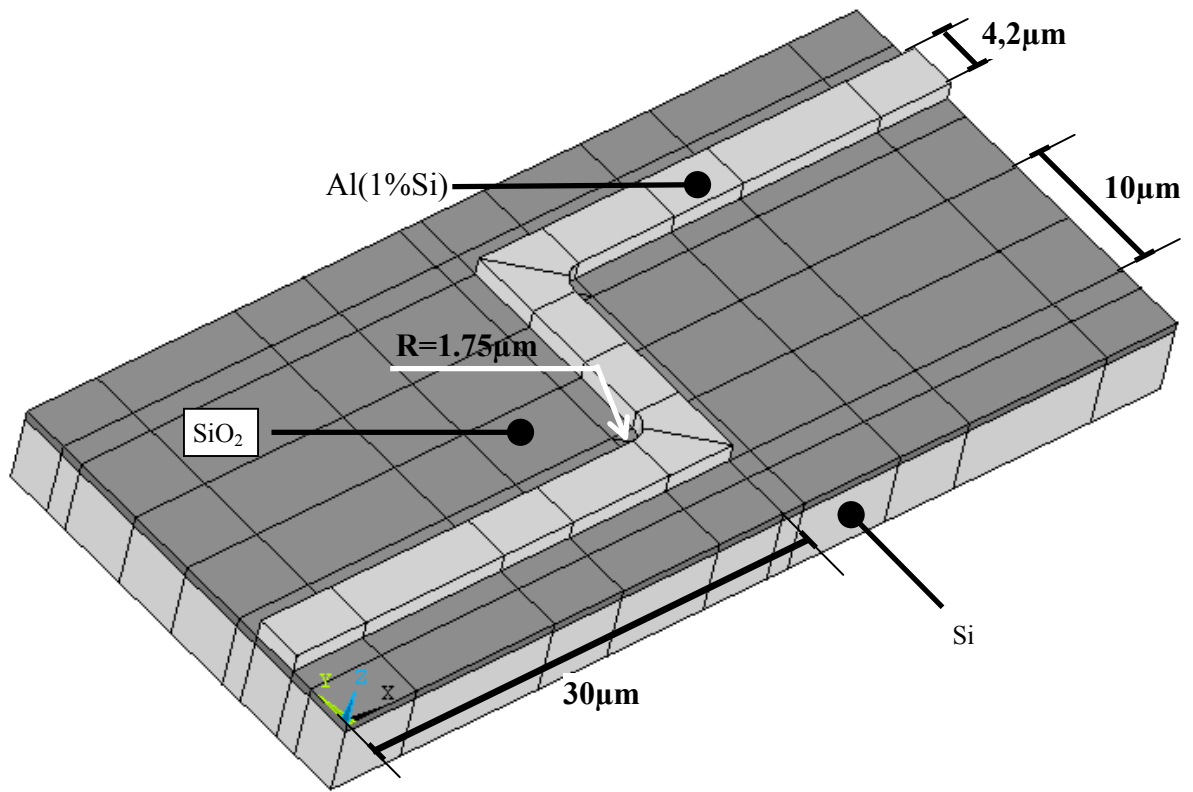


FIGURE 1.2. Geometry description of the meander structure.

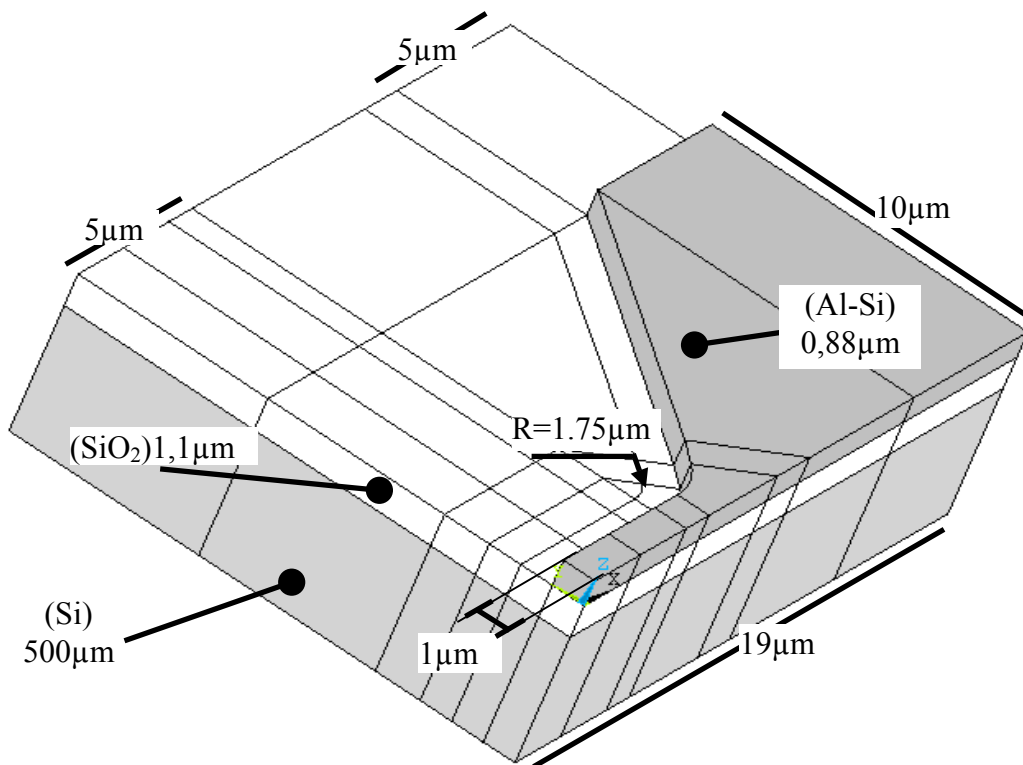


FIGURE 1.3. Geometry description of the SWEAT structure.

metallization layer in Aluminum (1%Si) was then structured in order to obtain the test samples. The geometries of the metallization structures were therefore instrumentally verified in order to avoid geometry dispersion between the reality and the modelling phase for the simulations. Figure 1.2 gives an overview of the geometrical description for the meander structure determined by SEM. Due to symmetry, only a part of the structure is given. The width for the meander was measured to be $4,2\mu\text{m}$. A measurement of the length for the long half part of the meander was determined to be $30\mu\text{m}$. A determination of the length for the short half part of the meander has been found to be $10\mu\text{m}$. The radius forming the inner corner of the metallization was measured to be $1,75\mu\text{m}$. The both structures were not fabricated together and some differences exist in their geometric description. Like presented for the meander structure, the dimensions of the SWEAT structure are provided in figure 1.3 where only a quarter of the whole structure is presented due to symmetry consideration. The geometries provided for both the meander and the SWEAT structures present only a part of the silicon substrate. Indeed, only a portion of the silicon thickness is taken into account. This consideration does not influence the results expected from the simulations because the thermal conductivity value of silicon is considerably lower than the values of the others material composing the model.

1.1.3 Experimental observations and measurement results

The reliability evaluation of the metallization structures was carried out using accelerated stress tests. In this process, the polycrystalline aluminum

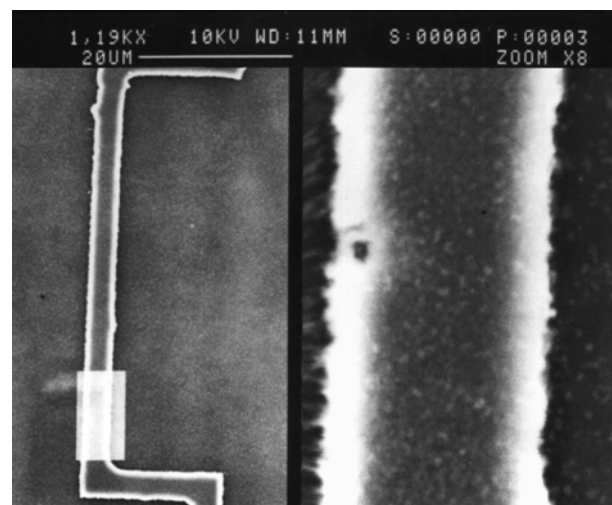


FIGURE 1.4. Nucleation in the meander structure.

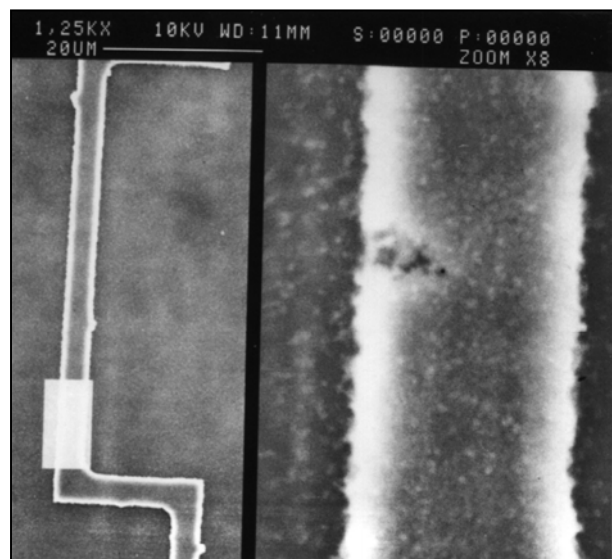


FIGURE 1.5. Void evolution within the structure.

metallization structures are supplied under high current densities levels. The tests were done by setting and fixing the substrate temperature to 180°C for the meander structure. The applied current within the metallization structure is maintained constant during the accelerated test until the electrical interconnection fails. The migration phenomenon in the meander structure has been observed and video-recorded with 200mA at a temperature of 180°C. The different steps of the void formation are shown from figure 1.4. The picture shows a nucleation appearing in the meander structure, near to the inner corner of the metallization. A beginning of hillocks formation around the metallization structure is also visible. Figure 1.5 represents the void formation development, and the path of the degradation seems to be orthogonal to the current flow. Figure 1.6 gives the continuation of the degradation in the meander structure again, and also shows some matter accumulation at the surface of the metallization structure giving birth to some extrusions. Finally, the picture provided by figure 1.7 shows a state where

the structure is almost completely destroyed due to diffusion phenomena induced voiding on the metallization. The destruction of the electrical interconnection is then effective when no more current goes through the structure. This moment is generally indicated by a jump in the measured electrical resistance during the test. A series of tests have been made under a constant temperature of 180°C with a variation of the applied current between 10mA and 500mA. Furthermore, a second series of test was investigated by maintaining a constant current density within the structure, and changing the environment temperature of test to

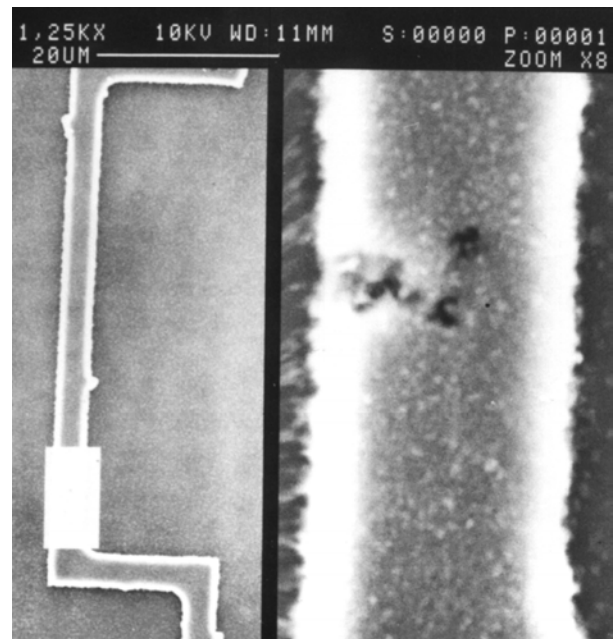


FIGURE 1.6. Developed void within the meander structure.

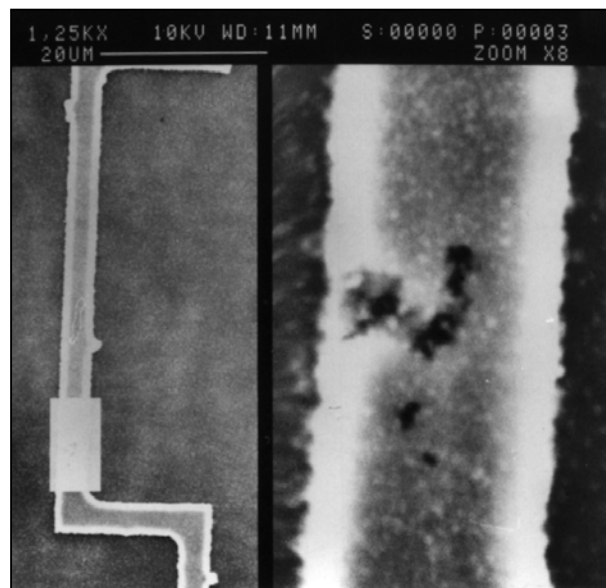


FIGURE 1.7. Evolution and limit of failure of the metallization structure.

130°C, 150°C and 180°C for a substrate temperature variation, in order to determine the activation energy E_A . Different important data such as the electrical resistance R_i of the structure without load, the electrical resistance R_b at the beginning of the tests, and the electrical resistance at failure time R_f have been measured. The Time-To-Failure values obtained by experimental results for the meander structure under the different test conditions are summarised and given in table 1.1.

| Samples | Stress conditions | | TTF $\times 10^3$ [s] | R_i [Ω] | R_b [Ω] | R_f [Ω] |
|---------|-------------------|------------------|--------------------------|-----------------------|-----------------------|-----------------------|
| | Current [mA] | Temperature [°C] | | | | |
| 1-1 | 100 | 130 | 104,1 | 37,9 | 25,0 | 40,4 |
| 1-2 | 100 | 130 | 101,1 | 36,9 | 26,1 | 43,7 |
| 1-3 | 100 | 130 | 102,6 | 35,4 | 25,1 | 43,0 |
| 1-4 | 100 | 130 | 106,2 | 34,9 | 24,8 | 40,5 |
| 1-5 | 100 | 130 | 134,4 | 34,7 | 24,7 | 41,6 |
| 2-1 | 100 | 150 | 67,8 | 39,3 | 26,1 | 43,5 |
| 2-2 | 100 | 150 | 74,7 | 35,2 | 24,7 | 36,5 |
| 2-3 | 100 | 150 | 67,62 | 34,7 | 25,0 | 36,3 |
| 2-4 | 100 | 150 | 92,4 | 36,3 | 24,7 | 38,2 |
| 2-5 | 100 | 150 | 74,82 | 38,1 | 25,8 | 40,2 |
| 3-1 | 100 | 180 | 43,8 | 39,6 | 25,0 | 40,4 |
| 3-2 | 100 | 180 | 32,7 | 40,6 | 25,7 | 43,7 |
| 3-3 | 100 | 180 | 34,5 | 39,6 | 25,0 | 43,0 |
| 3-4 | 100 | 180 | 26,1 | 39,5 | 24,9 | 40,5 |
| 3-5 | 100 | 180 | 28,5 | 40,0 | 25,3 | 41,6 |
| 4-1 | 70 | 180 | 102,6 | 39,2 | 25,3 | 40,3 |
| 4-2 | 70 | 180 | 85,5 | 40,7 | 26,3 | 42,7 |
| 4-3 | 70 | 180 | 86,22 | 42,5 | 28,1 | 45,0 |
| 4-4 | 70 | 180 | 79,5 | 39,3 | 25,5 | 42,7 |
| 4-5 | 70 | 180 | 97,32 | 39,0 | 25,3 | 41,1 |
| 5-1 | 50 | 180 | 276,6 | 37,9 | 25,5 | 39,7 |
| 5-2 | 50 | 180 | 252,3 | 36,6 | 24,4 | 38,0 |
| 5-3 | 50 | 180 | 171,6 | 36,8 | 24,5 | 41,4 |
| 5-4 | 50 | 180 | 230,82 | 38,9 | 25,6 | 41,4 |
| 5-5 | 50 | 180 | 198,48 | 38,1 | 25,7 | 40,6 |

TABLE 1.1. Reliability test and experimental results of the meander structure.

The SWEAT structure was tested at room temperature under several load levels and the following table 1.2 summarises the experimental results for the structure very well.

| | | | | | | | | |
|--|-------------------|---------------------|---------------------|---------------------|-------------------|----------------------|-----------------|------|
| Current density [MA/cm ²] | 13 | 14,8 | 17,6 | 18,2 | 18,75 | 19,25 | 19,8 | 21,6 |
| TTF[s] | 2×10 ⁵ | 7,2×10 ⁴ | 1,7×10 ³ | 5,3×10 ² | 4×10 ² | 1,45×10 ² | 10 ² | 10 |

TABLE 1.2. Reliability test and experimental results of the SWEAT structure.

These measurement results are important because they will be used for comparison with the simulation results.

1.2 Diffusion mechanisms in aluminum metallization structures

One of the most effects which contributes to the degradation of the metallization structures running under strong levels of load are the mechanisms of atomic diffusion. These different diffusion mechanisms exist, which are the bulk diffusion, the surface and/or the interface diffusion as well as grain boundary diffusion.

1.2.1 Bulk diffusion mechanisms

The bulk diffusion mechanisms are from different types. One of the most effective of them corresponds to the atomic diffusion due to the presence of atomic hole naturally present in the bulk material like shown in figure 1.8. An another one deals with the diffusion of ions of a material from type A inside a material from type B without mechanical disturbance. As presented in figure 1.9, this is caused by the smaller atomic volume of material A compared to the one of material B. Thus, an exchange in the position between two different neighboured ions is able to occur, and describes the « Position Mechanism Exchange » like given in figure 1.10. Finally, the environment and the running conditions can influence the interconnects texture like drawn in figure 1.11. Under strong temperature variations and/or mechanical stresses, the crystal structure can be subjected to mutations that create possible ways empowering the diffusion of ions.

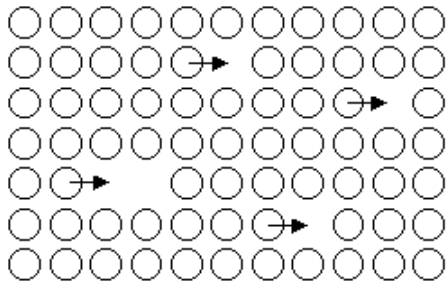


FIGURE 1.8. Hole diffusion mechanism.

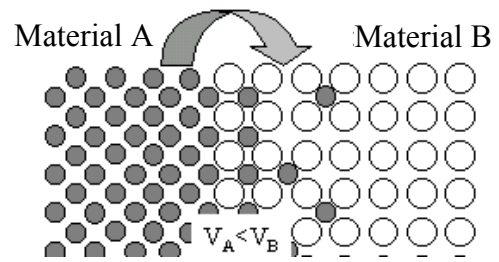


FIGURE 1.9. Volume difference diffusion.

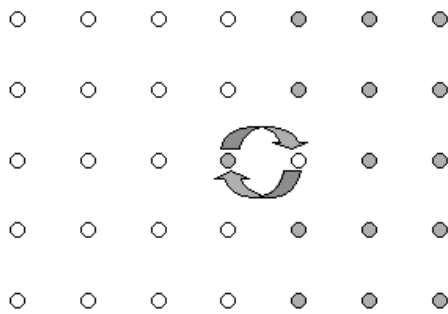


FIGURE 1.10. Substitution mechanism of diffusion.

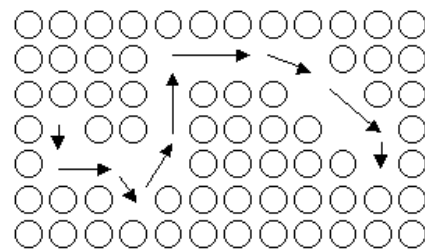


FIGURE 1.11. Diffusion path due to crystal mutation.

1.2.2 Surface and interface diffusion

One of the most easiest way for ion to diffuse takes place on the surface of metallization structures. Indeed, due to their low activation energy values (0,3 to 0,4eV for Al) at this location [32], it is easier to move them there than those included in the bulk (1,2 to 1,4eV). It is shown that the motion of material in surface regions particularly occurs when the structures are non-passivated [10]. In the case of aluminum, unpassivated interconnects are usually protected by a natural layer of Al_2O_3 due to early oxidation process after fabrication. The activation energy is consequently lightly higher than the values given above [11]. In addition, the metallic ions are able to migrate along the interfaces or to diffuse in an orthogonal direction trough the interface itself. The presence of a barrier layer (mostly Ti and/or TiN) between both different materials at the interface insures the stability of the metallization structure geometry and brakes the diffusion velocity of atomic elements. In this case, it emphasises the lifetime and the reliability of the interconnects.

1.2.3 Grain boundary diffusion

One of the major ways taken by the ions when diffusion occurs are the grain boundary regions [12,13]. These regions result in an axis misorientation when the crystal of the material is growing. Indeed, the atomic ions are deposited on a substrate where molecule islands are forming in order to form the metallization structures. In this case the crystal takes a random orientation at the beginning of its growth compared to other regions. Then the accumulation of atoms induces the formation of grain boundaries at the limit region of growth. Consequently, the fabrication process creates some dislocation in the common regions of two different grains, which are named as "Grain Boundary". At these locations, the ions are lightly connected with the crystal and are then also easier to be extracted from the metallization structures and to be put into circulation. Moreover, the matter depletion for void formation starts in these regions [14]. The value of the activation energy of atoms at these locations is smaller than in bulk regions. This make them more mobile, and then able to participate to the formation of voids (depletion process) as well as to hillock formation (accumulation process) in these regions. An illustration of a polycrystalline aluminum line is given on the left side of figure 1.12. The right side represents the grains and the grain boundary regions are schematically given on the left side. A grain structure is characterised by its geometry, where

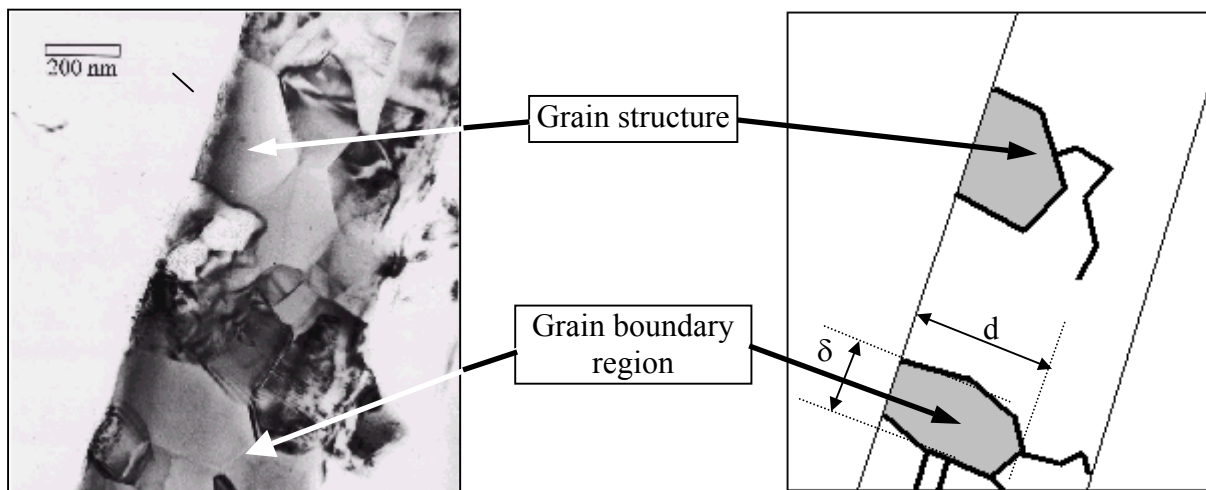


FIGURE 1.12. Grains and grain boundaries observations.

d is the grain average length, and δ the effective width. The grains shown in figure 1.12 are about 230nm long, and 110nm large.

As presented previously, all of the diffusion mechanisms contribute to the formation of voids (due to atomic depletion) as well as hillock formation (caused by particle accumulation). The diffusion phenomena are driven by different effects. One of them corresponds to the presence of an electron-wind exercising a mechanical strength on the ions able to displace them when the current density within the metallization structure reaches a certain level (more than 10kA/cm^2 for aluminum). Another one comes from the presence of strong temperature gradients, capable to participate to matter migration. The direction taken by the local temperature gradient vector amplifies or decelerates the migration mechanism and is more known as thermomigration. Finally, the formation of microvoids in metallization structures can occur under strong thermal induced stress and/or external mechanical loading. The mechanical force that acts on the crystal is derived from the presence of some gradients in the hydrostatic stress, and the migration mechanism is known as stressmigration.

The formation of voids and hillocks consequently also depends on the fabrication process (due to the residual stresses), the running conditions (due to the thermal environment), and also from the design of the metallization itself (due to its geometry).

2. Theoretical background of matter migration in interconnects

2.1 Physical aspects of migration

The metallic material motion induced failure of metallization structures by high current density refers to complex mechanisms. The typical effects acting and amplifying the degradation of chip-level interconnects are from different types, and have been interpreted from experimental observations. One of the first effects that has been carried out concerns the influence of the current density under which the metallization structure is running. Volumetric matter motion has been reported when the value of current density reaches about 10^5 A/cm^2 at room temperature environment conditions. In the same time, a temperature elevation due to the Joule self-heating phenomena on the metallization line occurs and the produced energy needs to be removed. Indeed, the metallization structure will fail rapidly if the heat flux through the substrate and the material surrounding it is not enough important to evacuate the created energy. The metallization structure should be maintained at the environment temperature running conditions in order to avoid the deterioration due to the temperature itself. In this case, the limit charge of 10^5 A/cm^2 is a critical run condition and the lifetime of the interconnect would be very limited [62]. Above this limit, the diffusion phenomena induced matter migration well-known as "electromigration" is able to occur.

As the current density increases, strong temperature level can be reached for particular designs and encapsulation technologies of the metallization structure. High temperatures play an important role on the migration of ions and the temperature distribution can have an important impact on the degradation acceleration of the chip-level electrical contacts. Indeed, a structure at uniform temperature does not show signs of ions displacement due to thermal diffusion. In the contrary, some temperature gradients occur when temperature is not the same all over the structure and the statistic diffusion of ions becomes inhomogeneous. In this situation, metallic ions are able to migrate in the direction of the temperature gradient. This phenomena is generally reported as « thermomigration ». This second form of metallic ions migration also contributes to the destruction of interconnects running under strong temperature conditions.

One of the other effects that contribute to the degradation of metal line interconnects in integrated circuits is thermally induced by the temperature distribution over the structures. All the materials composing the structure have a great influence on the thermal-induced

mechanical stress levels since that all of them have different values of the thermal coefficient of expansion (CTE). When a metallization structure runs under high current density, high temperature levels as well as strong values of temperature gradients can occur, forcing some parts of the metallization to expand themselves or to be compressed under hydrostatic stress. This behaviour takes place due to the differences in the CTE of these materials, implying them to dilate differently. The expansions inducing some tensile stresses can lead to formation of microvoids if a critical stress level is reached and can be amplified to void formation until the electrical interconnection fails. Also, an accumulation of material due to compressive stress can lead to the presence of tensile stress in passivation layers able to cause cracks and their destruction if a certain level within the passivation layer is reached. Since tensile and compressive stress are derived from the presence of thermally induced micro-mechanical strength, matter migration within the structure can take place. This effect is known as “stressmigration”.

Finally, the reliability of interconnection structures can be affected by the fabrication process as well as the induced mechanical stress. Indeed, non-homogeneity in the material concentration is able to occur when the metallization layers and the vias are fabricated followed by a cooling to ambient temperature. This creates some concentration gradients in the structures. Also, the induced mechanical stress participate simultaneously to the appearance of concentration gradients. These gradients induces natural diffusion from region with important value of atomic concentration to regions with lower concentration values.

2.2 Mathematical modelling of ions massflow in interconnects

2.2.1 Modelling of the electromigration

When a metallization structure is loaded under an electrical charge, the flow of electrons circulating within the interconnect induces a strength field on the crystal bonded ions. This strength field is the resulting force of two different influences [15]. The first one is created by the crystal ions $\vec{F}_{ion} = Z_{ion} \cdot e\vec{E}$, and the second one is well-known as “electron-wind” effect, described by $\vec{F}_e = -e\tau v_l n \sigma \vec{E}$. Z_{ion} is the charge number of ions, e is the electron charge and \vec{E} the local electrical field. v_l is the mean value of the electrons velocity, n is the electron density, τ is the transit time of an electron between 2 atoms and σ the mean value of

the surface of ions diffusion. The superposition of these two physical phenomena corresponds to the “electrotransport” or "electromigration" of metal migration induced degradation in the metallization structures. The efficient force $\vec{F}_{eff} = \vec{F}_{ion} + \vec{F}_e$ is proportional to the effective charge number of ions $Z^*=Z_{ion}-\tau v n \sigma$. The resulting massflow is defined by equation (2.1):

$$\vec{J}_A = \frac{N}{k_B T} e Z^* \vec{j} \rho D_0 \exp\left(-\frac{E_A}{k_B T}\right) \quad (2.1)$$

N is the atomic concentration, Z^*e represents the effective charge of ions, \vec{j} corresponds to the local current density vector, ρ is the temperature dependant value electrical resistivity of the metal, D_0 defines the self diffusion coefficient of the conductor material, k_B is the Boltzmann constant, T is the value of the local temperature and E_A the value of the activation energy of the material.

2.2.2 Modelling of the thermomigration

A metallization structure under high current density level induces an inhomogeneous temperature distribution and an appearance of temperature gradients. As explained previously, the temperature gradients drive to a force able to participate to the massflow along the structure. The ionic massflux due to the thermal response of interconnects is modelled by the following equation (2.2) :

$$\vec{J}_{th} = -\frac{NQ^* D_0}{k_B T^2} \exp\left(-\frac{E_A}{k_B T}\right) gradT \quad (2.2)$$

Q^* represents the specific heat of transport of the metallic material where $Q^*=\beta H_m-H_f$. H_m and H_f are respectively the molar enthalpies of migration and formation for vacancies and β is a dimensionless constant approximately equal to 0,8 [16]. Equation (2.2) denotes a proportionality with the local temperature gradient vector $gradT$.

2.2.3 Modelling of the stressmigration

Thermal induced mechanical stress in metallization structures are capable to move material under tensile as well as compressive state of material. Tensile stresses contribute to

voids formation whereas compressive stresses can lead to hillocks and cracking formation of the passivation layers in the IC [3]. Indeed, a bare of material with an initial length l_0 at the temperature T_0 would have a length l at the temperature T defined by equation 2.3:

$$l = l_0(1 + \alpha_l(T - T_0)) \quad (2.3)$$

The mismatch in the CTE α_l of the different materials can lead to the development of tri-axial stress as a result of a change in the temperature [17]. The difference in the dilatation coefficient of the different materials assembled together produces undesirable effects such as frontal pressure as well as strong mechanical stress at the interface regions. The mechanical stress due to the thermal variations is generally defined by equation 2.4:

$$\sigma_{th} = E \cdot \alpha_l \cdot (T - T_0) \quad (2.4)$$

The mechanical stress defined at a particular location is given by the stress tensor S_t presented by equation 2.5:

$$S_t = \begin{pmatrix} \sigma_{xx} & \tau_{xy} & \tau_{xz} \\ \tau_{yx} & \sigma_{yy} & \tau_{yz} \\ \tau_{zx} & \tau_{zy} & \sigma_{zz} \end{pmatrix} \quad (2.5)$$

where σ_{xx} , σ_{yy} , σ_{zz} represent the normal components of stress and $\tau_{xy} = \tau_{yx}$, $\tau_{yz} = \tau_{zy}$ and $\tau_{zx} = \tau_{xz}$ are the shear stress components. The coupling of the temperature effects on the expansion of a material is then defined by the Hooke law:

$$\begin{aligned} \varepsilon_{xx} &= \frac{\partial u}{\partial x} = \frac{1}{E} [\sigma_{xx} - \nu(\sigma_{yy} + \sigma_{zz})] + \alpha_l(T - T_0) \\ \varepsilon_{yy} &= \frac{\partial v}{\partial x} = \frac{1}{E} [\sigma_{yy} - \nu(\sigma_{xx} + \sigma_{zz})] + \alpha_l(T - T_0) \\ \varepsilon_{zz} &= \frac{\partial w}{\partial x} = \frac{1}{E} [\sigma_{zz} - \nu(\sigma_{xx} + \sigma_{yy})] + \alpha_l(T - T_0) \end{aligned} \quad (2.6)$$

where u , v , and w are the expansion values respectively following the x , y and z directions. E is the Young modulus and characterizes the elasticity of the material and ν the Poisson ratio that represents for example the retraction rate of matter (in y and z directions) when the matter expands or retracts in the x direction. The global stress value (Von Mises stress) is generally

$$\sigma_v = \sqrt{\frac{1}{2} [(\sigma_{xx} - \sigma_{yy})^2 + (\sigma_{yy} - \sigma_{zz})^2 + (\sigma_{zz} - \sigma_{xx})^2]} \leq \sigma_l \quad (2.7)$$

defined as given by equation 2.7. σ_l represents the critical stress level admitted by the material. σ_l is generally represented in the literature to be about a few 100MPa for aluminum.

Volumetric relaxation mechanism, such as voiding or cavitation [9], may act to relieve the stress levels and represents one causes of the degradation due to the mechanical behaviour of the whole structure. Sometimes, the presence of some microvoids within the metallization structure during fabrication process also participates by the same way to the performances degradation of the electrical interconnection. These effects are responsible for the atomic transport due to mechanical activity within the structure. The ionic massflow for the mechanical influence is given by the following equation :

$$\vec{J}_S = -\frac{N\Omega D_0}{k_B T} \exp\left(-\frac{E_A}{k_B T}\right) \text{grad}\sigma_H \quad (2.8)$$

Ω defines the atomic volume and σ_H the local hydrostatic stress value ($\sigma_H = (\sigma_{xx} + \sigma_{yy} + \sigma_{zz})/3$), where σ_{xx} , σ_{yy} , and σ_{zz} correspond respectively to the normal components provided by the local stress tensor.

2.2.4 Modelling of the concentration distribution effect

The filling rate of multilevel interconnects as well as non homogeneous atomic concentration distribution within metallization structures used for the microelectronic industry can have an important impact on the degradation caused by particles diffusion induced migration. The control of the deposition processes as well as the method used for the fabrication of vias and metallization structures are important key factors for their reliability. A local variation in the atomic concentration can then occur during the fabrication and mostly in the grain boundary regions during the crystal growth. Under concentration gradient, the atoms are then able to diffuse within the metallization under the effect of the temperature. The flow of ions under atomic concentration gradient can be expressed like presented by equation (2.9):

$$\vec{J}_C = -D_0 \exp\left(-\frac{E_A}{k_B T}\right) \text{grad}N \quad (2.9)$$

2.3 Time-dependency modelling of the phenomena

The metallization structures running under strong environment conditions are subjected to matter motion induced failures. The different effects presented previously contribute together to the birth of an atomic massflux within the interconnects. The formation of voids as well as hillocks is due to the presence of a divergence in the ionic massflow. A location associated with a positive value in the massflow divergence implies the formation of a void whereas a location with a negative value represents an accumulation of material or the formation of a hillock. The matter migration phenomena is time-dependent and is theoretically modelled by the following continuity equation :

$$\frac{dN}{dt} + \text{div}(\vec{J}_{tot}) = 0 \quad (2.10)$$

2.3.1 Massflow divergence due to the electromigration

The calculation of the massflow divergence affected by the electromigration relates to certain background in physics. In our case, the experiments have been made under constant current load. The following approximation $\text{div}(\vec{j}) = 0$ is needed to be considered [18]. The results obtained taking into account the atomic concentration distribution is given by the following expression:

$$\text{div}(\vec{J}_A) = \left(\frac{E_A}{k_B T^2} - \frac{1}{T} + \alpha \frac{\rho_0}{\rho} \right) \cdot \vec{J}_A \cdot \text{grad}T + \frac{1}{N} \text{grad}N \quad (2.11)$$

Since \vec{J}_A is proportional to the local current density vector \vec{j} , the scalar $\vec{j} \cdot \text{grad}T$ is noticeable in equation (2.11). α is the thermal coefficient of resistivity of the conductor material used to fabricate the metallization structure.

2.3.2 Massflow divergence for the thermomigration

The calculation of the massflow divergence related to the thermomigration is carried out in two different steps. The first expression obtained is given as followed:

$$\text{div}(\vec{J}_{th}) = -\frac{Q^* D_0}{k_B T^2} \left[N \cdot \text{divgrad}T + N \cdot \left(\frac{E_A}{k_B T} - 2 \right) \frac{\text{grad}^2 T}{T} + \text{grad}N \cdot \text{grad}T \right] \quad (2.12)$$

An another formulation with some local parameters like $gradT$ is possible using the equations (2.13) and (2.14), where κ is the thermal conductivity of the metallic material, σ the local electrical conductivity and V the local electrical potential:

$$\kappa \cdot divgradT + gradT \cdot grad\kappa = -\sigma(gradV)^2 \quad (2.13) \quad \kappa = 3\left(\frac{k_B}{e}\right) \frac{T}{\rho_0(1 + \alpha(T - T_0))} \quad (2.14)$$

A transformation of equation (2.13) provides the opportunity to reformulate the expression (2.12) with help of equation (2.15):

$$divgradT = -\left\{ \frac{j^2 \rho^2 e^2}{3k_B^2 T} + \left(\frac{1}{T} - \alpha \frac{\rho_0}{\rho}\right) grad^2 T \right\} \quad (2.15)$$

Another form of equation (2.12) can then be obtained, and the massflow divergence value concerning the thermomigration is then given by the following expression:

$$div(\vec{J}_{th}) = \left(\frac{E_A}{k_B T^2} - \frac{3}{T} + \frac{\alpha \rho_0}{\rho}\right) \cdot \vec{J}_{th} \cdot gradT + \frac{NQ^* D_0}{3k_B^3 T^3} j^2 \rho^2 e^2 \exp\left(-\frac{E_A}{k_B T}\right) + \frac{1}{N} \vec{J}_{th} \cdot gradN \quad (2.16)$$

The local temperature gradient has an important influence on the material motion induced by the thermal effects. Equation (2.16) also shows the dependence of the massflow divergence with the value of the local current density \vec{j} .

2.3.3 Massflow divergence for the stressmigration

In a first step, the divergence value of the massflow due to the thermomechanical stress takes the form as shown by the following equation:

$$div(\vec{J}_S) = -\frac{N\Omega D_0}{k_B T} \exp\left(-\frac{E_A}{k_B T}\right) \left\{ \left(\frac{E_A}{k_B T^2} - \frac{1}{T}\right) grad\sigma_H gradT + divgrad\sigma_H \right\} - \frac{N\Omega D_0}{k_B T} \exp\left(-\frac{E_A}{k_B T}\right) grad\sigma_H gradN \quad (2.17)$$

The influence of the thermally induced mechanical stress on voids and hillocks formation has been already demonstrated [9] and the divergence value of the hydrostatic stress gradient is:

$$\text{divgrad}\sigma_H = \frac{2E}{3(\nu-1)}\alpha_l\text{divgrad}T \quad (2.18)$$

Finally, the whole expression obtained for the stress massflow divergence is represented by the following formula:

$$\begin{aligned} \text{div}(J_S) = & \left(\frac{E_A}{k_B T^2} - \frac{1}{T} \right) \bar{J}_S \text{grad}T + \frac{1}{N} \bar{J}_S \text{grad}N \\ & - \frac{2N\Omega D_0 E \alpha_l}{3k_B T(1-\nu)} \exp\left(-\frac{E_A}{k_B T}\right) \left\{ \frac{j^2 \rho^2 e^2}{3k_B^2 T} + \left(\frac{1}{T} - \frac{\rho_0 \alpha}{\rho} \right) \text{grad}^2 T \right\} \end{aligned} \quad (2.19)$$

The divergence in the massflow due to the mechanical stress shows a dependence on the local temperature gradient $\text{grad}T$ as well as on the local current density \vec{j} . It is also a function of the material itself through the presence of some mechanical and thermomechanical parameters such as the Young modulus E , the Poisson ratio ν and the coefficient of thermal expansion α_l .

2.3.4 Massflow divergence due to the concentration distribution

The atomic concentration distribution induced diffusion due to atomic concentration gradients in the metallization structure implies the existence of a divergence in the atomic massflow determined by the following expression:

$$\text{div}(\bar{J}_C) = \frac{E_A}{k_B T} \cdot \frac{\text{grad}T}{T} \bar{J}_C - D_0 \exp\left(-\frac{E_A}{k_B T}\right) \text{divgrad}N \quad (2.20)$$

This equation shows a strong dependence of ions motion with the local temperature gradient and remains in a complex form. In this work, only the phenomenon of electromigration, the thermomigration and the stressmigration are considered. In this case, the total value of the divergence in the massflux is defined by:

$$\text{div}(\bar{J}_{Tot}) = \text{div}(\bar{J}_A) + \text{div}(\bar{J}_{Th}) + \text{div}(\bar{J}_S) \quad (2.21)$$

The theoretical expression of the total massflux divergence, taking into account the electromigration, the thermomigration and the stressmigration is then given by the following equation (2.22):

$$\begin{aligned}
div(\vec{J}_{Tot}) = & \left(\frac{E_A}{k_B T^2} - \frac{1}{T} + \alpha \frac{\rho_0}{\rho} \right) \vec{J}_A \cdot gradT + \left(\frac{E_A}{k_B T^2} - \frac{3}{T} + \alpha \frac{\rho_0}{\rho} \right) \vec{J}_{th} \cdot gradT \\
& + \frac{NQ^* D_0}{k_B T^2} \cdot exp\left(-\frac{E_A}{k_B T}\right) \cdot \frac{j^2 \rho^2 e^2}{3k_B^2 T} + \left(\frac{E_A}{k_B T^2} - \frac{1}{T} \right) \cdot \vec{J}_S \cdot gradT \\
& - \frac{2N\Omega D_0 E\alpha_l}{3k_B T(1-\nu)} \cdot exp\left(-\frac{E_A}{k_B T}\right) \cdot \left\{ \frac{j^2 \rho^2 e^2}{3k_B^2 T} + \left(\frac{1}{T} - \frac{\rho_0 \alpha}{\rho} \right) \cdot grad^2 T \right\} \quad (2.22)
\end{aligned}$$

This last equation is used for the calculation of the massflux divergence distribution and in the calculation of the time-dependency during of the simulation of the voiding phenomena. The maximum value found in the massflux divergence distribution will indicate the weakest part of the metallization structures and provide the failure location in the metallization structure. Also, the relationship between the TTF and the divergence value has been established, like shown by equation 2.23:

$$TTF \propto 1 / Div(\vec{J}_{Tot}) \quad (2.23)$$

3. Thermophysical properties of the used materials

In this chapter, the thermophysical properties of the used materials out of the literature are provided. At first, the general physical constants for aluminum is given. In the second part of this chapter, the physical data representing the phenomena of the electromigration are presented. The different values characterising the electromigration phenomena found for the effective charge number Z^* for the aluminum material will be given. Then, the values of the specific heat of transport Q^* for aluminum will be presented. Furthermore, the values of the self-diffusion coefficient D_0 as well as the activation energy E_A for aluminum are given. The results of the electrical characterization of the materials used for the fabrication of the thin films of the samples are also provided. Finally, the temperature-dependent thermal conductivity values of the different materials as well as their thermomechanical properties will be provided.

3.1 General physical constants for aluminum

In the chapter presenting to the theory for material motion in metallization structures, the different physical contributions as well as their physical model have been presented. The models are physical equations which are dependent from well-known physical constant like the Boltzmann constant k_B , the electrical charge unit e , the atomic concentration N for aluminum and the atomic volume Ω . These physical parameters are used in the program for the calculation of the divergence values and the determination of the time-dependency of the phenomena. Their values are given in table 3.1.

| Parameters | Values |
|----------------------------|--|
| Electrical charge unit e | $1,602 \times 10^{-19} \text{C}$ |
| Boltzmann constant k_B | $1,38 \times 10^{-23} \text{J/K}$ |
| Atomic volume Ω | $0,166055 \times 10^{-10} \mu\text{m}^3$ |
| Atomic concentration N | $6,022098 \times 10^{10} \mu\text{m}^{-3}$ |

TABLE 3.1. Physical constants (as for aluminum).

3.2 Thermophysical properties investigations of the used materials

The characterization of the materials used in the samples fabrication is necessary in order to reproduce the experiments by simulations as better as possible. The values found in the literature generally knows some deviations. Consequently, it is important to have an idea of the range of the data available in order to study their influence on the simulation results.

3.2.1 The effective charge number Z^* for aluminum

B. Ernst [19] reported some measurement results for the electromigration contribution in the aluminum. A coupled value $D_0Z^*=0,067\text{cm}^2/\text{s}$ was found. The experiments took place with an applied current density value of $14,1\text{kA}/\text{cm}^2$ and in an environment where the temperature range was $[470^\circ\text{C}-610^\circ\text{C}]$. In another study, Y. Limoge [20] investigated the aluminum diffusion phenomena using the “markers experiment” method, in which the displacement of markers placed on the surface of the metallization is measured. The analysis has permitted the extraction of the effective charge number $Z^*=-13,7$ under an applied current density of $9,55\text{kA}/\text{cm}^2$ at 849K . In his investigations, H. Hoebbel [21] proposed a value of

| Value of the effective valence Z^* for aluminum | Particular comments | References |
|--|--|------------|
| $D_0Z^*=0,067\text{cm}^2/\text{s}$ (Absolute value) | Drift Velocity Method measurements, under $141\text{A}/\text{mm}^2$, and within a temperature range $[470^\circ\text{C}-610^\circ\text{C}]$ | [19] |
| $Z^*=-13,7$ | Markers motion experiment under $9,55\text{kA}/\text{cm}^2$ at 849K | [20] |
| $Z^*=-10$ | Values between -100 and -1 mentioned and referred to previous work | [21] |
| $-20 < Z^* < -1,2$ | No comments provided | [17,22,23] |
| $Z^*=Z(1-\chi/\rho)$ | $Z^*=-7,4$ at 400K , where $Z=1$, and $\chi=45$ | [24] |
| $Z^*=Z_{\text{dir}}+K/\rho$ | Al (Self): $K=-38,5$ and $K/\rho=-8,2$ AlSi alloy: $K=-185,7$ and $K/\rho=-39,6$ AlCu alloy: $K=-97,4$ and $K/\rho=-20,8$ | [25] |
| $Z^*=-20$ | No comments provided | [19] |

TABLE 3.2. Effective charge number Z^* for aluminum.

$Z^*=-10$ based on possible comparison with available results. Also, a range of values from -100 to -1 making reference to reported work was provided in this work. J. T. Trattles reported a used value of -1,2 for the effective valence Z^* in his investigation [17]. Others values have been proposed in the literature, like a value of -20 for aluminum [22,23]. In parallel, the effective valence determination for aluminum has knew some particular interests so far that people have tried to model it physically using others known parameters. To do so, S. Shingubara et. al. [24] have proposed an expression which is $Z^*=Z(1-\chi/\rho)$. In this expression, χ represents an empirically determined value of 45 and ρ represents the electrical resistivity of aluminum ($Z=1$). In this case, Z^* was then obtained to be -7,4 at 400K. Finally, J. P. Dekker and A. Lodder have proposed an another physical model in their publication [25] where the effective charge number could be defined as $Z^*=Z_{dir}+K/\rho$. In this model, Z_{dir} is the direct atomic valence number, K is a constant depending on the temperature and ρ is the electrical resistivity of the material. The data provided there were given for pure aluminum and for some alloys like the AlSi and the AlCu alloys. The data provided there from the literature and their references are summarised in table 3.2. For the simulations performed in this investigation, a value of $Z^*=-10$ has been considered.

3.2.2 The specific heat of transport Q^* for aluminum

Like for the electromigration phenomena, the thermomigration has been studied and observed with more attention. A. Christou [26] describes the specific heat of transport Q^* as a function for the molar enthalpies of migration H_m , the molar enthalpies H_f of formation for vacancies and a dimensionless constant β , where $Q^*=\beta H_m-H_f$. It is then referred that Q^* would be essentially temperature independent in the case of aluminum for temperature up to 500°C. In this case, a value of 0,3eV is presented. Thin film materials have been characterized in order to extract the thermomigration parameters for aluminum [27]. The thermomigration was measured providing a global value for DQ^* of $6 \times 10^{-9} \text{m}^2 \text{eVs}^{-1}$. An effective diffusion coefficient D was estimated from measurement results to be $2 \times 10^{-7} \text{m}^2 \text{s}^{-1}$ leading to a value of 0,03eV for the specific heat of transport Q^* . This value disagrees with results on polycrystalline aluminum because a negative value was expected due to the flow of atoms from cold to hot areas. In his dissertation, O. Kraft [28] has carried out some investigations in the domain of simulation and a value of -7kJ/mol for the thermomigration of aluminum was

used. H. Wever has proposed a different value for the thermomigration in aluminum [29] where Q^* was determined to be -2kcal/mol was suggested. In a later study [30], the thermomigration for pure aluminum was measured with help of the "markers experiment" under alternative current (which compensate the electromigration phenomena) and a value $Q^*=0,07\text{eV}$ was determined. Table 3.3 summarises these values. The value used within the simulations of this work is $Q^*=-0,0867\text{eV}$.

| Specific heat of transport Q^* | Particular remarks | References |
|----------------------------------|---|------------|
| 0,3eV | Referred measured value. | [26] |
| 0,03eV(See particular remarks) | $DQ^*=6\times 10^{-9}\text{m}^2\text{eVs}^{-1}\Rightarrow Q^*=\pm 0,03\text{eV}$ when $D=2\times 10^{-7}\text{m}^2\text{s}^{-1}$. | [27] |
| -7KJ/mol#-0,07256eV | No remarks. | [28] |
| -2kcal/mol#-0,0867eV | No remarks. | [29] |
| 0,07eV | Measurements based on markers motion experiment. Values for Q^* of -0,06eV, -0,09eV and 0,48eV are also cited in the literature. | [30] |

TABLE 3.3. Specific heat values for aluminum.

3.2.3 The Self-diffusion coefficient D_0 for aluminum

In order to simulate the matter migration phenomenon in metallization interconnects, the determination of the parameters related to the diffusion processes of ions is necessary. The self-diffusion coefficient D_0 controls the degradation velocity of the interconnects and needs to be precisely determined. It's mostly a function of the alloying elements present in the matrix material (here aluminum). This value must reflect the real diffusion process that takes place on our samples during the experiments very well to be integrated to the simulation investigations. In aluminum, the influence of alloying elements on the global diffusivities of ions has been investigated [31], and their effects on the lifetime of metallization structures and interconnects have been determined [32,33]. A value of $10^{-2}\text{cm}^2/\text{s}$ has been used for simulation by John T. Tattles [17] and a value of $1,4\times 10^{-2}\text{cm}^2/\text{s}$ was used by O. Kraft [28]. In other studies [30,34], a different value for the self-diffusion coefficient of $0,047\text{cm}^2/\text{s}$ is mentioned. Also, a value like $1,71\text{cm}^2/\text{s}$ for pure aluminum has been used and reported in the

literature [35,36]. Furthermore, V. Petrescu has used a value of $0,1\text{cm}^2/\text{s}$ in her work [37], where she tried to reproduce the electromigration per simulation considering the electromigration as a gas-fluid system. Moreover, M. Scherge [38] took a value of $10^{-4}\text{cm}^2/\text{s}$ for its investigations. To finish with, different values for the self diffusion-coefficient are mentioned in the literature [39]. A value of $1,17\text{cm}^2/\text{s}$ extracted under low specific activity is given with the radiotracer method. Under TEM observations, a value of $0,176\text{cm}^2/\text{s}$ has also been found. In addition, a self-diffusion coefficient of $0,137\text{cm}^2/\text{s}$ has been extracted. In this case, measurements have been also carried out, with help of a semilogarithmic plot of the self-diffusion coefficient versus the temperature for pure aluminum, and a value of $0,132\text{cm}^2/\text{s}$ was determined. The following table summarises the values of D_0 found in the literature.

| Self-Diffusion coefficient D_0 [cm^2/s] | Comments | References |
|---|---|------------|
| 10^{-2} | Used for simulation | [17] |
| $1,4 \times 10^{-2}$ | Chosen for simulation | [28] |
| 0,047 | Values were considered for different investigations | [30,34] |
| 1,71 | | [35,36] |
| 0,1 | | [37] |
| 10^{-4} | | [38] |
| 1,17;0,176 0,137;0,132 | Respectively radiotracer, TEM, NMR measurement methods, and graphical analysis used | [39] |

TABLE 3.4. Self-diffusion coefficient values for aluminum.

3.2.4 The activation energy E_A for aluminum

A conductor material used for the fabrication of metallizations structures can also be characterised by an activation energy value, which represents the energy needed to extract an atomic ion from its stable state position within a crystal. This value depends on the kind of material used for the metallizations fabrication and can differ for aluminum and alloys. The activation energy for pure materials is indeed theoretically well-known and this value can sharply differ with a light addition of other materials to form metallic alloys. It can also depends on the diffusion mode that occur within the structure, where four different kind of

diffusion have been already reported for pure aluminum. Indeed, one concerns the surface diffusion of material, where values between 0,2 and 0,45eV have been mentioned. The second type of diffusion takes place at the interfaces where values of the activation energy was already determined in a range of 0,45eV to 0,7eV. Furthermore, the diffusion process of atomic ions is able to occur along the grain boundary regions caused by some disorientation during the crystal growth. The same range value of activation energy for grain boundary diffusion is predicted as those for the interface diffusion. Finally, the atomic state of ions located inside the ordered crystal can be destabilised with an activation energy oscillating between 1,2 and 1,4eV. However, the grain boundary diffusion phenomena has been observed [40] in $\text{AlNi}_{0,1}\text{Cr}_{0,1}$ alloy, and a value of $0,84\pm 0,03\text{eV}$ was extracted. In an another work [41], a value of about $0,79\pm 0,02\text{eV}$ was measured for the $\text{AlSi}_{0,01}\text{Cu}_{0,005}$ alloy. A. Christou recorded different values of the activation energy for an AlSi alloy as the temperature increases [16]. A value of 0,63eV has been found for temperature up to 350°C and a value of 0,55eV was determined between 350°C and 550°C. In addition, the influence of alloys have been investigated [42], showing some differences with the alloyed element. The activation energy corresponding to pure aluminum has been reported to be 0,45eV again and confirms previous referred works.

| Activation energy value | Comments | References |
|-------------------------------------|---|------------|
| 0,2eV to 0,45eV | Surface diffusion | [32] |
| 0,45eV to 0,7eV | Interface as well as grain boundary diffusion | |
| 1,2eV to 1,4eV | Bulk/volume diffusion | |
| $0,84\pm 0,03\text{eV}$ | Grain boundary diffusion for the $\text{AlNi}_{0,1}\text{Cr}_{0,1}$ alloy | [40] |
| $0,79\pm 0,02\text{eV}$ | $\text{AlSi}_{0,01}\text{Cu}_{0,005}$ alloy | [41] |
| 0,63eV(1) and 0,55eV(2) | AlSi alloy, (1): $T < 350^\circ\text{C}$ and (2): $350^\circ\text{C} < T < 550^\circ\text{C}$ | [16] |
| 0,45eV(1) 0,72eV(2) 1,07eV(3) | (1): Pure aluminum (2): AlCu alloy (3): AlMg alloy | [43] |
| 0,57eV(1) 0,97eV(2) | (1): annealed pure aluminum (2): “as-deposited” pure aluminum measured by the drift velocity method | [42] |
| 0,58eV | Al(1%Si) under $3\text{MA}/\text{cm}^2$ | [44] |
| 0,39eV | Value extracted from the meander test results | |

TABLE 3.5. Activation energy for aluminum and aluminum alloys.

A stronger value was found to be 0,72eV for an aluminum based copper alloy. Therefore, a strong value of 1,07eV was measured when Mg is added to the aluminum. Finally, the influence of the fabrication process on the apparent activation energy has been showed [43]. It was then found that the activation energy for pure aluminum can sharply differ with the fabrication process. Some annealed metallization stripes provided some values at about $E_A=0,57\text{eV}$ compared to $E_A=0,97\text{eV}$ for those used "as deposited" without treatment. Table 3.5 gives an overview of the values found in the literature. An extrapolation of the measurement results for the meander structure has permitted the extraction of an activation energy value $E_A=0,39\text{eV}$ to be used within the simulations.

3.3 Aluminum thin film electrical characterization of the samples

In order to investigate the time-dependency of the matter migration phenomena, the retrieval of the electrical resistivity of the material composing the metallization structures is necessary. The divergence value governing the degradation process is proportional to the local resistivity ρ as described in chapter 3. The determination of the different material properties to be used in the simulator should be precise as possible to avoid strong error estimations between lifetime measurements and calculations. The measurement of the electrical resistivity of the conductor of the meander structure was performed with help of the four points method [45], giving a resistivity ρ_0 of $4,68\Omega\text{cm}$ at a room temperature T_0 of 30°C . The Temperature Coefficient Resistance (TCR) associated to the material used for the samples was determined as $3,37\times 10^{-3}/\text{K}$.

The electrical resistivities of the silicon and the silicon dioxide were set constant and taken from the literature [46]. A value of $4,4\times 10^2\Omega\text{cm}$ was taken for silicon, and a value of $10^{14}\Omega\text{cm}$ for the silicon dioxide. Table 3.6 lists the electrical resistivity for each material composing the samples for the meander structure as well as for the SWEAT structure.

| Material | Electrical resistivity | |
|------------------|-------------------------------------|--|
| Al(1%Si) | $\rho_{Al}=\rho_0(1+\alpha(T-T_0))$ | Meander: $\rho_0=4,68\mu\Omega\text{cm}$, $T_0=30^\circ\text{C}$, $\alpha=3,37\times 10^{-3}/\text{K}$ |
| | | SWEAT: $\rho_0=2,76\mu\Omega\text{cm}$, $T_0=30^\circ\text{C}$, $\alpha=3,9\times 10^{-3}/\text{K}$ |
| SiO ₂ | $10^{14}\Omega\text{cm}$ | |
| Si | $4,4\times 10^2\Omega\text{cm}$ | |

TABLE 3.6. Electrical resistivity of the aluminum metallizations.

3.4 Thermal conductivities of the used materials

The values of the thermal conductivities for the different materials have been taken from the literature [46]. They are considered temperature dependent in the simulations, first due to the range of temperature in which the samples are supposed to run and second because they vary with the temperature. Moreover, their values have to match those of the materials composing the samples. Some investigations on thermophysical properties of thin film material has been performed [47] and the thermal conductivity value of the silicon dioxide layer is reduced by 20%. A good correlation between measurements and simulations can be obtained in this case. The thermal conductivity values for each different materials are listed on the following table as a function of their temperature.

| Temperature[K] | Al(1%Si) [W/mK] | Thermal SiO ₂ [W/mK] | Si [W/mK] |
|----------------|--------------------|------------------------------------|--------------|
| 200 | 235 | 0,912 | 264 |
| 300 | 237 | 1,1 | 148 |
| 400 | 240 | 1,208 | 98,9 |
| 500 | 237 | 1,296 | 76,2 |
| 600 | 232 | 1,4 | 61,9 |
| 700 | 226 | 1,536 | 50,8 |
| 800 | 220 | 1,736 | 42,2 |
| 900 | 213 | 1,984 | 36 |

TABLE 3.7. Thermal conductivities of the different materials.

3.5 Mechanical and thermomechanical properties of the used materials

The mechanical stress induced voiding in metallization structures is effective under direct local mechanical loads and/or thermomechanical stress. In this work, only thermally induced stress is taken into account. When the metallization structures are tested, the differences in the CTE of each material causes the appearance of mechanical stress. To calculate these level of stress within the structures, the implementation of the mechanical data for the different materials is necessary. Data like the Young modulus E as well as the coefficient of thermal expansion α_l are taken from the literature [46] and considered temperature dependent. The table bellow lists the mechanical properties of each material of our samples as a function of the temperature.

| Temperature [K] | Young modulus [Gpa] | TCE $\times 10^{-6} [K^{-1}]$ | | |
|-----------------|---------------------|-------------------------------|-------------------|----------------|
| | E_{AlSi} | $\alpha_l(Al)$ | $\alpha_l(SiO_2)$ | $\alpha_l(Si)$ |
| 200 | 6,99 | 20,3 | 0,348 | 2,24 |
| 300 | 6,89 | 23,23 | 0,498 | 2,64 |
| 400 | 6,69 | 25,1 | 0,61 | 3,2 |
| 500 | 6,038 | 26,4 | 0,63 | 3,5 |
| 600 | 4,78 | 28,4 | 0,59 | 3,7 |
| 700 | 3,987 | 30,9 | 0,53 | 3,9 |
| 800 | 3,5 | 34 | 0,47 | 4,1 |

TABLE 3.8. Temperature dependent mechanical properties of aluminum.

The Poisson ratio ν of the different materials is considered constant with the temperature and their values have been taken from the literature. The different Poisson ratios ν and the Young modulus value E for silicon and silicon dioxide are listed in the table bellow.

| Poisson ratio (ν) | | | Young modulus (E) [GPa] | |
|-------------------------|------------------|------|-------------------------|------------------|
| Al | SiO ₂ | Si | Si | SiO ₂ |
| 0,34 | 0,18 | 0,45 | 98,7 | 64,72 |

TABLE 3.9. Young modulous and Poisson ratio of the used materials.

4. Static analysis and failure location determination

In this chapter, the static analysis of the structures will be presented. The investigations are performed with the Finite Element Method (FEM) code ANSYS for the analysis of the different degradation mechanisms. This program is particularly useful for the determination of thermoelectrical as well as for the thermomechanical response and the behaviour of microsystems. The geometry description of the investigated metallization structure have been given in chapter 1. At first, the method describing the static analysis steps is presented through a detailed flowchart. Then, the thermoelectrical analysis results for the meander structure are exposed. In parallel, the behaviour of the different electrical and thermal parameters under different load conditions are investigated and their modelling are given. This part of the work needs to be considered for a better understanding of the different degradation mechanisms during the early stage of the metallization structures degradation. The variation of temperature gradients are analysed under different charge. Afterwards, the investigation of the induced thermomechanical stress on the meander structure is exposed. In the same time, the influence of the applied current on the thermomechanical stress is analysed and a mathematical model is given. In the third part of this chapter, the massflux divergence distribution is presented for the both investigated structures and the failure location determination is provided. Finally, the influence of the electromigration compared to the thermomigration as well as the stressmigration is studied and presented as a function of their ageing accelerated test conditions. The results obtained from the modelling work in this chapter will be used in the last chapter in order to extract some reliability degradation indicators.

4.1 Static analysis flowchart for the massflux divergence value distribution

The massflux divergence value distribution needs to be determined in order to provide some information about the failure location within the metallization structures. The flowchart to achieve this goal is built through different steps as presented in figure 4.1. At first, the finite element model need to be defined for the thermoelectrical analysis. Then the corresponding local results are extracted and saved in text format files. In a next step, the thermal solution of this analysis is used to perform the thermomechanical simulation. It follows a step for the extraction of the thermomechanical results to be used in the hydrostatic stress gradient calculation. Finally, the massflux as well as the total massflux divergence

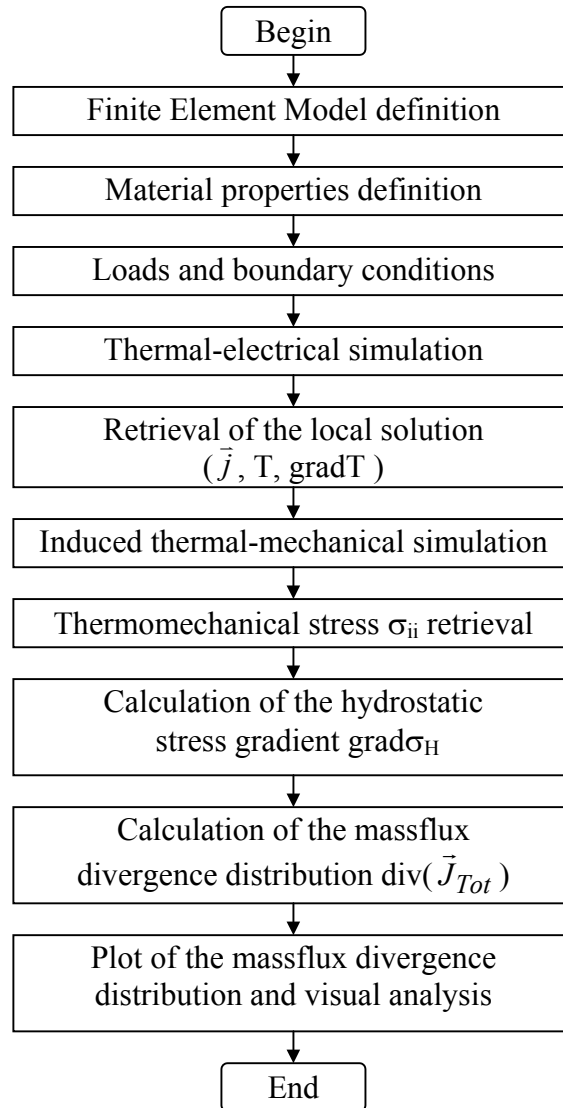


FIGURE 4.1. Algorithmic representation of the static analysis step.

value distribution is computed by an external Fortran user's routine and plotted within the program ANSYS. The results provided by the thermoelectrical analysis as well as the thermomechanical investigation are indeed as entrance parameters for the massflux divergence values calculation function, and their calculation has to be the more precise as possible. More importantly, their values fixes the degradation velocity at the beginning of void formation like it will be presented in the next chapter. Consequently, the static thermoelectrical and the thermomechanical analysis are the basic steps for the time-depending simulation process of void formation in metallization structures. To do so, the results of these investigations are presented in the next parts of this chapter. In parallel, a characterization work has been performed and the corresponding results are also presented and will be used in the last part of this work for the reliability modelling.

4.2 Thermoelectrical behaviour analysis by FEM

The thermal-electrical analysis is one of the most important phase study of this research work. Indeed, the time-dependency of matter migration is function of the diffusion velocity and this value is strongly dependent with the temperature. Consequently, the results obtained by the simulations need to match as better as possible the results obtained during the experiments. The theoretical analysis done by FEM was made for different loads in order to compare the measurement and the simulation results. The results of the thermal-electrical analysis is presented here for both the meander and the SWEAT structures. Due to symmetry in the geometry of the fabricated tests samples, only relevant parts for the finite element

model were considered. The substrate temperature is taken to be 180°C for the meander metallization structure as used in the experiments. The SWEAT structure was investigated at

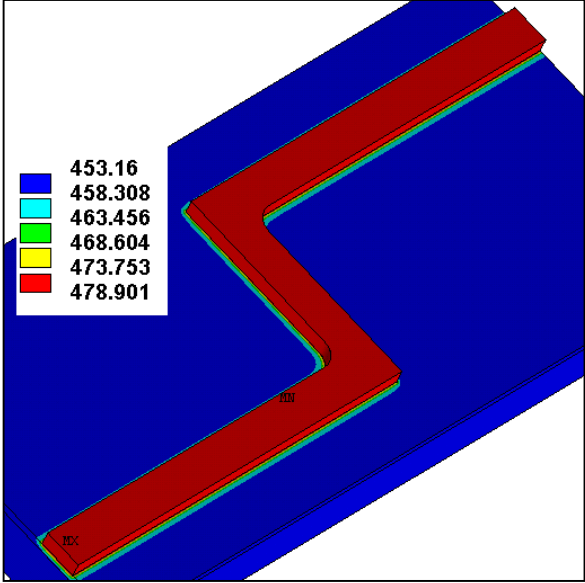


FIGURE 4.2. Temperature distribution on the meander structure under 100mA [K].

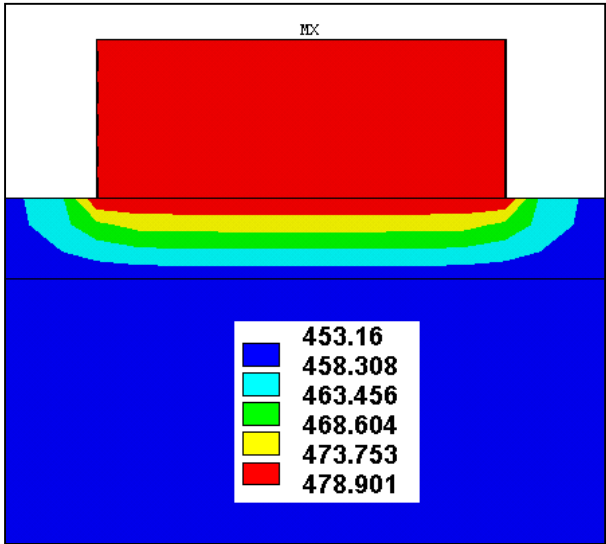


FIGURE 4.3. Temperature distribution at the interface region Al/SiO₂ [K].

room temperature. The simulation results for the SWEAT structure were found in good agreement with previous results published in the literature [48].

Figure 4.2 gives the temperature distribution found in the study of the meander structure under an applied current of 100mA. The temperature distribution shows a concentration of high temperature value on the metallization structure. This fact is due to the highest thermal conductivity value of aluminum compared to the other materials of the chip. Unfortunately, the thermal conductivity of the silicon dioxide between the aluminum and the silicon substrate represents a thermal barrier for the energy produced by the Joule self-heating effect of the metallization

structure and brakes the heat flow through the different material layers. It results in the appearance of some strong temperature gradients at the interface formed by the metallization and the silicon dioxide layers like presented in figure 4.3. When a current flows within a metallization structure, the geometry induces some differences on the value and the direction of the local current density distribution as shown in figure 4.4. The maximum value was found in the inner corner of the meander structure due to the short electrical path generally taken by the electrons flow. The maximum value of the current density is determined at the inner corner of the metallization structure. The current density at this location have to be taken into account carefully since the electromigration phenomena appears above a particular level of current density for aluminum metallization structure. This value was found to be 10^4A/cm^2 for aluminum. The current density distribution also provides some information on this value along the metallization and the distribution seems to be the same in the Z direction. In this case, an evaluation of the current density distribution can be done in a two-dimensional analysis. This evaluation can be carried out by the utilisation of the 2-D conform transformation on the simplified plane metallization structure represented given by figure 4.5. The structure is represented with a metallization part of width h , the inner radius r and the other metallization part with a width g . The maximum current density in "A" has been calculated and proposed in the literature [33,49] for low current density values as given by the following equation (4.1). J_{ein} corresponds to the global current density value

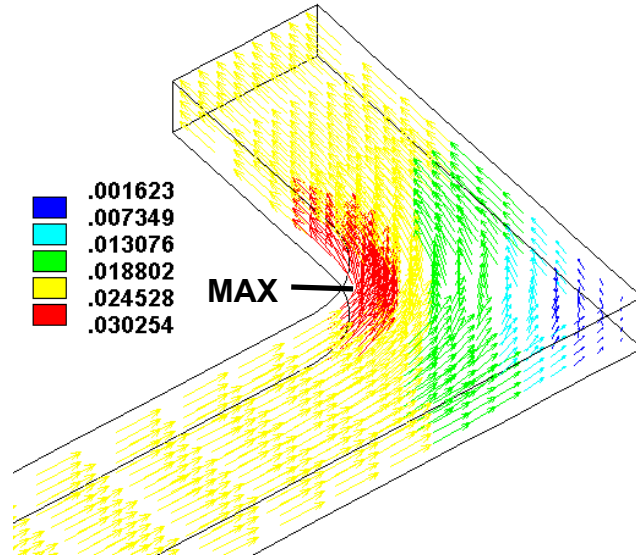


FIGURE 4.4. Current density distribution within the meander structure under 100mA [$\text{A}/\mu\text{m}^2$].

in the metallisation structure away from the inner corner and J_{max} gives the current density value in the corner at the point "A". S is a parametric factor ratio between the widths at each

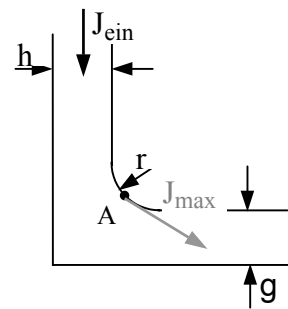


FIGURE 4.5. 2-D representation of the meander structure.

by the following equation (4.1). J_{ein} corresponds to the global current density value in the metallisation structure away from the inner corner and J_{max} gives the current density value in the corner at the point "A". S is a parametric factor ratio between the widths at each

$$J_{max} = 1,04 \left[\frac{S^2 + 1}{PS^2} \right]^{\frac{1}{3}} J_{ein} \quad (4.1)$$

side of the corner and is defined by $S=g/h$. P represents the ratio between the radius r and the width h of the vertical part and is given by $P=r/h$ (with $r \ll h$). By this way, an approximation of the local current density at the inner corner of the metallization is possible. For the meander structure, these parameters are calculated and found to be $S=1$, and $P=0,41$. The current density J_{ein} is calculated to be $17,50\text{mA}/\mu\text{m}^2$. Then, the calculation by equation (4.1) predicts a ratio between the applied current density J_{ein} and the maximal local value J_{max} to be $J_{max}=1,75J_{ein}$. A maximal current density in “A” of about $30,7\text{mA}/\mu\text{m}^2$ would be determined by this method. This value is found in good agreement with the simulation results given in figure 4.4, where a fine meshing was performed in the corner area of the metallization structure. The consideration of equation (4.1) is in this study very important because it gives some indications in the limitation of the maximal current density J_{max} for the meander structure compared to the electromigration phenomena.

Because of the important differences in the thermal conductivity values of the different materials used for the fabrication of the test samples, an elevation of the temperature out of the joule self-heating effect of the metallization structure is expected. In addition, some strong temperature gradients are able to occur within the aluminum material. Indeed, temperature gradients has been reported to be one active driving force playing in the degradation of metal interconnect used in VLSI circuits [50]. The simulation result of the temperature gradient distribution for the meander structure under 100mA is given in figure 4.6. The maximum value is found to be at the external corner of the metallization structure and located at the metal-oxide interface. Some important values of temperature gradients are also calculated from this location of the model and decreasing continuously along the border of the metallization with the rest of

the structure. The thermoelectrical calculation has shown that the small part area of the structure and the large part area of the structure were warmer than the part formed by the external corner of the structure, and explains the temperature gradient distribution obtained in this case.

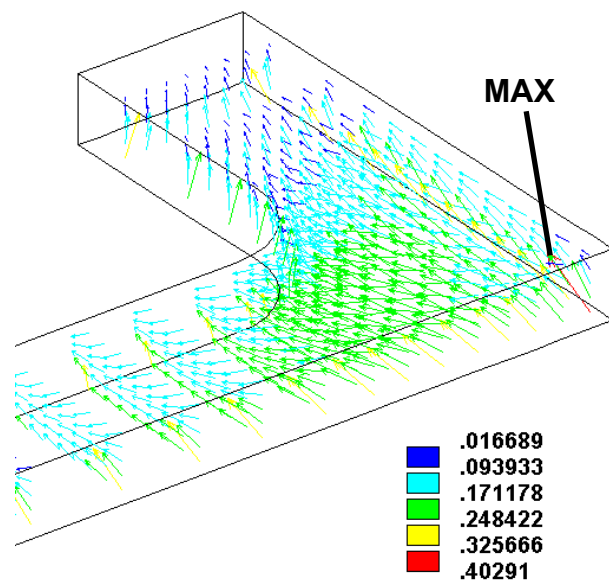


FIGURE 4.6. Temperature gradient distribution on the meander structure for 100 mA [$\text{K}/\mu\text{m}$].

4.2.1 Influence of the current density on the metallization temperature

In order to model the influence of temperature gradients on the degradation phenomenon, a determination of the temperature gradient induced by the current density is necessary. The temperature elevation is caused by an increase in the electrical resistivity of the aluminum with the temperature through the Joule self-heating phenomena. The divergence values of the different

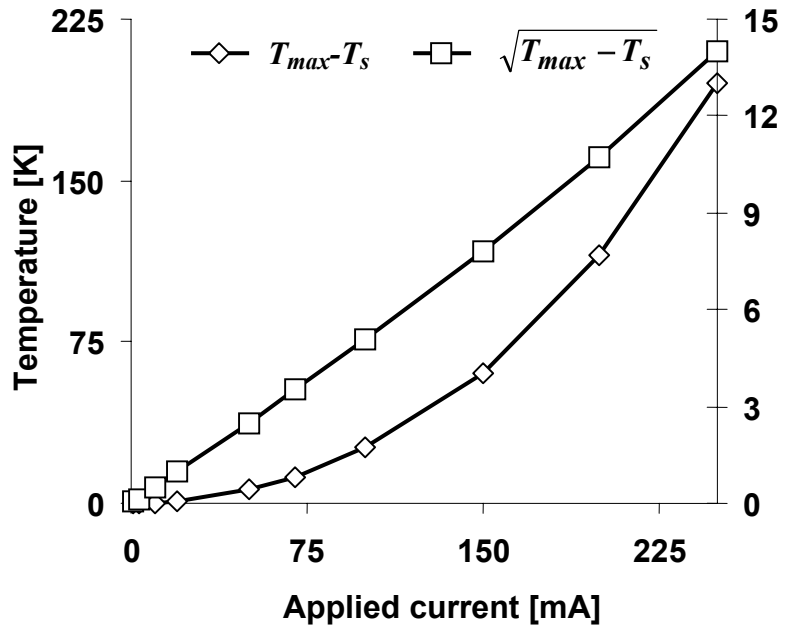


FIGURE 4.7. Influence of the applied current on the metallization temperature.

degradation phenomena is influenced by the temperature like previously shown by equations (2.11), (2.16) and (2.19). The temperature variation with the applied current density has already been studied [51], where a quadratic form has been modelled and the difference between the maximum temperature value of the metallization and the ambient temperature was found to have a proportionality to J^2 .

This variation is carried in this study, and
$$T_{max} - T_s = \beta J^2 \quad (4.2)$$

the temperature variation for the meander

is given in figure 4.7. The results shows the influence of the current density on the temperature level reached in the metallization structure. The square root of the temperature difference between the metallization T_{max} and the substrate temperature T_s is also given and found quasi-linear with the current density J . In this case, equation 4.2 can be written, where β is a constant.

4.2.2 Influence of the current density on the temperature gradient in the metallization structure

As explained previously, temperature gradients occur within the metallization structure under strong level of electrical charge. Since the temperature vary with the level of

the current density in the interconnect, the temperature gradient variation is coupled with the increase

$$|\text{grad}T| = \gamma J^2 \quad (4.3)$$

in temperature. This variation was also studied in this work for the meander structure. The results obtained by simulation is presented in figure 4.8 and shows a quadric dependence of the temperature gradient with the current density J again. The temperature gradient can

then be modelled as a function of the current density, like given by equation (4.3), where γ is a constant. This equation shows that the temperature gradient in the metallization structure increases quadratically with the current density J .

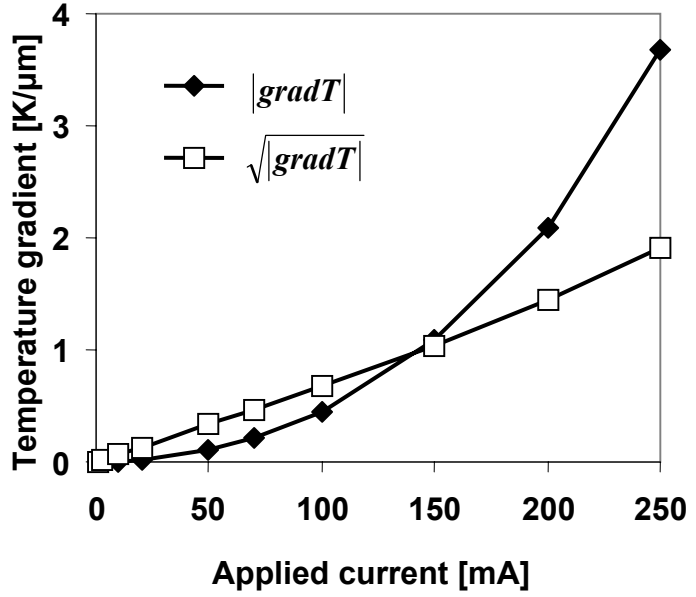


FIGURE 4.8. Current density influence on the temperature gradient.

4.2.3 Influence of the temperature on the electrical parameters

When the metallization structure is supplied, the electrical current flowing within the structure induces a warming of the aluminum metallization. Well-known as the Joule self-heating phenomena, the temperature elevation can influence the electrical resistance of the interconnect. The material used for the fabrication of the sample has a temperature coefficient resistance (TCR) like most of the conductor materials. An increase of the temperature within a chip induces a resistance change which is able to degrade the performances of the system. The variation of the maximum voltage V_{max} with the applied current is given by figure 4.9 extracted from simulation results. The results show an increase in the maximum value with the applied current. In fact, this evolution corresponds to the effect of the temperature on the electrical resistance value. In order to understand the effect of the temperature, the difference between the real evolution $V(I)$ and the voltage evolution without temperature consideration $V(I)-R_0I$ is studied and presented in figure 4.9, where R_0 represents the resistance measured at substrate temperature and I the applied current flowing within the metallization. At 250mA, the contribution of the temperature is determined to be strong in the electrical resistance

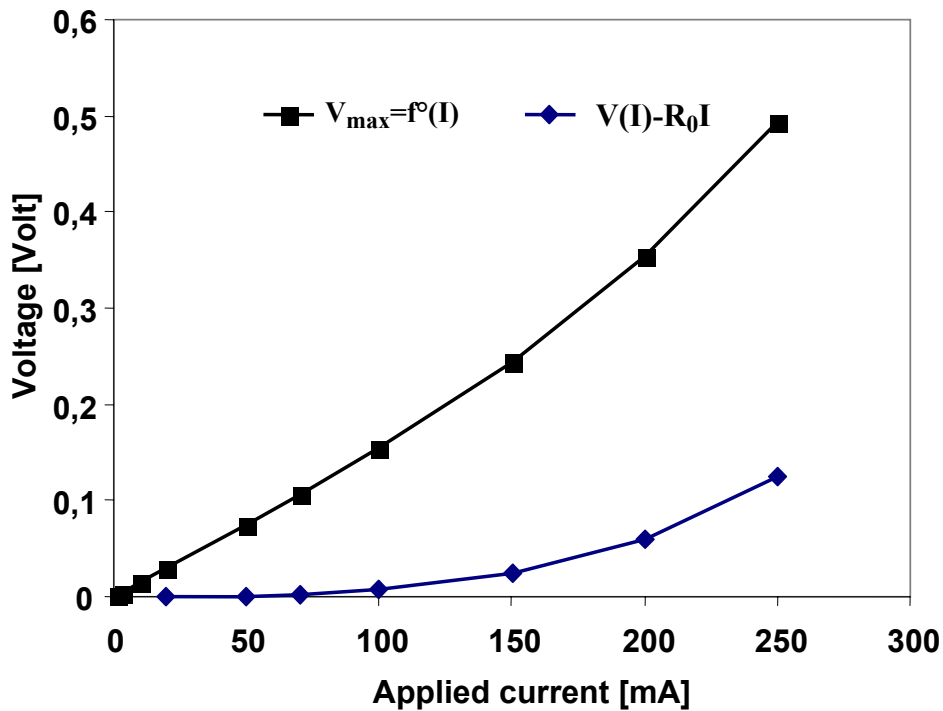


FIGURE 4.9. Maximum voltage as a function of load.

evaluation of the metallization structure and to be more than 20% above $4,3\text{MA}/\text{cm}^2$. This demonstrates that the current density within the metallization structures integrated in a chip can have an important impact on their electrical performances caused by an elevation of the temperature. A local temperature elevation during the void growth within a metallization structure consequently influences the time where the structure is considered failed, because of the resistance elevation due to the temperature.

4.3 Thermomechanical simulation over the metallization structures

When an integrated circuit is supplied, the global electrical resistance due to the conductor lengths runs as a heat source in the chip and power dissipation can reach today some values up to 80 Watts [52]. A part of the energy produced by power consumption and due to Joule self-heating of the chip is dissipated through the thermal conduction process. In the same time, the materials composing the chip are dilating. The deformation depends on the geometry and on the thermomechanical property α_1 of the materials. This value is represented by the CTE (Coefficient of Thermal Expansion). A difference in the CTE of two different materials assembled together is susceptible to create some thermomechanical stress.

4.3.1 Thermomechanical simulation of the structures

The thermomechanical behaviour of the samples was studied for the stressmigration contribution to the matter migration phenomena. The massflux produced by stressmigration is given by equation (3.3) and shows a proportionality to the local value of the hydrostatic stress gradient $grad\sigma_H$. The thermal-electrical solution have been used for coupled field analysis with the ANSYS program to determine the mechanical response of the unpassivated structures. The meander and the SWEAT structures are considered to be free of mechanical stress at room temperature and completely relaxed. The experiments were performed under an environment temperature of 180°C for the meander. The accelerated tests for the SWEAT structure were made at room temperature. For both structures, the symmetry and the different planes have been used to set the boundary conditions for the thermomechanical stress

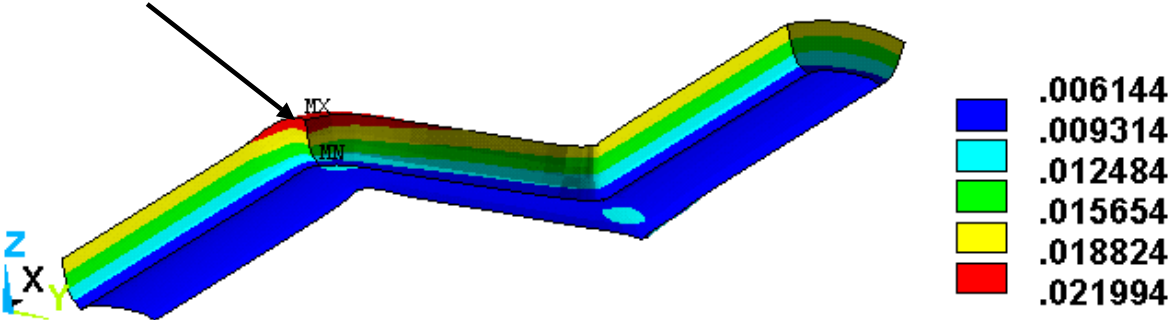


FIGURE 4.10. Bending effects and global expansion of the meander structure [μm].

calculation. The bending effects caused by high temperature over the meander structure is presented in figure 4.10. and is found in agreement with previous experimental investigations [53]. This figure shows the global expansion of the metallization structure under the joule self-heating phenomena. The dilatation of the external corner, located at the top of the structure, is found to be maximum with about 22nm like shown in figure 4.10. The equivalent stress distribution (Von Mises stress) for the meander structure shown in figure 4.11. has been also calculated. The distribution shows some high stress level at the inner corners of the metallization (about 500MPa) as well as at the interface between the metal line and the SiO₂ layer. Some strong level of stress are expected to appear in the inner corners because they are the meeting point of two orthogonal part of the metallization which are expanding under the effect of the high temperature. The stress in these areas are of the compressive type. Those

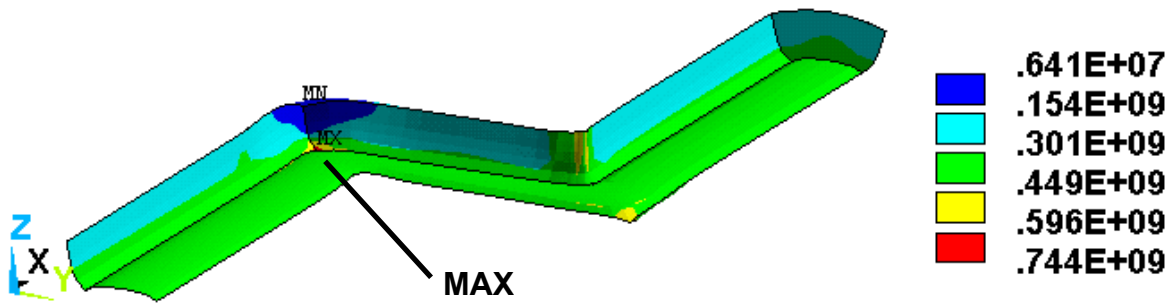


FIGURE 4.11. Thermomechanical stress over the meander structure [Pa].

found at interface location and within the metallization structure belong more to mechanical stress due to the CTE mismatch between Al and SiO₂. Some compressive stress is also determined there. The maximum value is found to be located at the corner of the structure and at the interface (~750MPa) like shown on figure 4.11. The values usually reported in the literature are given to be between 350 and 450 MPa for systems running at room temperature. The stress evaluation takes into account the additional stress generated by the temperature offset of 180°C for the meander structure and justify the important value found here. In the next subpart of this chapter which deals with the influence of the applied current on the thermomechanical stress behaviour of the structure, the stress evaluated will be discussed. A comparison between the analysis of the SWEAT structure and the meander structure will be also presented.

4.3.2 Determination of the gradient of the thermomechanical hydrostatic stress

The hydrostatic stress corresponds to the stress formed by mechanical pressure strength. It is defined by the average value of the normal components of the mechanical stress. The massflux due to mechanical hydrostatic stress is proportional to the gradient of the hydrostatic stress (equation 3.3). The calculation of the hydrostatic stress gradient was programmed as an external Fortran user routine, which uses the finite element method. The same program was applied to the calculation of temperature gradients and compared with the ANSYS simulation results for the verification. The hydrostatic stress gradient distribution calculated for the meander structure under 100mA at 180°C is given in figure 4.12. The maximal hydrostatic stress gradient values are mostly found at the interface. A maximum value of more than 750MPa/μm is found at the corner of the metallization and at the interface.

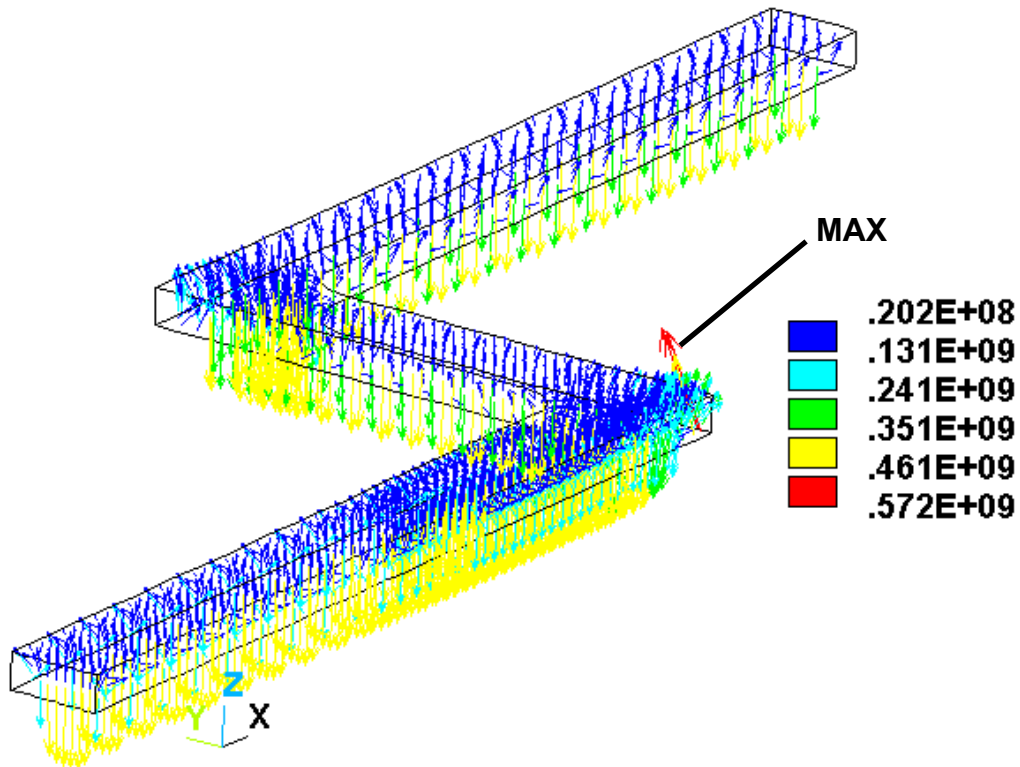


FIGURE 4.12. Mechanical hydrostatic stress gradient over the meander structure [Pa/ μm].

4.3.3 Influence of the applied current on the thermomechanical stress

In order to characterize the thermomechanical induced stress, an investigation is performed to determine their values with the applied current density within the metallization structure. The investigation is carried out by simulation with applied currents up to 250mA. As said before, the structure has been tested in an environment temperature of 180°C. In this case, an offset in the stress is expected to appear over the metallization when no current is applied, because of the temperature offset between the relaxation temperature T_a and the temperature at which the investigation were made T_s ($T_s - T_a = 180^\circ\text{C}$). The maximum value of mechanical stress (Stress von Mises σ_V) and the extracted hydrostatic stress gradient $|\text{grad}\sigma_H|$ as a function of the applied current obtained per FEM analysis is given in figure 4.13. The results confirm the presence of the shift in the mechanical stress induced by the temperature environment. The maximum value of the equivalent stress is found to be about 650MPa when no current is applied and the maximum value of the hydrostatic stress gradient is determined to be around 500MPa/ μm . Then, their value rise in a quadric form with the

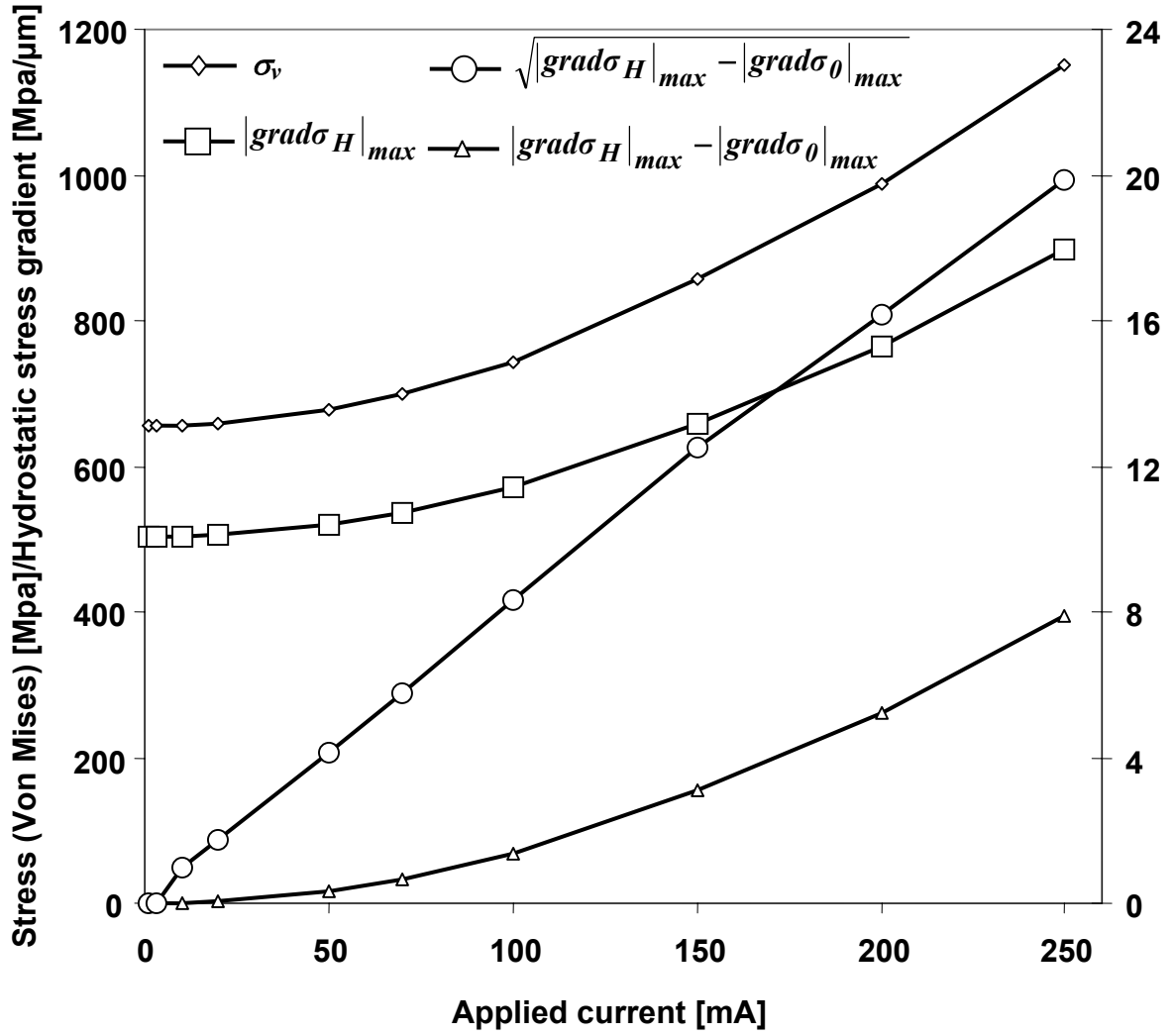


FIGURE 4.13. Maximum stress and hydrostatic stress distribution with the applied current.

applied current respectively to more than 1,1 GPa for σ_V and about 900 MPa for the hydrostatic stress gradient $grad\sigma_H$. A graphical analysis of the results suggests that the variation of the hydrostatic stress gradient is proportional to J^2 . In this case, the dependence of the thermomechanical induced hydrostatic stress gradient can be modelled by the following equation (4.4) where φ is a numerical constant:

$$|grad\sigma_H| = |grad\sigma_H|_{J=0} + \varphi J^2 \quad (4.4)$$

The gradient of the mechanical hydrostatic stress is found to be a function of the boundary conditions and is determined to increase quadratically with the applied current density J .

4.4 Failure location determination over the investigated structures

The determination of the failure location can be done by studying the massflux divergence distribution of the ionic particles. The divergence expressions have been given and calculated in chapter 3. In this study, the massflux divergence taking into account the effect of the atomic concentration variation distribution will not be considered. In this case, the divergence distribution investigated here gives some important indications about the start status of the time-dependent phenomena. The investigated structures have already been presented in chapter 2. The massflux divergence values distribution is obtained by the implementation of equation (2.22) in the algorithm presented previously in figure 4.1. A summary of the specific physical parameters for the aluminum alloy used in the divergences calculation of this study are given in table 4.1.

| | |
|---|------------------------|
| Self-diffusion coefficient D_0 | 1,71cm ² /s |
| Activation energy E_A for the meander structure | 0,39eV |
| Activation energy E_A for the SWEAT structure | 0,70eV |
| Effective charge number Z^* | -10 |
| Specific heat of transport Q^* | -2kcal/mol#-0,0867eV |

TABLE 4.1. Specific physical parameters for the divergence calculation.

The others parameters such as the thermomechanical properties for the silicon and the silicon dioxide materials as well as the electrical properties of the aluminum alloy for the both structures have been given in chapter 3. The simulations made with the Multiphysics tools ANSYS take into account the temperature dependence of the physical properties for the different materials. Figure 4.14 presents the divergence distribution obtained for the meander structure. The distribution is represented here by a backside view of the metallization structure. The maximum value is found at the interface between the structure and the silicon dioxide layer. It indicates a start of void formation at the interface under the metallization itself. These results confirm some experimental observations reported in the literature, where the phenomena has already been detected at interfaces [54]. Figure 4.15 represents the divergence distribution obtained for the SWEAT structure under 150mA at room temperature. The maximum value indicates a failure location within the metallization line of the structure. The failure location is determined within the line of the structure and confirms previous

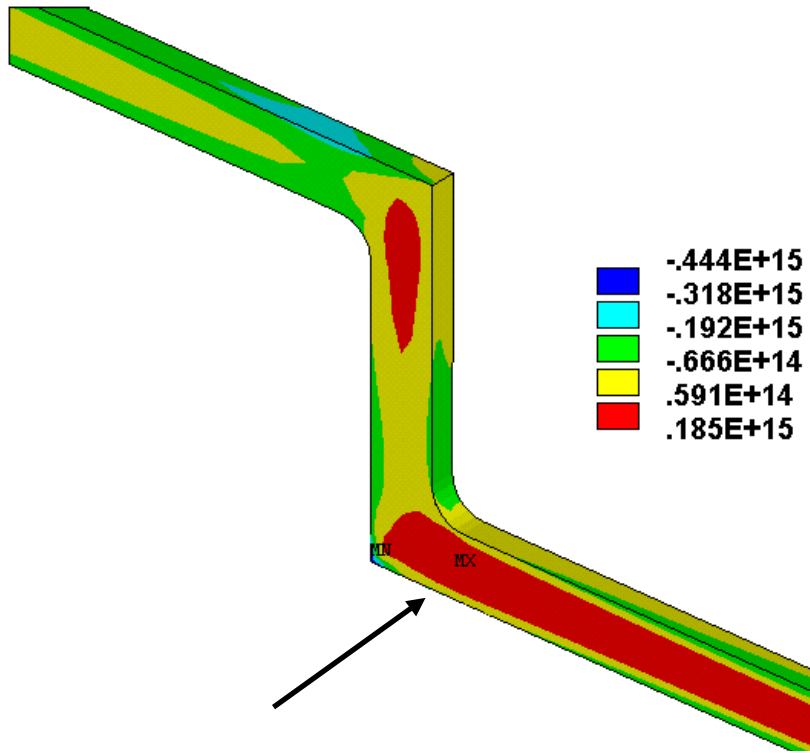


FIGURE 4.14. Backside view of the massflux divergence distribution over the meander structure [$1/\mu\text{m}^3\text{s}$].

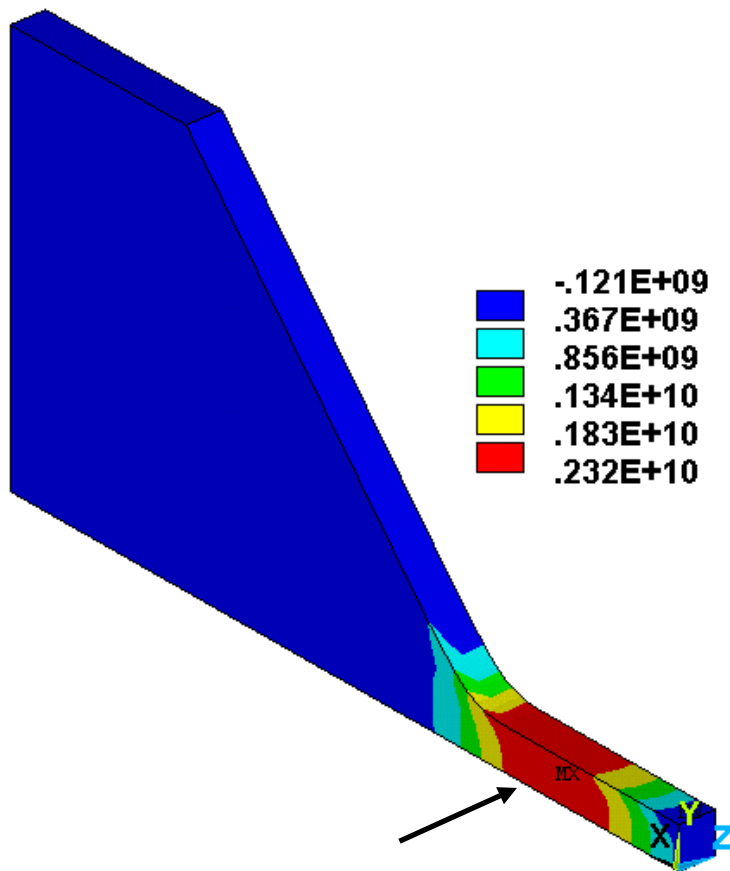


FIGURE 4.15. Backside view of the massflux divergence distribution over the SWEAT structure [$1/\mu\text{m}^3\text{s}$].

studies where the influence of the current density as well as temperature gradient distributions on the degradation site has been demonstrated [55]. The results obtained in this study confirm a start of void formation at the Al/SiO₂ interface again.

4.5 Influence of the different migration effects

One aspect of this study is the determination of the different influences that contribute to the void formation induced failure in the metallization structures. This determination can be done by simulation comparing the divergence values of the different effects with the total divergence value. However, the electromigration phenomena has been the most investigated phenomena in the study of interconnects reliability. The goal of this analysis is to show the importance of the thermomigration and the stressmigration in the determination of the different factors which influences the reliability of the metallization structures. The static analysis results for the both structures are presented here under different running conditions.

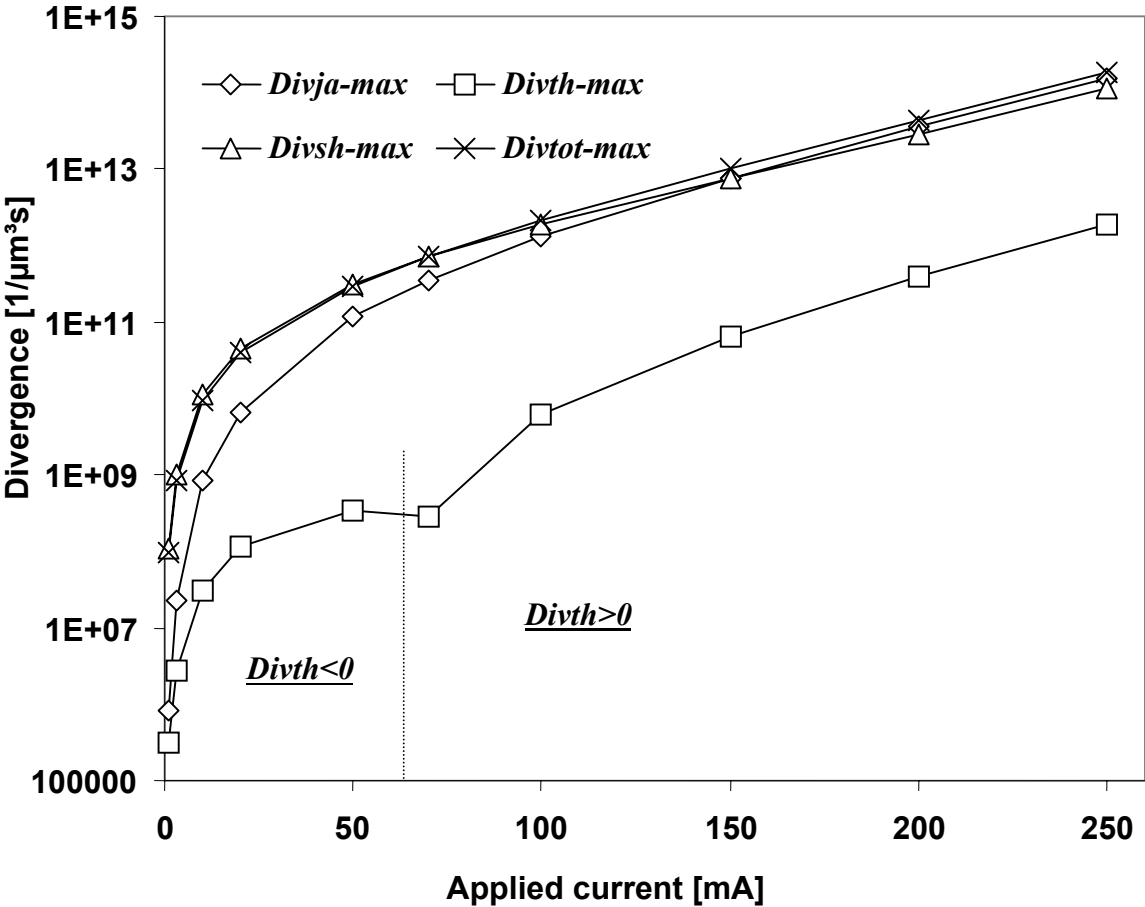


FIGURE 4.16. Influence of the different type of migration for the tested meander structure [1/μm³s].

The meander structure was investigated with a substrate temperature of 180°C and the SWEAT structure studied at room temperature. Figure 4.16 gives the massflux divergence maximum value distribution for the different types of migration depending on the applied current. The influence of the thermomigration is found particularly weak (~1%) compared to the electromigration and the stressmigration. The influence of the migration due to thermomechanical induced stress is determined to be the strongest. This is caused by the substrate temperature level of 180°C at which the metallization structure was tested. Under a level an applied current of 150mA, the stressmigration plays a more important role in the degradation phenomena, whereas the electromigration dominates the degradation above this value. The inflexion point shown at 70mA is due to the negative values in the divergence of the thermomigration for applied current below this value. The simulation results obtained for the SWEAT structure are presented in figure 4.17. The participation of the migration due to the thermomigration is found to be less than 1%. The stressmigration acts only for less than 10% at the start of the degradation. The electromigration is the most important driving force in the start of the degradation activity of the metallization structure.

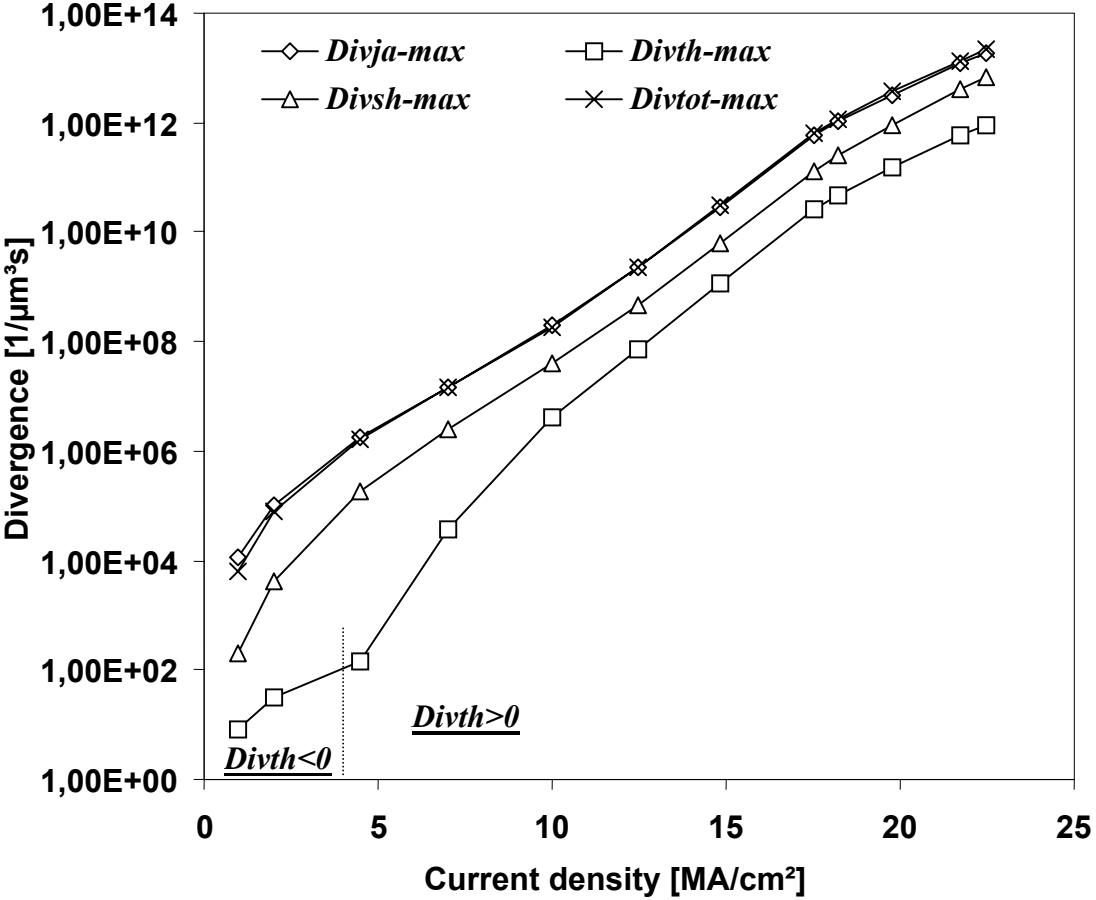


FIGURE 4.17. Divergence value distribution of the different migration effects on the SWEAT structure [1/μm³s].

Finally, some guidelines seem to emerge from the static analysis performed on the meander and the SWEAT structures. At first, the maximal divergence value associated to the failure location determines the failure location and gives some indications on the velocity of the degradation start for void formation in the metallization structures. Indeed, the mass flux divergence expresses a variation of ions per unit volume and per second [$1/\mu\text{m}^3\text{s}$]. This value plays an important role in the time-dependency determination of the degradation, as it will be described in the next chapter. In this part, the influence of the different type of migration effects have been presented and compared. The study shows that the stress migration can be one of the most important induced failure mechanism within metallization structures, like for the meander structure. The electromigration can mainly affect the reliability of metallization structures due to the weak influence of the thermomigration like demonstrated for the both structures. The influence of the different failure mechanisms in the degradation of metallization structures seems to depend on their geometry, the different used materials and also on their working conditions.

5. Study of the time-dependency: development of a void formation simulator

The fast degradation of metallization structures within the integrated circuits corresponds to an acceleration and to the amplification of the diffusion phenomena of ions due to some mechanical induced driving forces. These forces have different origins as previously presented in chapters 1 and 2. The phenomena occurs generally when some running parameters like the current density, the temperature and the thermomechanical induced stress take place and act unfortunately on the material of the metallization structures. This chapter focuses on the time-dependency analysis of the phenomena, using available tools like simulation programs and study the possibility of its implementation for computer analysis. The important results from the previous chapter are considered as basics for the time-dependency analysis and the development of a 3-D simulation tool of void formation in metallization structures. In this chapter, an analysis of the experimental observations is first presented. Then, some guidelines and an interpretation are extracted from the experimental observations and are provided for the definition of the voids simulation method. After that, the method used for 3-D simulation of voids in the metallization structures is presented. Then, a method for the time-dependency calculation of the void formation is provided. The chapter ends with the presentation and the description of the developed algorithm for the time-depending void formation simulation.

5.1 Analysis of the experimental observations

The start point of the degradation induced by void formation in the metallization structures corresponds to the nucleation phase. As shown on figure 1.4 in chapter 1, the nucleation phase shows the beginning of the void formation caused by an induced atoms diffusion at this location. Referring to chapter 4, the divergence in the atomic massflux in the static analysis shows the maximum at this location and this area will be depleted by a certain amount of matter. It appears remarkably near the border of the metal line and particularly near a region where the metal line geometry shows strong changes in its geometry. The observation of the metal line also reveals some important dispersion along the border of the line itself due to the etching phase of the fabrication process. The void growth within the metal line accelerates and the material around the nucleation void seems to disappear letting

place to an extension of the initial void. The experimental observation shows that the depletion continues to develop as the void growth continues to degrade the metal line integrity following a specific and orthogonal direction with the current flow. In addition, the formation of hillocks is visible along the surface of the metallization structure. The obtained void also presents some irregularities in its form and its geometry, and suggest that the phenomena is particularly complex. The development path and the growth of the void is given in figure 1.6. The picture reflects a deep development of the void morphology within the metal line, but the direction taken by the void path has changed although it has followed a unique direction until the metal line seems to be half-broken. Obviously, the degradation does not follow a specific way and the evidence of a complex process in the degradation of the phenomena can be confirmed based on experimental observations, although the morphology suggests a random one. The evolution of the void growth may be due to the characteristic of the material that composes the metallization structure, which was polycrystalline aluminum. Polycrystalline aluminum generally presents some grain boundary regions. The void growth may consequently follow the direction formed by these regions associated to a depletion of matter at the grain level. Figure 1.7 represents the void at the limit of an electrical open-circuit. The previous steps in the formation of void is conserved and the void has continued to grow along the structure. In the same time, some extrusions have continued to take place and their volumes have increased as the void volume within the metal line has grew.

5.2 Experimental based extracted guidelines and simulation method

The experimental observations presented previously suggest some hypothesis about for the development of the method of void evolution simulation. The first step in the time-dependency of matter diffusion induced degradation referred to the nucleation phase. This phase is one of the most important activities related to the void formation because it determines globally the failure location start of the degradation. The determination of the failure location can be investigated as presented in the previous chapter. The determination of the failure location is given by the maximum value obtained by the determination of the massflux divergence distribution over the structure. The value of the massflux divergence generally represents the number of ions leaving or coming into a small volume during one second [$1/\mu\text{m}^3\text{s}$]. This description is important since it describes the basics of the matter migration phenomena. A positive value in the massflux divergence indicates a location where

matter depletion inducing void formation is able to happen whereas a negative value reflects a location with particle accumulation causing the formation of hillocks. The appearance of voids as well as hillocks can be considered as volumetric matter displacement within metallization structures running under high current loads. Therefore, the time-dependent observation suggests that the phenomena is a continuous process of degradation, where the removing as well as the accumulation of matter takes place without abrupt changes in void and hillocks morphology. A continuous evolution of the massflux divergence value at the failure location can then be suggested. These hypothesis will be studied for the time-dependency calculation of the phenomena for verification. In addition, the observation of the time-dependent void formation within the meander structure shows something important: the part of the metallization located around the void and insuring the electrical current conduction seems to remain intact and the integrity of the conductive metal line seems to be conserved. This suggests that particles concentration variations only occur at the parts where the void formation happens. Next, a change in the electrical resistance of the metallization structure has been observed during the metal line degradation. Some modification in the electrical resistance is expected due to some modifications in the geometry of the metallization structure when the degradation goes on. These different observations give us the possibility to know more about the void formation in metallization structures and provide some guidelines for the development of an algorithm for void simulation formation. The integration of these hypothesis in the definition of the simulation method for the void formation are presented in the coming part.

5.3 Method description of the void formation simulation

The degradation of the metallization structures revealed that the material is sequentially removed when the void is growing. In the same time, extrusions of matter appear at other sites along the metallization structure. The simulation formation of extrusion is not considered in this study. The static as well as the time-dependent simulation of voids formation can be done using the FEM program ANSYS. This program offers the opportunity to perform some fine meshing where it is desired. One method consists in the preparation of a fine meshing area where the maximum value of the massflux divergence is determined. Then, the divergence distribution is calculated again. Each fine meshed element is affected with a value of the massflux divergence like presented in figure 5.1.

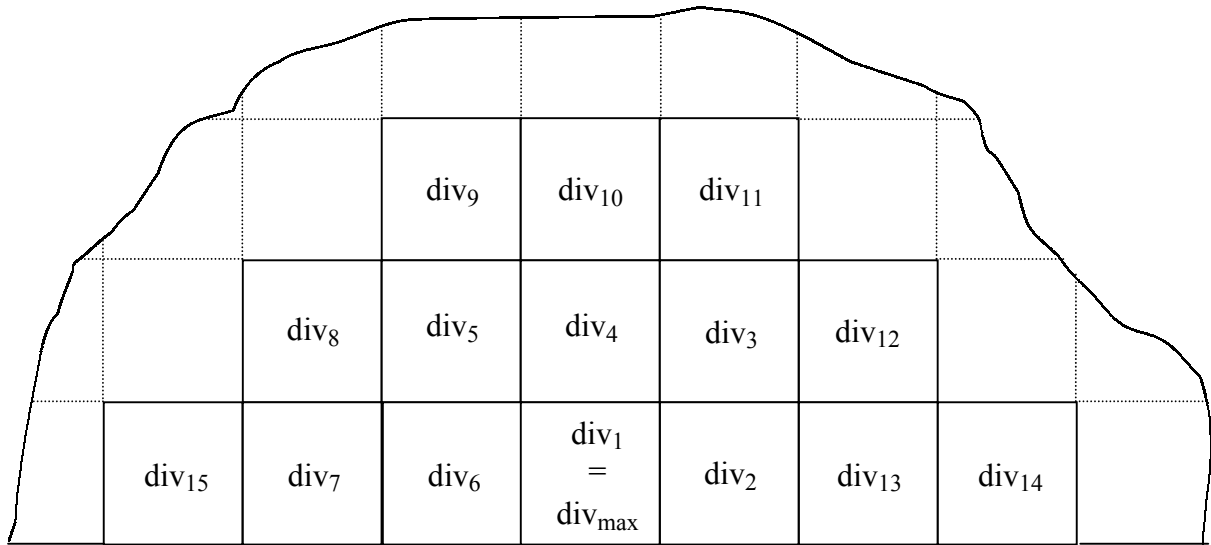


FIGURE 5.1. Schematic representation of a 2-D mesh part area with their element divergence values.

The start of void formation appears where the divergence value is found to be the maximum. The divergence value distribution is given and sorted like the following $div_1 > div_2 > div_3 > div_4 > \dots > div_{14} > div_{15}$. The element with the maximum divergence value can be deleted within the simulation possibility provided by the ANSYS program. After that, the model has to be electrically, thermally and mechanically calculated again and then the divergence distribution needs to be redefined for a new deletion phase. The element found with the maximum value of the divergence is simulated deleted again. The process goes on until the metal line is simulated to be broken. But the calculation and the simulation time would be too long and remain an important problem for the study. To solve this problem, the process of void simulation is modified like presented in figure 5.2. A simplified 2-D part of a conductor is showed. In a first step, a thermoelectrical simulation followed by a thermomechanical simulation is performed in order to obtain the massflux divergence distribution for the structure. From these analysis, the divergence values and the affected elements are sorted again in a decreasing order. Then, a set containing a chosen number of elements which corresponds to those having the higher divergence values are selected for deletion. The method consisting in the deletion of a percentage of elements having their massflux divergence values among the highest one has been rejected because a good control of the void simulation steps number is not possible and doesn't work in all cases. When the deletion process is terminated, the finite element model have to be calculated again and the

next steps of deletion follows until the metal line fails. After each step, a much higher value in the maximum divergence has been found during the simulations steps like represented on

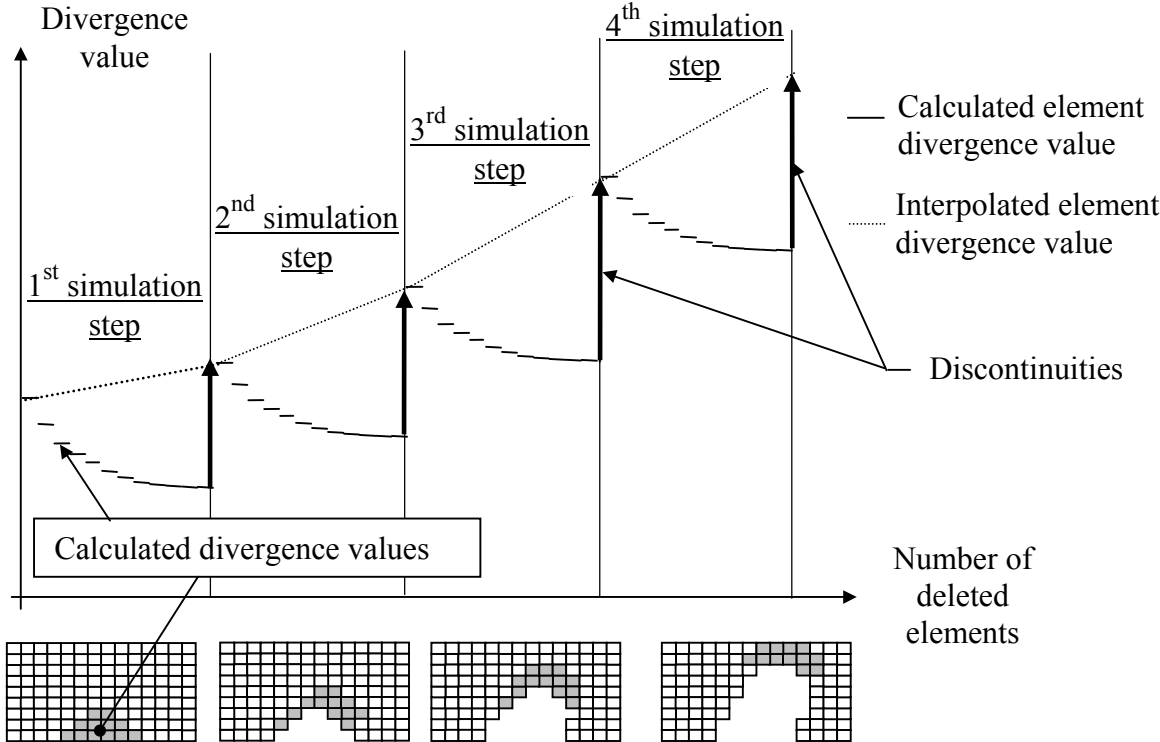


FIGURE 5.2. Calculated and interpolated values method of the massflux divergence.

figure 5.2. This discontinuity is attributed to the change in the metal line geometry after the deletion of the corresponding set of elements for void simulation. A linear interpolation in the maximum value of the divergence value is suggested for the time-dependency evaluation.

Moreover, although the matter displacement can not be well simulated in the grain boundary regions, the method of volumetric amount of matter deletion used in this work should provide very good results. The method simulates the macroscopic degradation globally instead of doing it locally with a microscopic point of view. In addition, the determination of volumetric amount of matter which disappear during the void growth simulation remains difficult due to the random process of meshing at the failure location area. That's the reason why a correlation between the massflux divergence values and the volumetric amount of disappeared material will not be considered in this study.

5.4 Time-dependency calculation of the void simulation

For the time-dependency evaluation, the simulation results as well as the continuity equation giving the relationship between the divergence value and the time of degradation will be used. The continuity equation has been given in chapter 2 in which the theory has been presented. Again, some considerations are needed here to perform the time-dependency calculations. The observations reveals that the matter is removed sequentially from the degradation site. In the most cases, the material depletion takes place at interface or in grain boundary regions. Based on this consideration, the part of the metallization structure where the void appear becomes a region without any presence of matter ($N=0$). Within the metallization structure, the material seems to conserve its integrity where no depletion takes place ($N=N_0$). Else, the simulation results provide some discontinuity on the maximum value of the massflux divergence calculation. But the material is removed sequentially during the degradation process and no discontinuity should take place in the divergence value evolution ideally. To remedy this problem, the maximum divergence value obtained from each analysis step is retained and used to interpolate the maximum divergence value evolution between each step, like represented again in figure 5.2. This process is considered to correct the discontinuity in the values of the massflux divergence. Moreover, the proportionality of the massflux divergence value with the local atomic density N has been noticed during this study and the divergence value given by equation (2.22) can be reformulate like presented by equation (5.1):

$$\text{div}(\vec{J}_{tot}) = N \cdot F(\vec{j}, T, \sigma_H, E_a, D_0, E, \alpha_l, \dots) \quad (5.1)$$

F can be represented as a parametric function taken into account all the calculated parameters provided by the ANSYS program, like the local current density \vec{j} , the local temperature T and the temperature gradient $gradT$ as well as the local value of the hydrostatic stress σ_H and the gradient $grad\sigma_H$. Then, equation (2.5) take the form given by equation (5.2):

$$N \cdot F + \frac{\partial N}{\partial t} = 0 \quad (5.2)$$

The form of the local atomic concentration evolution $N(t)$ is theoretically found to be exponential and determined to be dependent on the parametric function F . This function represents the local massflux divergence value when $N=1$. N is then defined by:

$$N(t) = N_0 e^{-Ft} \quad (5.3)$$

With the previous presented considerations extracted from the experimental analysis and the observations, the time-dependency of the void formation simulation can be determined. To do this, we make the following approximation: due to the exponential form taken by $N(t)$, we consider the element empty of material when the corresponding atomic concentration reaches 10% of the initial concentration N_0 . In this case, the extracted and corresponding time T_i for matter migration to “delete” the element “ i ” is given by equation (5.4):

$$T_i = \frac{1}{F_i} \ln 10 \quad (5.4)$$

The time necessary to deplete the element i shows an inverse proportionality with the value F_i of the parametric function. This property has indeed been suggested in a previous study [9] and is reconfirmed theoretically in this chapter. Since the depletion of atoms operates sequentially, it is suggested that the time needed to degrade the metallization structure by electromigration as well as thermomigration and stressmigration should be the sum of the different needed time T_i to empty each element. Then, the different values of T_i obtained during the void simulation between each step like shown in figure 5.2 can be added, and provide the time-dependency of the phenomena. With this method it would be then possible to determine the state of the metallization structure during the void growth. In the same time, the electrical resistance change of the metallization structure can be retrieved, and temporally coupled with the calculated time. Before the end of the degradation process, the electrical resistance reaches a critical level, which indicates that the electrical interconnection is at the limit of rupture. This moment is generally qualified to be the TTF (Time-To-Failure). If we consider that the metallization is completely failed when the elements assuring the electrical contact are all deleted, then we can defined the calculated TTF as the sum of all the corresponding depletion time T_i and given by equation (5.5):

$$TTF = \sum_{i=1}^n T_i = \ln(10) \sum_{i=1}^n \frac{1}{F_i} \quad (5.5)$$

This expression shows that the TTF can be expressed as the sum of the inverse value of the divergence value over the degradation path, considering that $N=1$.

The description of the different tasks has been provided in the previous part of this chapter. The different steps composing our approach can then be integrated in an algorithm which gives a better overview of the work needed to be implemented for simulation. The next

part will present the algorithm and also how the different tasks can be implemented with available tools.

5.5 Time-dependency algorithm presentation of void simulation

Before going directly into the time-dependency analysis, some preliminary preparation need to be considered. The failure location area can be previously determined during the static analysis. Since a deletion of important volumetric element could affect the precision of the void formation simulation within the metallization structure, the area where the failure location is determined needs to be remeshed with a fine grid. By this way, it's possible to increase the precision of the calculations and the simulations performing the deletion of a small number of elements and simulate the finite element model in a loop, until the complete degradation is calculated. An overview of the different steps to reach this goal is presented by the algorithmic form given in figure 5.3. The first step corresponds to the remeshing and the preparation phase for the time-dependency analysis. On the other hand, a complete static analysis is needed to be processed again in order to determine the failure location area.

The first steps shown in figure 5.3 have been presented and some operations are necessary after the massflux divergence distribution is obtained. Indeed, the different divergence values are classified after calculation. Then, a set of elements having their divergence values among the highest one are retained. The number of elements to be deleted is randomly chosen. The calculation and the simulation of the void formation as well as the time-dependency evaluation should be better as this number get smaller. Next, the deletion of these elements from the finite element model is performed trough the modification of their material properties, since the complete deletion of elements from an ANSYS finite element model is not permitted [56]. In this case, their electrical resistivity is chosen to be a high value ($\sim 10^{14}\Omega\text{cm}$) like for silicon dioxide and their thermal conductivity is taken to be a small value ($\sim 10^{-12}\text{W/mK}$) for the simulation of air conductivity. By the same way, the mechanical properties have to be changed and the Young modulus has been taken to be a small value of 10Pa. The Poisson ratio as well as the thermal coefficient of expansion have been considered to be the same one as the property of the conductor material. When the simulated development of void is performed, a thermal-electrical analysis is necessary. It gives the opportunity to get some information on the electrical resistance development of the

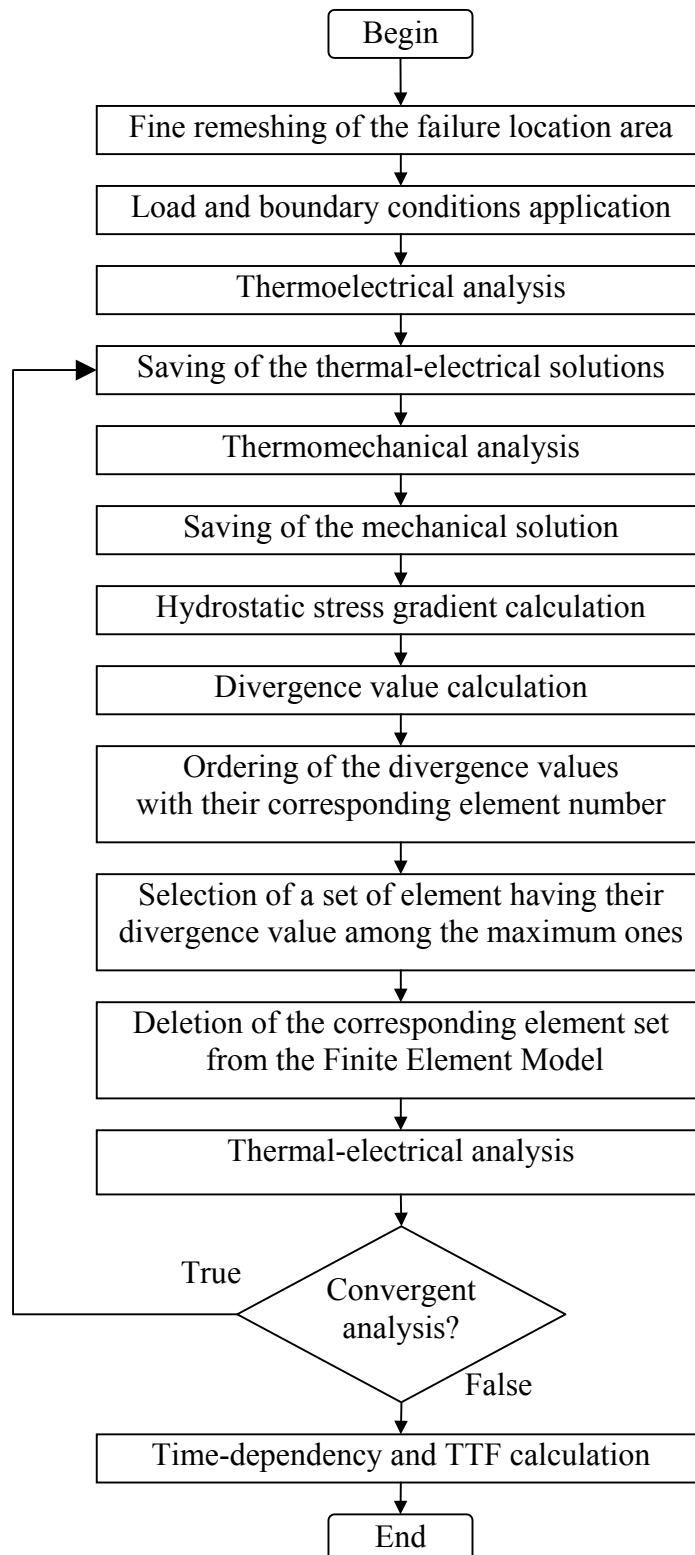


FIGURE 5.3. Overview of the time-dependent void simulation algorithm.

metallization structure, where the voltage maximum value is retrieved [57]. In parallel, it determines if the electrical interconnection formed by the metallic conductor line is still functional. In this case, the void can pursue its growth, and the finite element model continues to be looped by the program. In the contrary, the metal line should have failed when the thermal-electrical analysis does not converge. As a consequence, the electrical interconnection is simulated opened and the sequential process of element deletion is stopped. Out of this, the time-dependency evaluation of the degradation can be determined and the simulation process is terminated. In the program represented by the algorithm in figure 5.3, the divergence calculation as well as the classification and the determination of the elements used for the deletion process is included and programmed within an external Fortran program. The sequential tasks are linked together through the use of a batch file including DOS written commands. The test of the convergent analysis is also carried out by the same way. The time-dependency and the TTF are then calculated by an external Fortran program which consider the equations (5.4) and (5.5). In the following chapter, the calculation and the simulation results will be presented for the both investigated structures. In order to get more information about the influence of the different parameters on the simulation results, a parameter variation study will be carried out. In this study, the variation of the activation energy E_A , the effective charge number Z^* and the specific heat of transport Q^* will be investigated.

5.6 Algorithm implementation on computing systems for simulation

In order to simulate void formation induced degradation over metallization structures, their implementation in available computing systems was necessary. The simulation tool was developed on a Sun Microsystems workstation of type SPARC Station 20, where Unix commands as well as Fortran developed programming code were combined together with the APDL language of the FEM program ANSYS. In order to accelerate the velocity of the calculations and the simulations, the codes been transferred on PC systems. The optimisation of the codes has been performed on a PC computer equipped with an AMD Athlon processor cadenced at 800MHz and with 512MB of work memory (RAM). The Unix simulator code has then been translated into DOS commands within batch files.

6. 3-D time-dependent void simulation formation in metallization structures

In this chapter, the simulation results of the void formation within the meander and the sweat structures are presented. The material properties used in the simulations have been given in chapter 3. The time-dependent simulation is based on the results of the static analysis. The results are taking into account the same boundary conditions exposed for the static analysis. The massflux divergence distribution for these structures have been given in chapter 4. The TTF has been experimentally determined from accelerated ageing tests and for different loads like presented in the first chapter. A comparison between the simulation results and the TTF calculation is provided here in order to qualify the developed algorithm. Finally, the influence of the different physical parameters as well as the variation of different material properties on the calculated TTF is studied. The parametric investigation study the influence of the substrate temperature, the influence of the activation energy E_A , the variation of the effective charge number Z^* and the influence of the specific heat of transport Q^* on the calculated TTF. The influence of the random number of the deleted elements used per simulation step for the void simulation is also investigated.

6.1 Void formation simulation for the meander structure

In order to simulate the void formation within the meander structure, a study of the massflux divergence distribution was necessary. The distribution for an applied current of 200mA was presented in figure 4.14 for the meander structure. The maximum value is found to be located near to the intersection of the long part and the small one of the meander structure. Moreover, the maximum divergence value is determined to be confined at the metallization-oxide interface. This result indicates a start of the depletion process at this location. For the void simulation, a particular amount of elements is chosen to be deleted per step so that the simulation process is performed in this case in more than 6 steps. The start of the void simulation with a set of 60 deleted elements per step is given in figure 6.1. The different parameters like the current density, the temperature gradient and the hydrostatic stress gradient were found particularly strong at this location and explain why the void nucleation is found there. In the next step, the thermoelectrical as well as the thermomechanical analysis are performed again and a new massflux divergence distribution is

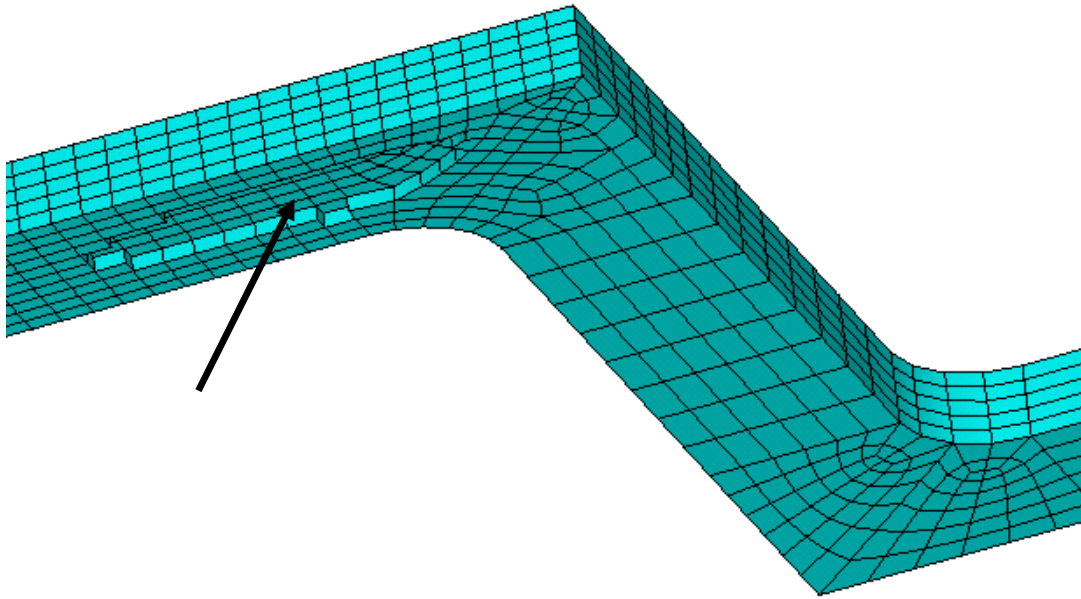


FIGURE 6.1. First step of the void formation simulation at the interface within the meander structure.

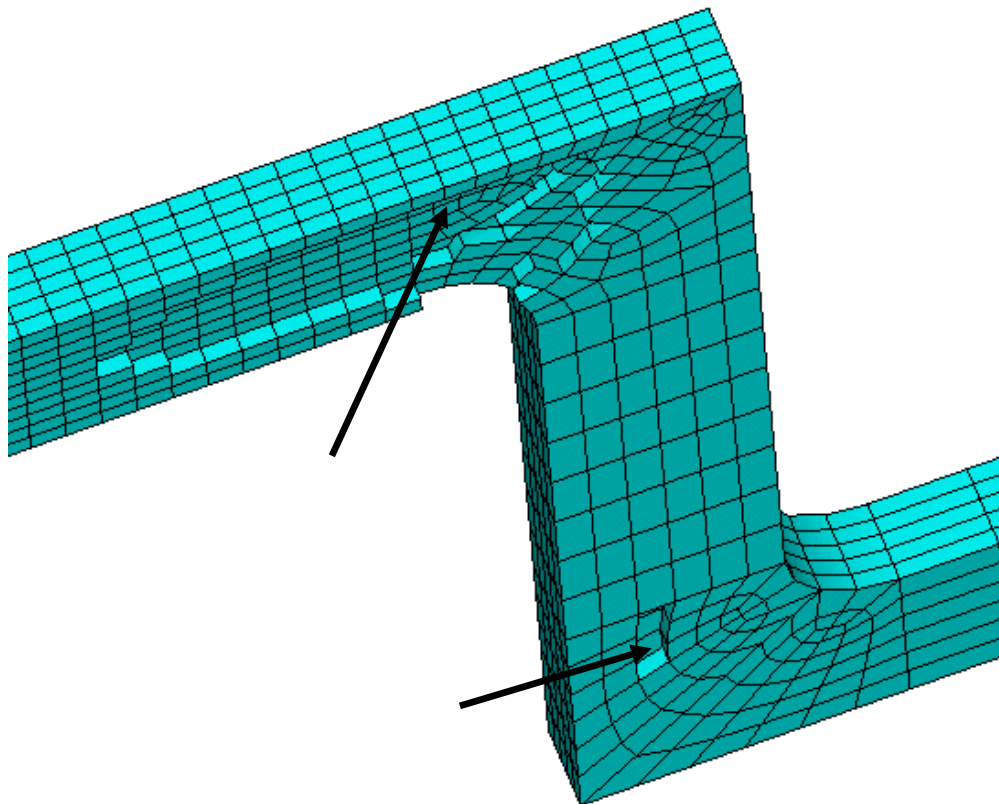


FIGURE 6.2. Void formation simulation overview for the second step.

obtained for the modified structure. Like described for the first step, the elements are deleted where the elements have their divergence values to be among the maximum ones. The void formation simulation for this step is presented in figure 6.2. Two phenomena are remarkable as shown by the picture: the first one shows a deeper evolution of the void through the metallization structure and near to the inner corner, suggesting further amplification of the electromigration phenomena on the degradation. When the matter is removed sequentially as shown previously, the cross-section area of the metallization structure at this location decreases. The decrease of the cross-section induces an increase of the current density in this region which induces a local increase of the temperature due to Joule heating phenomena. The second phenomena corresponds to the formation of an other void at the opposite side of the first one like shown in figure 6.2. This indicates that several voids are able to occur within the metal line when the load is strong enough. Next, the process of degradation simulation continues and the morphology of the void evolution obtained is presented in figure 6.3. The degradation evolution has moved towards the inner corner of the metallization structure where

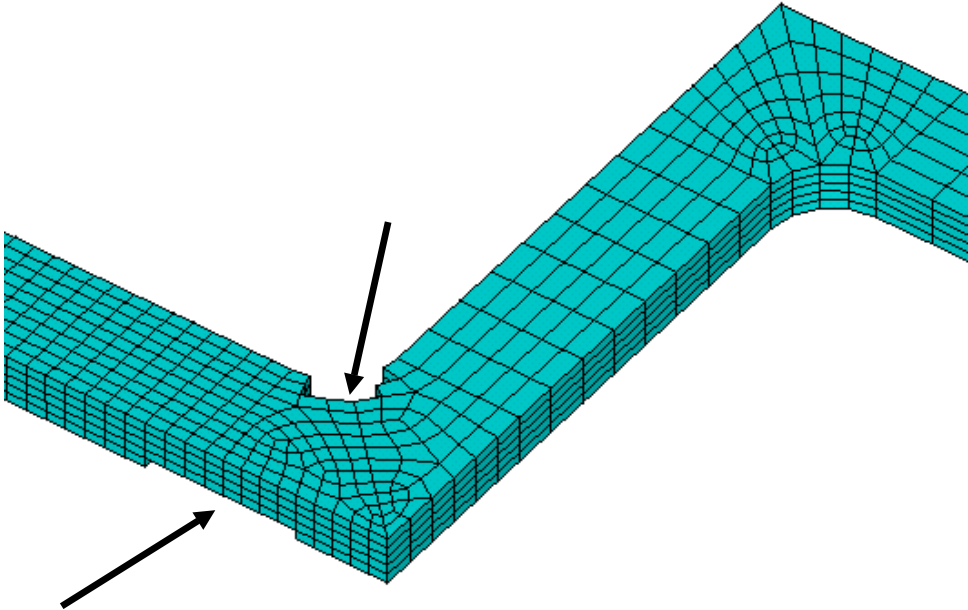


FIGURE 6.3. Void evolution simulation performed in the 3rd step.

elements have been removed again. In addition, the degradation simulation takes place at the interface metal-oxide due to the absence of a passivation layer and confirms previous experimental investigations presented in the literature. At the stage of the void simulation, the

degradation path taken by the void in the direction of the inner corner seems to confirm that the electromigration activity in the matter depletion process at this location is stronger than the stressmigration and the thermomigration. The current density reaches high values at this

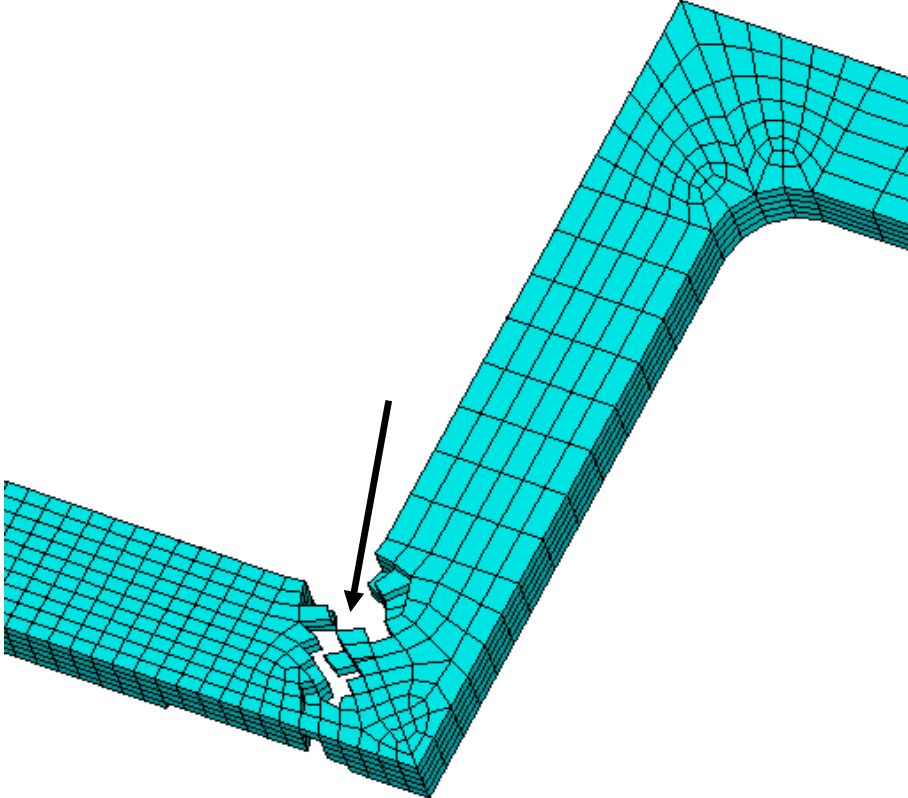


FIGURE 6.4. Void formation simulation performed by the 4th step.

location. Moreover, a non negligible increase in the electrical resistance at this step is also expected. Based on the new geometry taken by the metallization, the 4th step of the void evolution simulation can be performed. In addition, the modification induced in the geometry by the void simulation should have an impact on the massflux divergence contribution due to stressmigration. Indeed, the long part of the metallization as well as the small one tend to expand towards the inner corner of the interconnect due to thermal conditions. This expansion induces compressive stress and also stress gradients at this location. Else, the thermomigration contribution is expected to be relatively low at the stage of the degradation simulation because the temperature elevation would not be critical to induce high temperature gradients at this location. In this case, only two phenomena are suggested to really influence the void evolution, which are the electromigration and the stressmigration. These analysis results will be studied in details and should be confirmed in the determination of the different effects on

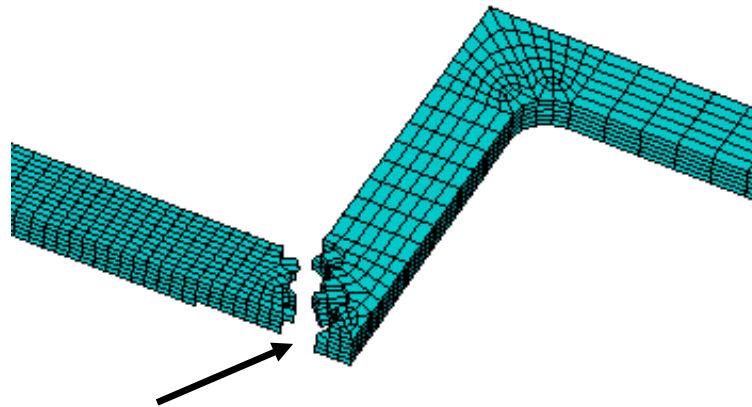


FIGURE 6.5. Completed simulation destruction of the electrical interconnection after 6 steps.

the void growth through the analysis of the different divergence value evolution. The void evolution simulation obtained by the fourth step is shown in figure 6.4. At the stage of the simulation process, the destruction of the electrical interconnection due to a deeper development of the matter depletion process through the metallization structure is shown. Moreover, the picture shows that the cross-section area for current conduction is now really limited and that the interconnection is at the limit of failure. This cross-section area is now able to induce some important increase in the electrical resistance on the metallization structure. The increase of the current density in the small portion of the metal line also creates an increase of the temperature and strong temperature gradient level on the both sides of the location. Consequently, the electromigration contribution could be one of the highest contributions on the last step of degradation. To illustrate this last step of void growth simulation, the simulation of the destruction of the electrical interconnect is given in figure 6.5.

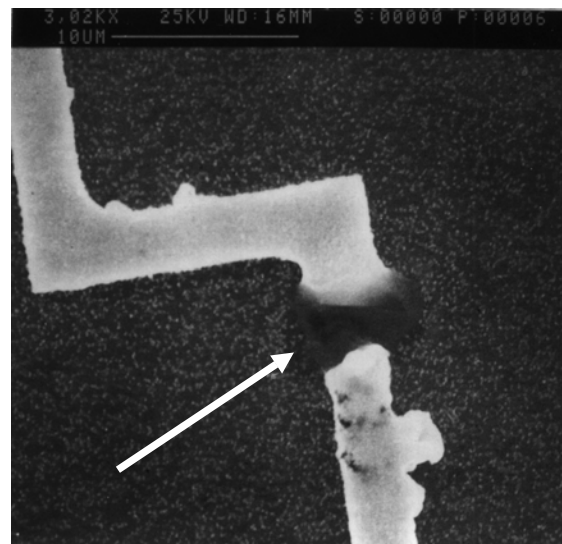


FIGURE 6.6. REM report after the ageing accelerated test of the meander structure.

This picture finally indicates that the void growth obtained by simulation has taken a path where the metallization structure knows some variation in the morphology of the design.

Indeed, the metallization structure forms a right angle at this location and the failure location is determined in this area by simulation and is verified experimentally. Nevertheless, the opposite corner do not suffer from any degradation process. The divergence values have been found to be mostly negative in this area indicating an atomic accumulation and the formation of hillocks. The simulation of the degradation of the metallization structure is found in concordance with the experimental observations and its morphology is comparable with the REM analytic report shown in figure 6.6. The simulation results are also found in good agreement with the work performed by V. Sukharev [59] on the same meander structure.

6.2 Analysis of the different migration mechanisms during the void simulation growth

In order to quantify the different migration effects in the degradation of the metallization structure during the void simulation process, the analysis of the divergence values of the different effects that contribute to void formation is necessary. To do so, the divergence values for the electromigration, the thermomigration as well as for the stressmigration is recorded sequentially at the void formation site and during the void simulation growth. This analysis provides the opportunity to measure the importance of the different migration effects when the development of the void within the metallization structure takes place. The results obtained for the meander structure analysed at 180°C and under an applied current of 200mA is listed bellow.

| STEP NUMBER | DIVTOT | DIVELEC | DIVTH | DIVSH |
|-------------|--------------|--------------|---------------|---------------|
| 1 | 0.447589D+14 | 0.260562D+14 | -0.680349D+13 | 0.255062D+14 |
| 2 | 0.145324D+15 | 0.478415D+14 | -0.891896D+13 | 0.106402D+15 |
| 3 | 0.233946D+15 | 0.240076D+15 | -0.352145D+14 | 0.290840D+14 |
| 4 | 0.121579D+16 | 0.157673D+16 | -0.183208D+15 | -0.177730D+15 |
| 5 | 0.252509D+18 | 0.378549D+18 | -0.229175D+17 | -0.103122D+18 |

TABLE 6.1. Divergence values evolution of the different effects at the failure site for the meander structure [$1/\mu\text{m}^3\text{s}$].

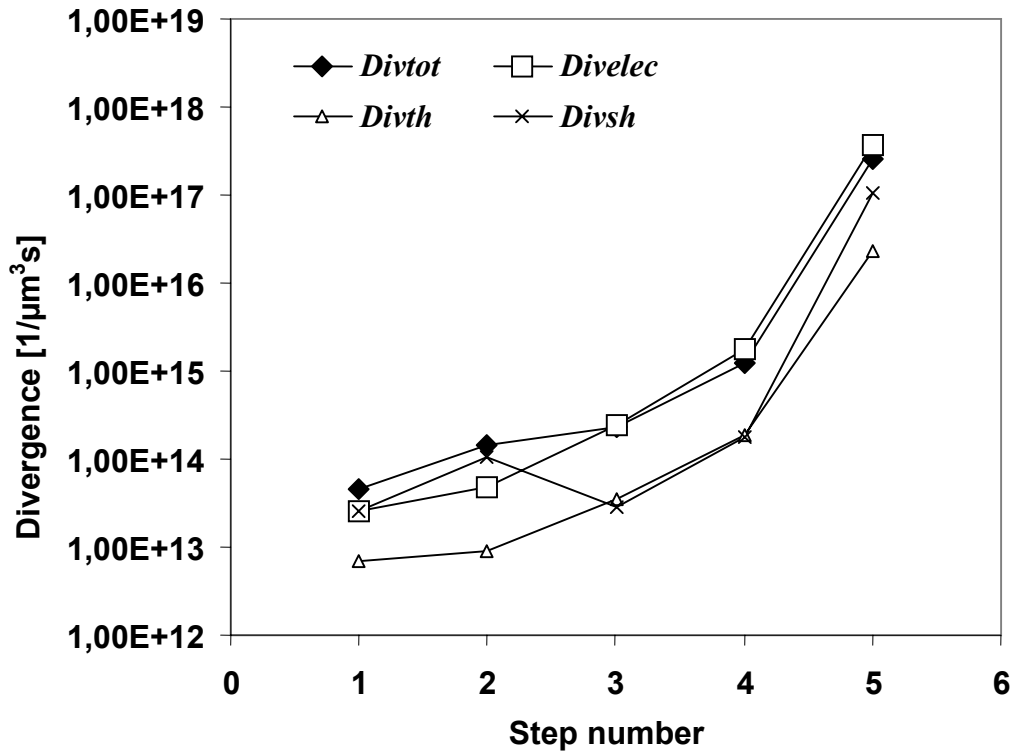


FIGURE 6.7. Different divergences effects at failure location during void growth.

The total divergence value (DIVTOT) represents the sum of the different divergence value of the electromigration, the thermomigration as well as the stressmigration (DIVTOT=DIVELEC+DIVTH+DIVSH). An analysis of these values shows that the value obtained for the thermomigration (DIVTH) is always negative. That means that the thermomigration acts as a backflux and tends to slow down the degradation velocity. The values due to the electromigration and the stressmigration phenomenon are found positive and in the same order when the void simulation begins. Nevertheless, the electromigration effect is found to be the most active phenomena in the last steps of the degradation simulation whereas the stressmigration acts as a backflux (negative value of DIVSH at the 5th step). Finally, an oscillation in the stressmigration is detected with a modification in the geometry due to void formation(3rd step). This oscillation may be due to the relaxation mechanism of mechanical stress due to the void formation itself at the failure location. A better overview of the different effects acting in the degradation process is given in figure 6.7. It confirms the dominance of the stressmigration at the beginning of void formation caused by the load conditions (high current density, high running temperature and low stress-free temperature state), the dominance of the electromigration from step number 3 and the small influence of the thermomigration during the void simulation growth.

6.3 Time-dependence determination of the electrical resistance evolution

The simulation of the void induces a change in the morphology of the metal line. Out of this, a variation in the electrical resistance is expected like determined during the experimental observations. A change in the electrical resistance induces a variation in the electrical potential taken between the extremities of the metallization structure under the effect of the electrical current. Consequently, when the void growth is being simulated, the finite element program ANSYS calculates the electrical voltage distribution and determines the maximum voltage evolution of the metallization structure. The evolution of the maximum electrical voltage for the void growth simulation under 100mA and for 30 deleted elements per step running with an environment temperature of 180°C is shown in figure 6.8. The maximum voltage value increases slowly when the degradation goes on and has a strong variation before the metallization structure fails. This result is found in good agreement with some investigation results found in the literature [60]. The strong variation in the maximum voltage value corresponds to the moment where the electrical resistance of the interconnection surges towards an infinite value and determines the Time-To-Failure (TTF) of the metallization structure. Such variation surges towards an infinite value and determines the

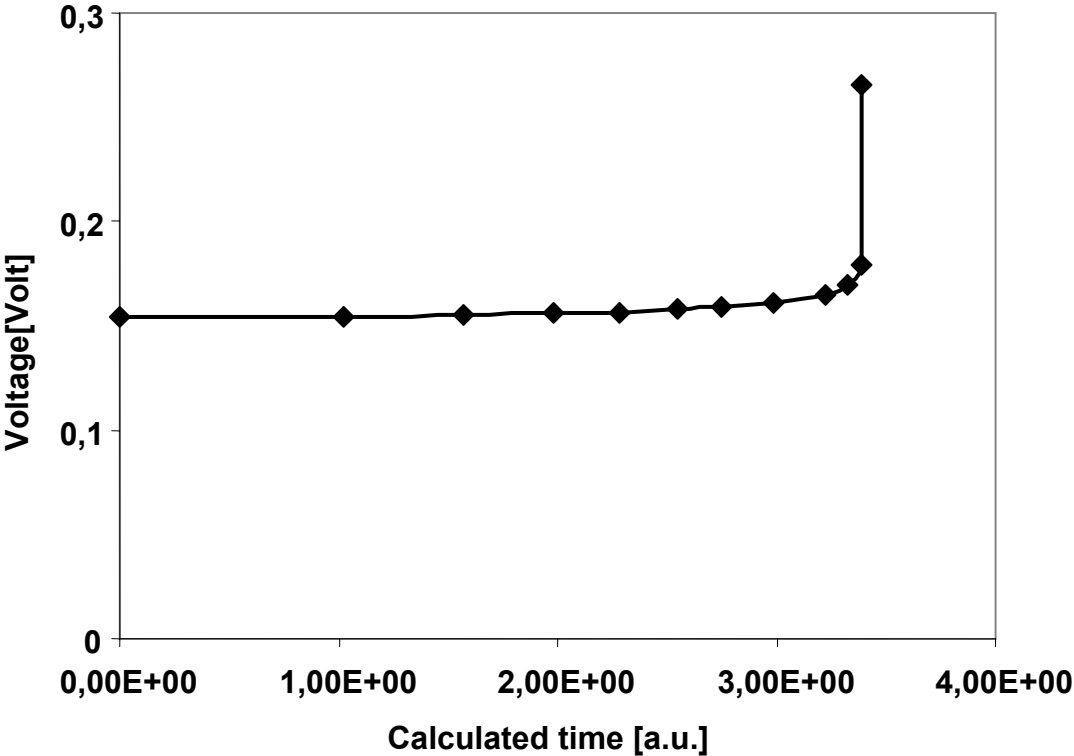


FIGURE 6.8. Voltage evolution simulation during the void growth.

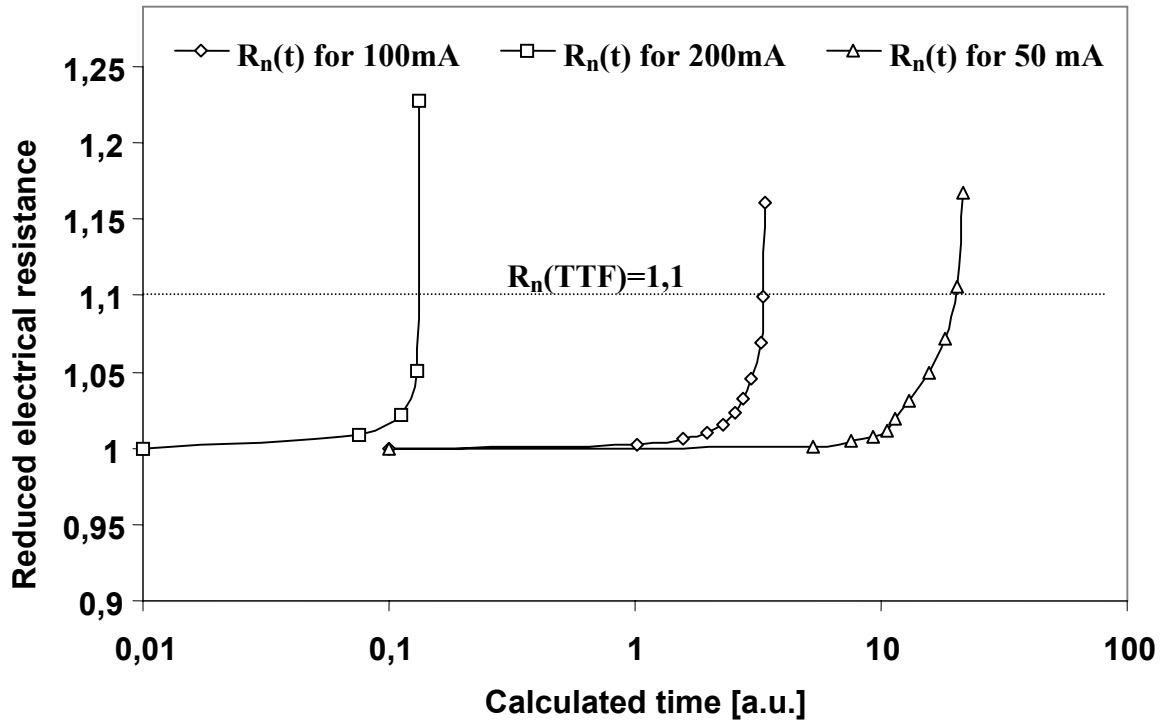


FIGURE 6.9. Reduced resistance simulation evolution under different applied current.

Time-To-Failure (TTF) of the metallization structure. Such variation in the electrical resistance is also attributed to the decrease of the cross-sectional area of the metallization structure at the failure location and to the local increase of temperature at this location [61]. The TTF is determined when the electrical contact is destroyed. Nevertheless, one reliability criteria takes into account the consideration of the RC constant delay for the switching time in logic integrated circuits, where R is the electrical resistance of the conductor line, and C is the entrance capacity of single logic gate. In this case, the functionality of the interconnect is considered lost when electrical resistance R has increased 10% from the initial electrical resistance value measured without applied current [62,63]. The analysis of the electrical resistance development for different applied current have been investigated like presented in figure 6.9. The reduced resistance evolution $R_n(t)=R(t)/R_b$ of the interconnect is displayed and the time-dependency have been determined for these different loads. R_b is the electrical resistance of the metallization structure at the beginning of the experiment (or the simulation). The different value of the TTF defined by $R_n(TTF)=1,1$ can be determined like shown in the figure. The corresponding time have been expressed in arbitrary due to the gap found between calculation and measurement results. To explain this, the value of D_0 taken for the time-dependency calculation corresponds to the value for pure aluminum and the material used for

the experimental observation and in this analysis is an aluminum material alloyed with 1% of silicon. In addition, the quality of the metal used for the fabrication of metallization structure doesn't reflect those used and found in the literature. The measured value of the aluminum specific electrical resistivity ρ_0 was found to be 50% higher than usual values ($\sim 3,20\Omega\text{cm}$). However, the ANSYS program doesn't provide the possibility to simulate properly the void growth (the quadric element volume deletion represents the macroscopic simulated void growth) and some deviations are also expected in the comparison between the calculated TTF and the experimental results.

6.4 Comparison of the calculated TTF with experimental results

In order to complete partially the study on the meander structure, an analysis has been performed in order to compare the TTF obtained by calculation and the measured MTF (Mean-Time-to-Failure). The investigation is made by applying different level of current loads within the metallization structure, and then by simulating the void growth in each case. During the study, the void growth path and the failure location has been determined to vary

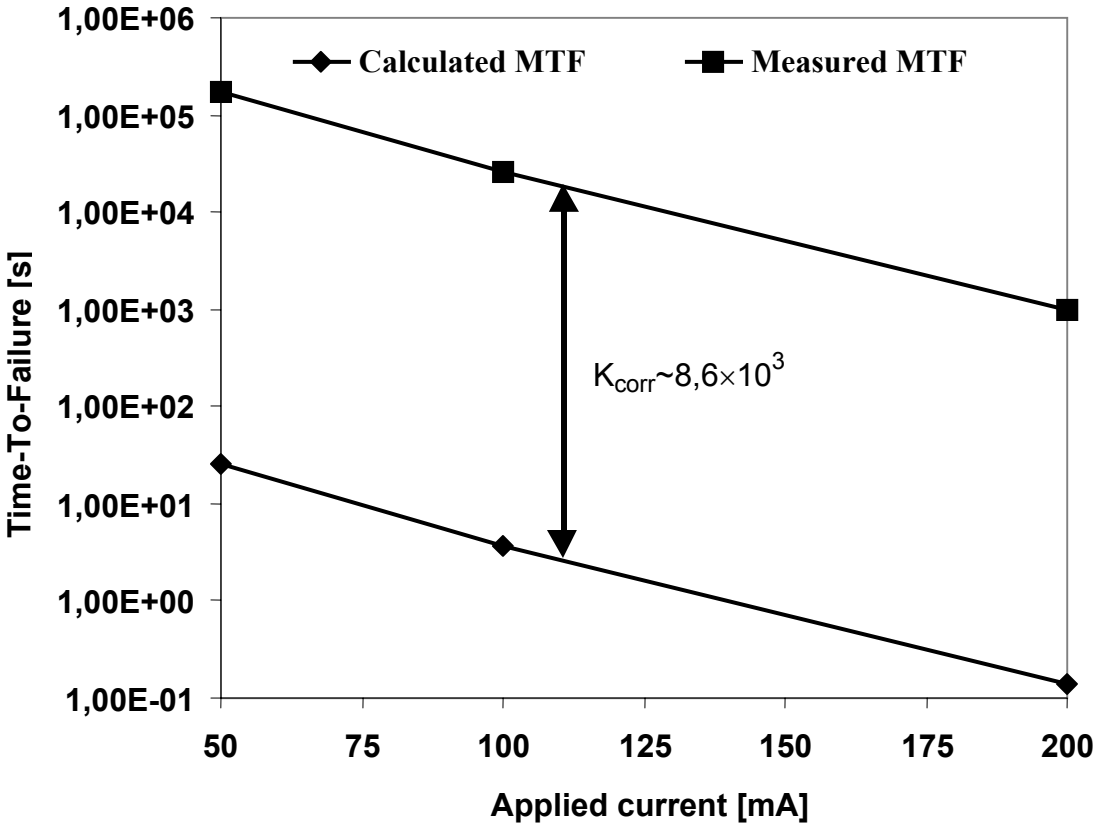


FIGURE 6.10. Comparison of the lifetime values between measurement and simulation results.

under different values of the applied current. The void simulation growth will not be presented here for each load, but the comparison between calculation and experiments is given in figure 6.10. The calculated TTF decrease with the applied current as expected. The analysis shows a perfect proportionality factor K_{corr} between the measured MTF and those obtained by calculation. The existence of a proportionality factor between the calculation and the measurement results may be due to different causes (quality of the metallization, non-proper simulation process, used alloy).

6.5 Variation of the number of deleted elements during void growth simulation

The void growth simulation is performed by deleting a random number of elements having their corresponding divergence values among the higher ones. The effect of this random number on the time-dependency, and particularly on the determination of the TTF calculation has to be determined. The investigation was made with an applied current of

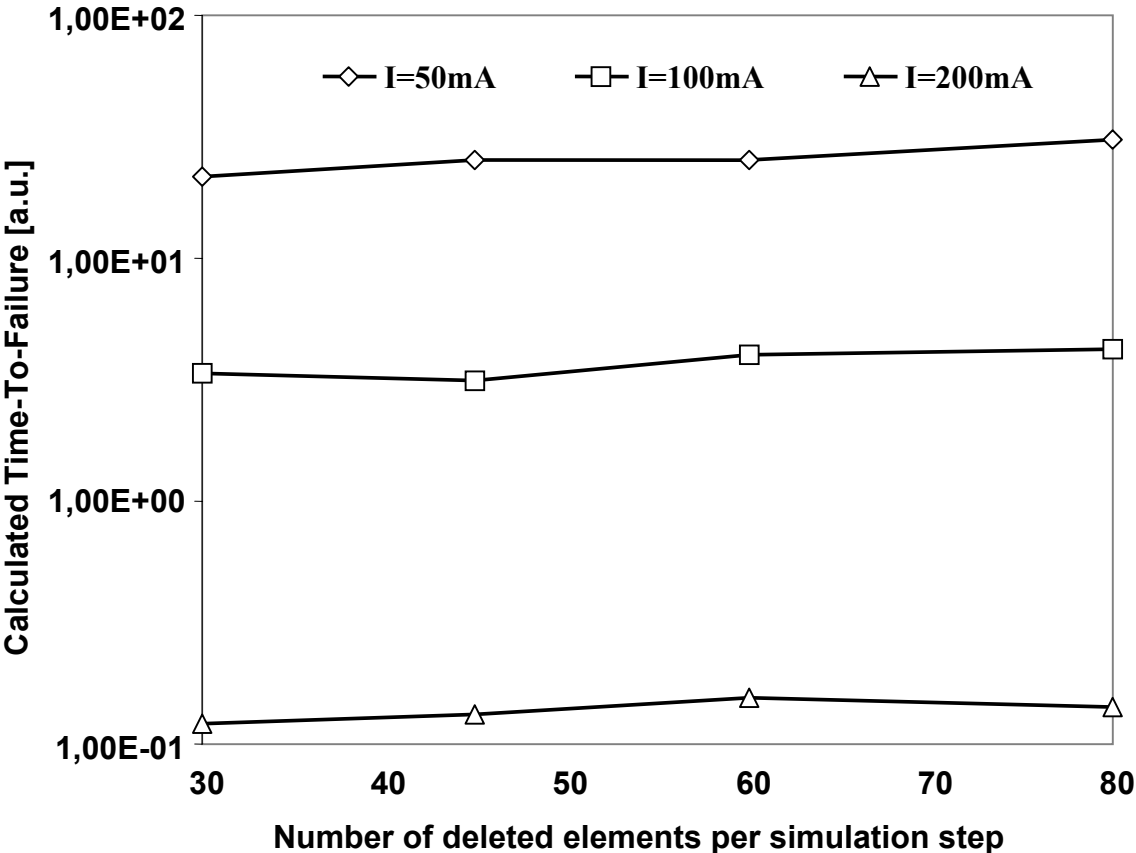


FIGURE 6.11. Per step number of deleted elements variation effects on the calculated TTF.

50mA, 100mA, and 200mA. The number of deleted elements was varied from 30, 45, 60, to 80. The results of this analysis is shown in figure 6.11. The variation of the number of deleted elements per simulation step doesn't affect the value of the TTF determined by calculation. Consequently, the algorithm can be qualified to be stable for any variation in the number of deleted elements per step when they are taken between 30 and 80 deleted elements per step.

6.6 Influence of the physical parameters on the calculated TTF

Any integrated circuit is expected to run under different environment conditions, in particular within a temperature range. The experimental results of the accelerated tests over the meander structure and with the substrate temperature variation are available as presented in chapter 1. In order to increase the qualification process of the developed algorithm, further investigations have been performed. To do so, the effect of the substrate temperature on the TTF is determined by simulation and the corresponding results is compared to the experimental one's. Next, the influence of the range of values determined from the literature for the specific heat of transport Q^* , the effective charge number Z^* and the activation energy E_A on the calculated TTF is presented.

6.6.1 Variation of the substrate temperature

During the experimental procedure, the influence of the substrate temperature variation on the TTF was determined for the meander structure. The investigation of the substrate effect on the TTF by simulation is a complementary evaluation of the developed algorithm for void growth simulation. The void simulation growth is simulated with a current load of 100mA and the substrate temperature is varied from 130, 150 to 180°C. The results obtained by simulation and calculation is shown in figure 6.12. The TTF has been found to decrease when the substrate temperature is increasing. The calculated TTF reproduces exactly the results obtained experimentally and confirms the trend taken by the TTF with the temperature. The simulation results obtained here from the use of the developed algorithm seems to attest that the calculation of the TTF can be performed by computer analysis, since the correction factor K_{corr} is found to be almost the same in the cases of the applied current variation and the substrate temperature variation. The trend found in the TTF with the substrate temperature is found in concordance with the experimental results. The results

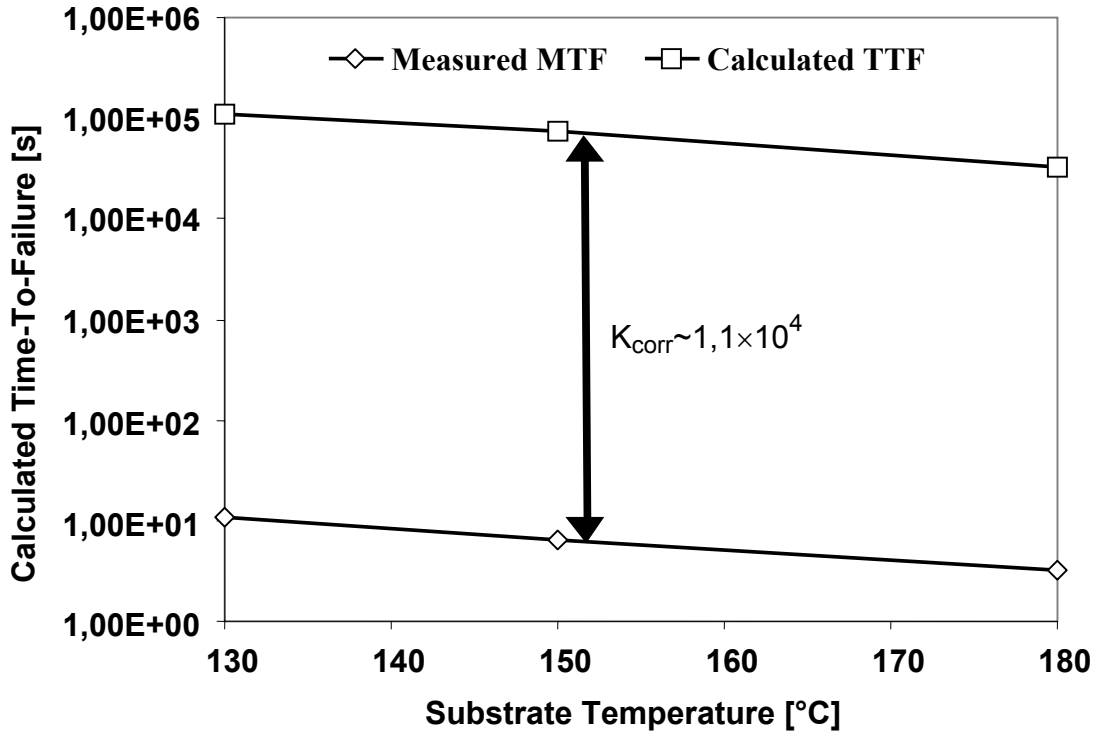


FIGURE 6.12. Effet of the substrate temperature on the calculated TTF for the meander structure.

obtained for this investigation shows again how valuable the developed algorithm is and qualifies the developed algorithm as additional way of reliability investigation.

6.6.2 Influence of Q^* , Z^* and E_A on the calculated TTF

The physical parameters like the specific heat of transport Q^* , the effective charge number of ions Z^* have been extracted from the literature. The activation energy E_A for the meander structure has been determined experimentally. A study of the calculated TTF with the variation of the activation energy values found in the literature is necessary to study their influence on the simulation results. The same investigation should be applied for the specific heat of transport Q^* and the effective charge number Z^* . In this part, their variation based on the values provided in the literature and presented in the chapter 3 will be considered. The experimental tests have been performed under high current density and high temperature environment. The presence of high induced thermomechanical stress has been determined by simulation. These aspects justify the consideration of the different effects and the study of their influence on the degradation time. The investigation was performed with the meander structure for an applied current of 100mA and with 45 deleted elements per void simulation

step. Figure 6.13 gives the effect of the specific heat of transport variation on the simulated TTF. The displayed results shows that the calculated TTF decreases when the value of the specific heat of transport increases.

The TTF determination takes into account the thermomigration influence. The failure location was found to be the same with the variation of Q^* . The increase of the thermomigration through a value of Q^* from $-0,3\text{eV}$ to $0,5\text{eV}$ is found to deteriorate the reliability of the metallization structure caused by the decrease of the calculated TTF.

The influence of the effective charge number Z^* on the TTF variation has

also been determined, and is exposed in figure 6.14. The failure location was found to remain stable when the value of Z^* was varied. The results extracted from this analysis indicates that the calculated TTF decreases when the effect of the electromigration is increasing. Finally, the influence of the activation energy deviation on the TTF determination has been studied. Different value of the activation energy have been varied from $0,3\text{eV}$ to $1,4\text{eV}$ and applied to

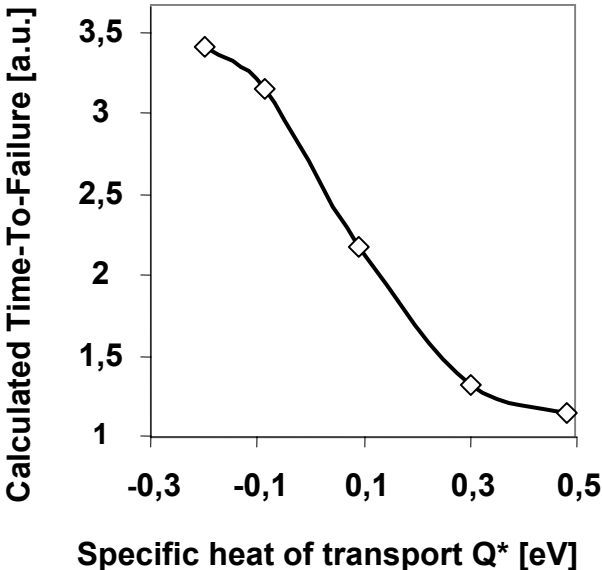


FIGURE 6.13. Effect of Q^* on the calculated TTF.

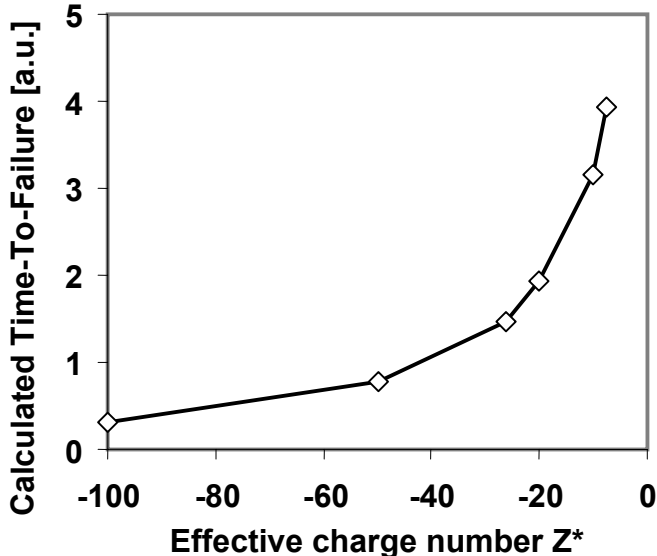


FIGURE 6.14. Influence of Z^* variation on the calculated TTF.

the meander structure to study their influence on the TTF calculation. The variation of the calculated TTF due to the deviation in the activation energy value is given in figure 6.15. The simulated TTF is determined to increase exponentially with the activation energy. The study demonstrates the strong sensibility of the calculated TTF with the variation in the activation energy. Consequently, the determination of this parameter remains one of the

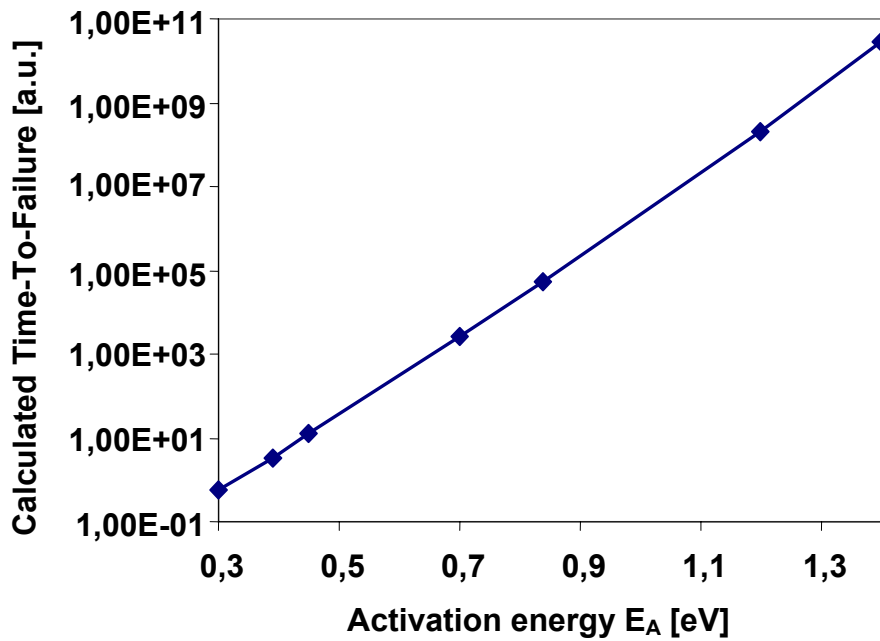


FIGURE 6.15. Influence of the activation energy value on the calculated TTF.

important steps during the characterization work, and suggests that the measurement errors have to be limited as better as possible. In conclusion, the variation in the activation energy affects the calculated TTF stronger than the variation of the effective charge number Z^* or the specific heat of transport Q^* . It can be concluded that the activation energy value considered for simulation can have an important impact on the differences found between the measured TTF and those determined by calculation.

6.7 Time-dependent investigations on the SWEAT structure

To verify the validity of the developed algorithm, a second metallization structure has been investigated by simulation. The geometry of the structure has been presented in the first chapter. The structure is specifically used for material reliability evaluation for electromigration accelerated ageing tests. The conditions of the test were different than those used for the investigation of the meander structure and should permit to avoid strong residual mechanical stress. The SWEAT structure was tested at room temperature and for current densities above $10\text{MA}/\text{cm}^2$.

6.7.1 Void formation simulation for the SWEAT structure

The following simulation results have been obtained for an analysis of the SWEAT structure with current density of $14,8\text{MA}/\text{cm}^2$ within the metal line. The beginning of the void formation simulation is shown in figure 6.16. The void simulation starts in this case at the interface metal-substrate like found for the meander structure. The failure seems to occur within the metallization structure and not far away from the large part of the structure. Due to the small amount of elements present at the failure location, only 10 elements are deleted per void simulation step to complete the void simulation within the metallization structure with 6

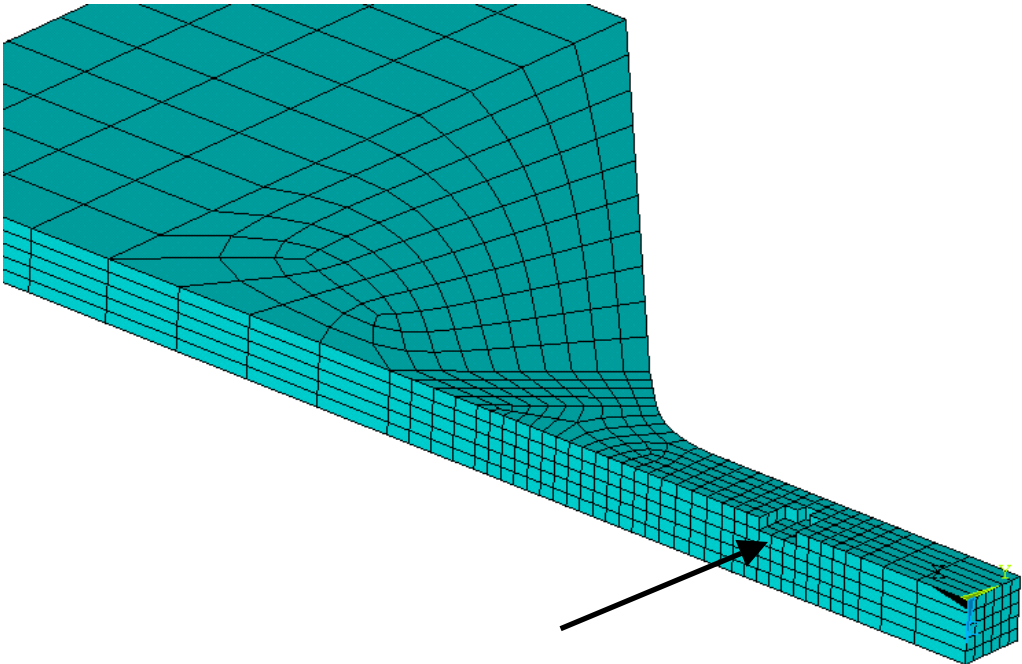


FIGURE 6.16. View of the void simulation start within the SWEAT structure at the interface.

steps. The contribution of the electromigration is determined to be the most important one since the massflux divergence value for electromigration at this location is determined to be the highest one like shown on table 6.1.

| DIVTOT [$1/\mu\text{m}^3\text{s}$] | DIVJA [$1/\mu\text{m}^3\text{s}$] | DIVTH [$1/\mu\text{m}^3\text{s}$] | DIVSH [$1/\mu\text{m}^3\text{s}$] |
|--------------------------------------|-------------------------------------|-------------------------------------|-------------------------------------|
| $0,3153262 \times 10^{11}$ | $0,290130 \times 10^{11}$ | $0,503338 \times 10^9$ | $0,201624 \times 10^{10}$ |

TABLE 6.1. Divergences values of the different effects at the start of the void simulation.

An analysis of the divergence values at the failure location demonstrates that 10% of the degradation is due to stressmigration whereas the thermomigration influence remains weak. Then, the void growth simulation continues like presented in figure 6.17, where the metallization structure continues to be degraded. Important values of current density and temperature gradient have also been observed at this location during the static analysis. Figure 6.18 represents the complete destruction simulation of the SWEAT metallization structure. At this

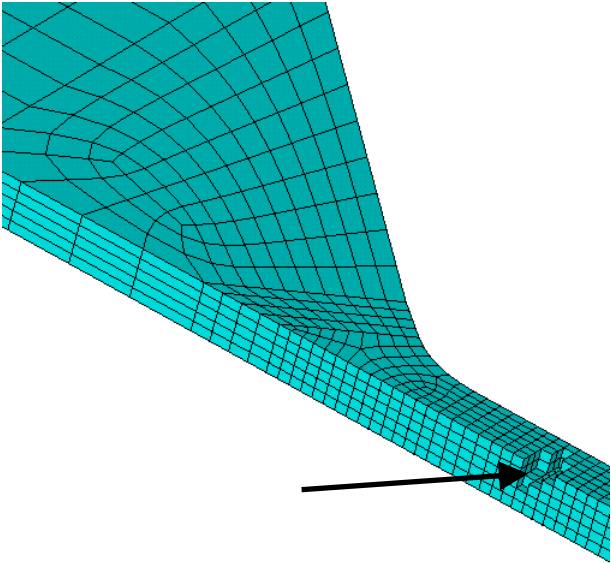


FIGURE 6.17. Void growth within the SWEAT structure.

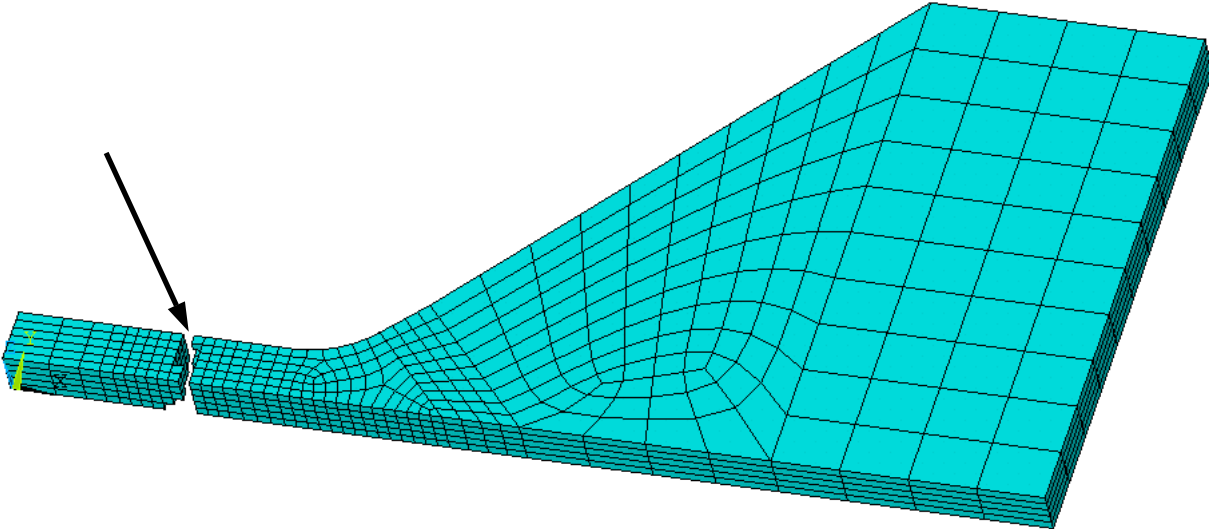


FIGURE 6.18. Completed void simulation within the structure and destruction of the electrical contact interconnect.

stage of simulation, the electrical contact destroyed. The result obtained by simulation for the SWEAT structure is comparable to the degradation stage as shown by the REM report provided by the figure 6.19. The results obtained by simulation are found in good agreement with the experimental results and observations.

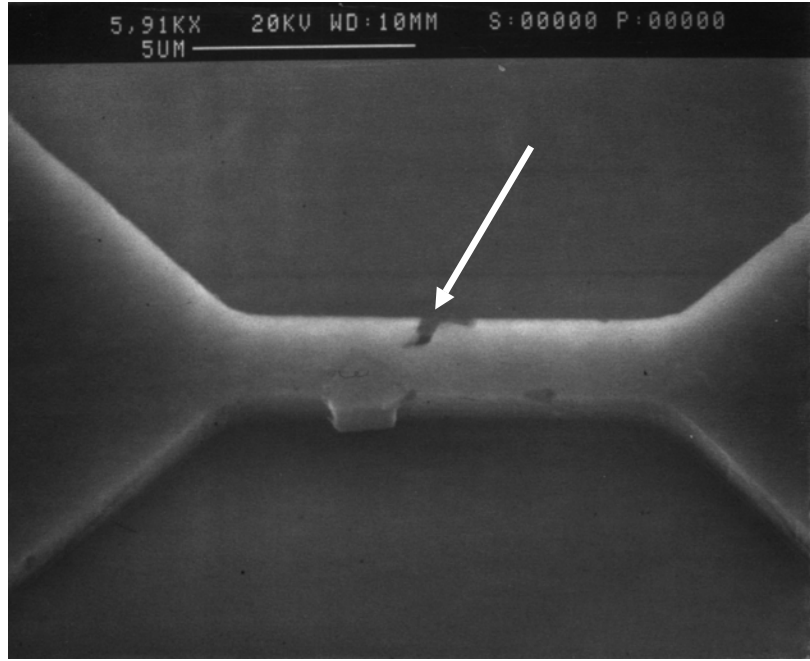


FIGURE 6.19. Void development within the SWEAT structure under accelerated ageing test.

6.7.2 Analysis of the different migration mechanisms during the void growth simulation

Like studied for the meander structure, the analysis of the divergence values of the different effects that contribute to void formation in the SWEAT structure is performed. The divergence values for the electromigration, the thermomigration as well as for the stressmigration are recorded from the void formation site and during the void simulation growth. The results obtained for the SWEAT structure analysed at room temperature (30°C) and under 17,6MA/cm² is given by the listing below.

| STEP NUMBER | DIVTOT | DIVELEC | DIVTH | DIVSH |
|-------------|--------------|--------------|--------------|---------------|
| 1 | 0.716305D+12 | 0.636068D+12 | 0.128380D+11 | 0.673987D+11 |
| 2 | 0.178923D+13 | 0.139090D+13 | 0.394976D+11 | 0.358834D+12 |
| 3 | 0.468345D+13 | 0.394182D+13 | 0.113892D+12 | 0.627739D+12 |
| 4 | 0.119463D+14 | 0.111735D+14 | 0.255202D+12 | 0.517625D+12 |
| 5 | 0.107162D+15 | 0.968770D+14 | 0.307287D+13 | 0.721185D+13 |
| 6 | 0.233152D+17 | 0.229388D+17 | 0.122424D+13 | -0.562570D+15 |

TABLE 6.2. Divergence values evolution of the different effects at the failure site for the SWEAT structure [1/μm³s].

An analysis of these values shows that the value obtained for the thermomigration (DIVTH) is always negligible compared to the values obtained for the electromigration and the stressmigration. Moreover, the electromigration mechanism is determined to be the major degradation mechanism as presented by the values. All the divergence values are found positive at the failure location during the void growth simulation. That means that all the mechanisms participate to

the degradation of the SWEAT structure. A better overview of the different effects acting in the degradation process is given in figure 6.20. It confirms the dominance of the electromigration at the beginning and during the simulation of void formation. Indeed, the structure was investigated at room temperature, and considered relaxed and stress-free at this temperature. The effect of

the induced thermomechanical stress on the degradation of the structure in this case seems to have less influence than in the case of the meander structure. The evolution of the thermomigration and the stressmigration knows an inflexion point at the fourth step like shown in figure 6.20. This may be caused by the modification of the metallization structure geometry when the void growth simulation goes on. From this analysis, it can be concluded that the impact of the temperature on unpassivated metallization structures running under high current densities is the major factor of degradation through the induced stressmigration mechanism. Nevertheless, the electromigration is the predominant mechanism for unpassivated metallization structures running under high current densities and at room temperature.

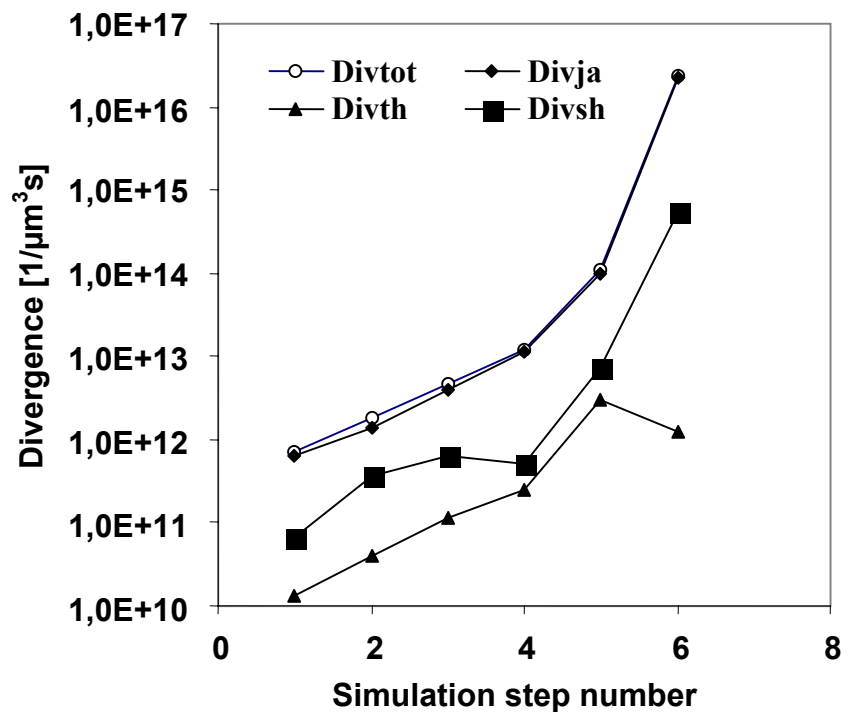


FIGURE 6.20. Degradation mechanisms during the void growth simulation through their divergence values.

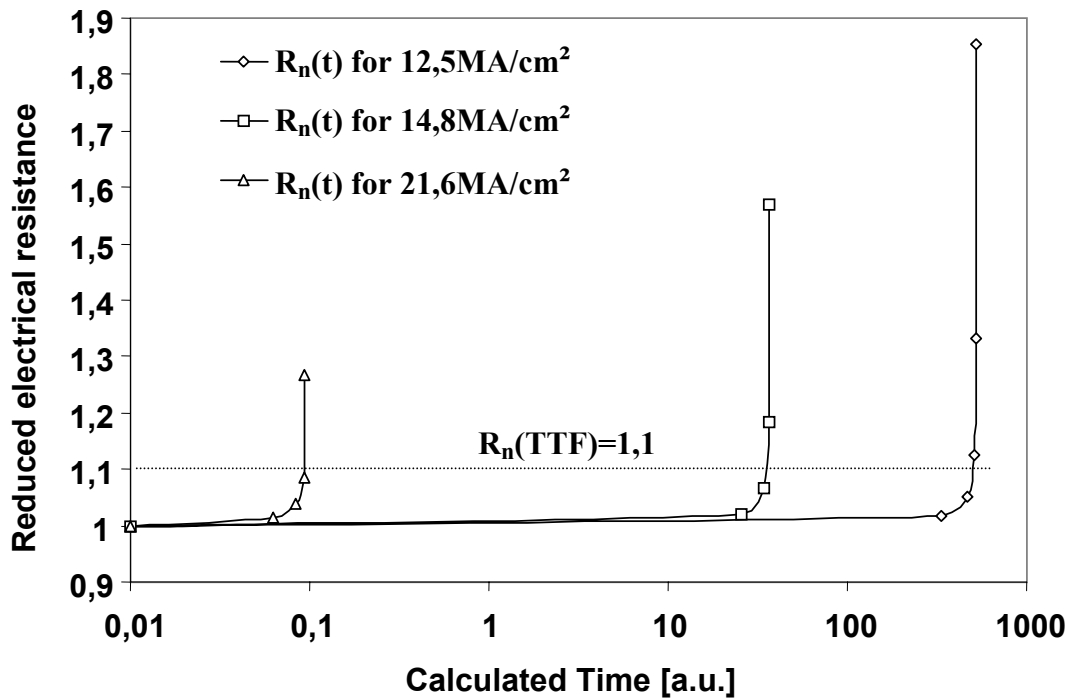


FIGURE 6.21. Reduced electrical resistance value evolution under different current densities for the SWEAT structure.

6.7.3 Electrical characteristic under different load

As for the meander structure, the electrical resistance evolution can be obtained with the time-dependency determination of the void evolution. The electrical resistance evolution can be deduced with the start resistance value before void formation simulation. The evolution of this characteristic $R_n(t)$ for three different current densities given on figure 6.21 and the slope is found to be typical. The electrical resistance is quasi-stable at the beginning of the experiment. Nevertheless, it increases in a great proportion before the moment of failure. The electrical characteristic also confirms that the Time-To-failure value decreases when the level of load increases. The strong variation in the electrical resistance defines the time where the function of the metallization structure is going to be destroyed.

6.7.4 Comparison of the lifetime calculation with measurement results

Like the meander structure, the lifetime for the SWEAT structure has been calculated as a function of the loads. The investigations have been performed in a range of 10 to 25 MA/cm² at room temperature. At these level of loads, the failure location have been found to be almost the same and situated within the metal line. However, the failure location have been determined to vary a lot for loads less than 10MA/cm². The comparison between the results obtained by simulation and those obtained experimentally is given in figure 6.22. The calculated TTF is determined to decrease with the current load as expected. The correction factor between the measurements from experimental results and the simulation one's is found to be at a value about 4×10^2 . The results are found in good agreement with those obtained experimentally.

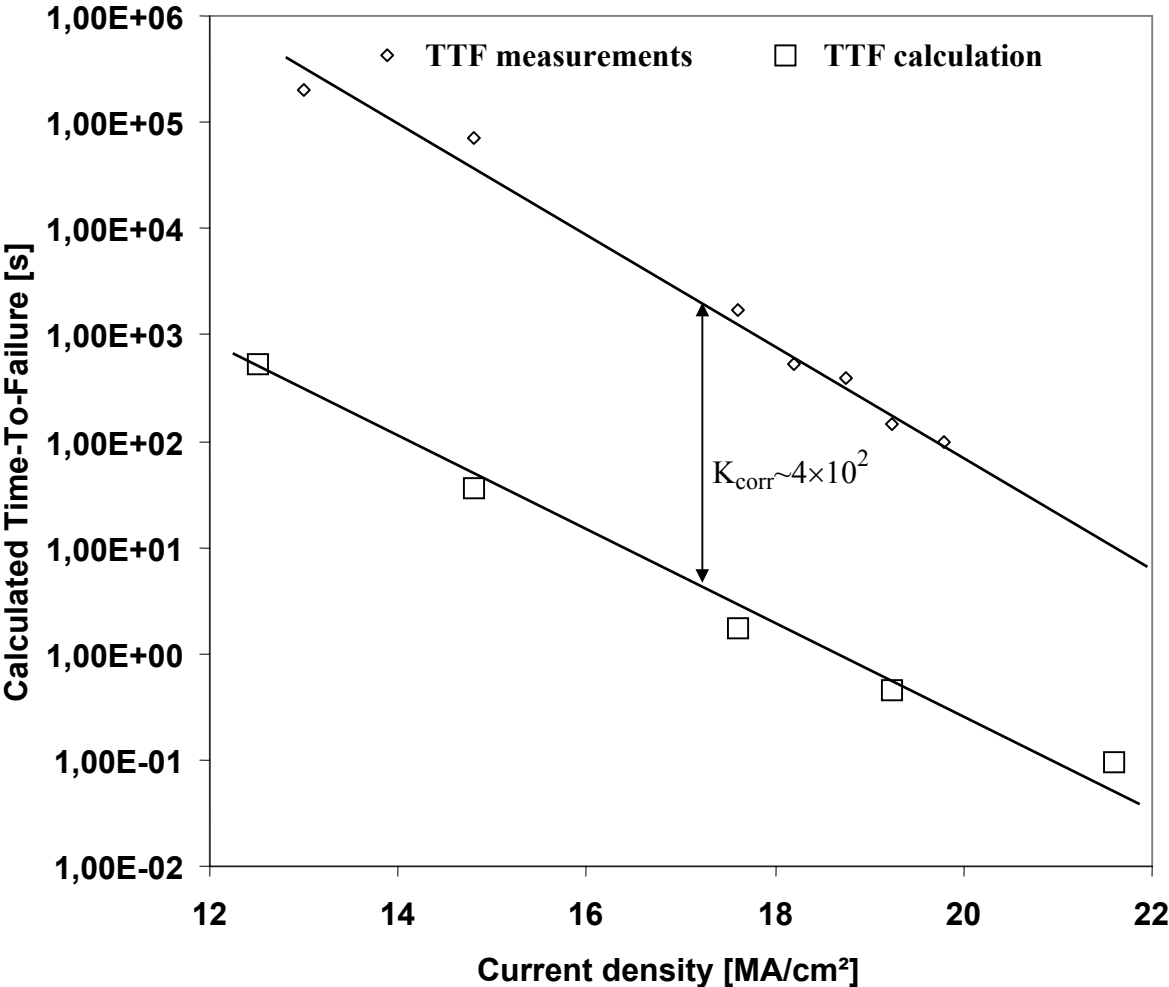


FIGURE 6.22. Time-To-Failure comparison between measurements and calculations.

6.8 Discussion of the simulation results

The correction factor K_{corr} determined in the case of the meander structure as well as the case of the SWEAT structure investigations lead to a different value although the simulation results are found in good agreement with the experimental observations. The difference found between measurements and simulations can have several reasons. One of them may be due to the influence of the alloying element type and the corresponding rate which was aluminum alloyed with 1% silicon in our case. The influence of the alloying element rate of silicon in aluminum on the TTF has been experimentally investigated [64], showing an increase of the lifetime value when the silicon rate in the aluminum matrix increases. In addition, the self-diffusion coefficient D_0 may be smaller in reality than the value used in our simulations which was considered as pure aluminum. The second reason could be the quality influence of the material used for the fabrication of the structures on the substrates. For example, the influence of the fabrication process parameters on the lifetime of metallization structures have been experimentally demonstrated [32,42]. In addition the difference may be due to the value of the activation energy considered for simulation like demonstrated previously. Finally, the simple method used to simulate the void has provided very good results although the method is not perfect, in particular the "deletion" process of volumetric material, which let some discontinuities in the morphological geometry of the simulated void. A research on the coupling combination between massflux divergence values, displaced volume material and a certain flexibility in the volumetric mesh variation should provide a more reliable tool and also more precise time-depending results.

7. Integration of the simulation results in the reliability modelling

One of the difficult issue and research in the domain of systems reliability study concern their lifetime prediction under operating conditions. A reliability test evaluation under operating conditions is generally a time-consuming process. One method usually used consists in the accelerated test of a set of systems (more than 1000 identical items) under high load conditions. The lifetime value is then recorded for each item failed, and different parameters of a degradation law are then extracted. The degradation law generally take into account the load conditions, the boundary conditions as well as some intrinsic parameters specific to the tested system. These parameters are then used in the degradation law in order to obtain the lifetime value if the system was running under operating conditions. In the case of failures due to matter migration within metallization structures, some controversies exist and the theory associated to this mode of failure need to be investigated. In this chapter, the degradation law that usually model the lifetime of VLSI metallisation structures is first presented. Then, the results of the characterisation work done and presented in the third chapter are used in the equation giving the massflux divergence value. Finally, the results will be presented and discussed compared to measurement results and to some parameters extracted from the degradation law.

7.1 Matter migration induced failure degradation law for electromigration

A metallization structure working under high current density can be degraded following an exponential law discovered by J.R. Black [65]. The degradation law is given by the equation provided below:

$$MTF = A \cdot J^{-n} \exp\left(\frac{E_A}{k_B T}\right) \quad (7.1)$$

where MTF is the Mean Time-to-Failure, J is the global current density within the metallization structure, E_A the activation energy of the degradation process, k_B is the Boltzmann constant and T is the working temperature. A is a geometrical factor of the tested structure and n is a current density exponent.

7.2 Integration of the characterisation results in the reliability modelling

At each point location within the metallization structure, we are in the presence of a temperature T , a temperature gradient $gradT$, a current density \vec{j} and a hydrostatic stress

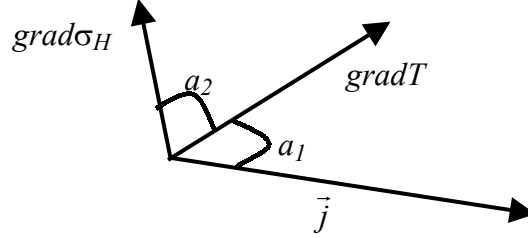


FIGURE 7.1. Spatial configuration of local parameters.

gradient $grad\sigma_H$. The spatial configuration of these parameters can be represented like shown on figure 7.1, where a_1 is the angle formed between the local current density vector and the local temperature gradient, and a_2 the one formed by the hydrostatic stress gradient and the temperature gradient vectors. In addition, we consider that the local current density within the metallization structure is a fraction of the global current density J . In this case, equation (7.2) can be written:

$$|\vec{j}| = mJ \quad (7.2)$$

where m is a parameter function as the location of the current density vector origin. In the same time, a transformation of equations (2.1), (2.2) and (2.8) can result in the following ones:

$$\vec{J}_A = FJA \cdot \vec{j} \quad (7.3)$$

$$\vec{J}_{th} = FTH \cdot gradT \quad (7.4)$$

$$\vec{J}_S = FJS \cdot grad\sigma_H \quad (7.5)$$

where FJA , FTH and FJS are parametric functions respectively from the massflux of electromigration, the massflux of thermomigration and the massflux of stressmigration. With these results, we consider that the metallization structure is free of mechanical stress and that the temperature distribution is homogeneous at room temperature. In this case, the structure presents no temperature gradients as well as no residual stress without any current applied. If these hypothesis are taken into account, then the use of equations (7.2), (7.3), (7.4) and (7.5)

in the equation that models the total massflux divergence value (2.22) described in chapter 2 can be written as:

$$\begin{aligned}
div(\vec{J}_{Tot}) &= \left(\frac{E_A}{k_B T^2} - \frac{1}{T} + \alpha \frac{\rho_0}{\rho} \right) \cdot FJA \cdot m \gamma J^3 \cos(a_1) \\
&+ \left(\frac{E_A}{k_B T^2} - \frac{3}{T} + \alpha \frac{\rho_0}{\rho} \right) \cdot FTH \cdot \gamma^2 J^4 + \frac{NQ^* D_0}{k_B T^2} e^{-\frac{E_A}{k_B T}} \frac{m^2 J^2 \rho^2 e^2}{3k_B^2 T} \\
&+ \left(\frac{E_A}{k_B T^2} - \frac{1}{T} \right) \cdot FJS \cdot \varepsilon \gamma J^4 \cos(a_2) - \frac{2N\Omega D_0 E \alpha_l}{3k_B T(1-\nu)} e^{-\frac{E_A}{k_B T}} \left\{ \frac{m^2 J^2 \rho^2 e^2}{3k_B^2 T} + \left(\frac{1}{T} - \frac{\rho_0 \alpha}{\rho} \right) \cdot \gamma^2 J^4 \right\}
\end{aligned} \tag{7.6}$$

This last equation clearly shows the dependence of the massflux divergence value with J^2 , J^3 and J^4 . The equation can be reformulated like given by the following equation (7.7):

$$div(\vec{J}_{tot}) = J^2 [FDIVTH2 + FDIVS2 + J \cdot FDIVJA + J^2 (FDIVTH1 + FDIVS1)] \tag{7.7}$$

$FDIVTH2$, $FDIVS2$, $FDIVTH1$ and $FDIVS1$ are parametric functions of the different values of the massflux divergences.

Equation (7.7) exposes a dependence on J^2 of the massflux divergence value in the case that $(FDIVTH2+FDIVS2) \gg (J \cdot FDIVJA + J^2(FDIVTH1+FDIVS1))$. The exponent n in the Black equation is then equalled to 2, and verify some experimental results found in the literature.

Else, if $J \cdot FDIVJA \gg (FDIVTH2+FDIVS2+J^2(FDIVTH1+FDIVS1))$, then the exponent should be equalled to 3 and also agree with literature references.

Finally, if $(FDIVTH2+FDIVS2+J \cdot FDIVJA) \ll J^2(FDIVTH1+FDIVS1)$ is verified, the exponent take a value of 4.

A study from experimental results for electromigration test has been performed and reported in the literature like shown in figure 7.2. In this figure, the Mean Time-To-Failure (MTTF) has been measured as a function of the global current density J within the metallization structure. Different values of the current exponent have been extracted from these measurements. Some values going from 1 to 2 have been found and agree with the theoretical result case where a value of $n=2$ has been extracted. For current density values above 0,8MA/cm², the figure suggests an exponent value larger than 2, and these results are in

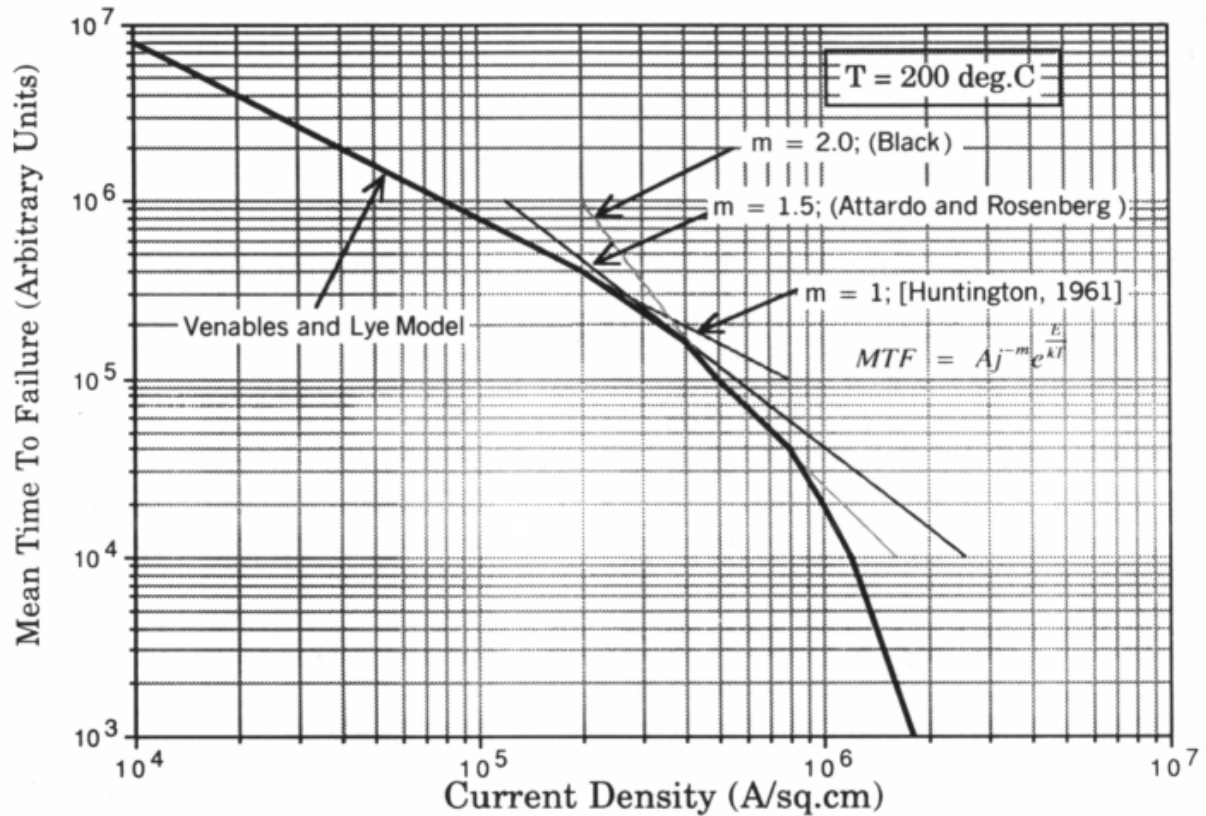


FIGURE 7.2 Typical TTF evolution with the applied current density.

concordance with the theoretical equation (7.7). A good correlation is found between the famous empirical Black equation and the theory used within this work.

For current densities above this value, a study by simulation for each tested structure should be carried out in order to determine the dominant effect in the degradation of metallization structure. The presence of a strong temperature gradient and/or some mechanical stress around a metallization structure when no current is applied can strongly affect the value of the current density exponent determined experimentally, and a study by simulation in each case should provide the opportunity to verify these influences. The influences can be found in the effects of electromigration, thermomigration, and stressmigration or a non negligible percentage of each of them in the degradation process of metallization structures like shown theoretically in this chapter.

Conclusion

In this work, the reliability problem related to the matter migration induced void formation has been exposed. The aim of this work has focused on the degradation mechanisms due to void formation caused by electromigration, thermomigration and stressmigration in unpassivated metallization structures. The time-dependency of void formation in metallization structures has been analysed. Two simplified structures have been experimentally investigated under different test conditions. The time-dependency results have been recorded and visually analysed for interpretation. In the same time, the lifetimes of the structures running under high level of loads has been determined. The deduction of some hypothesis from the experimental observations has been suggested and implemented in an algorithm to reproduce the void formation by 3-D simulation. A routine given the opportunity to calculate the time-dependency of the phenomena as well as the Time-To-Failure have been programmed. The program has been tested successfully with two metallization structures investigated experimentally.

In the first chapter, the reliability test procedure dedicated to the performance evaluation of metallization structures under accelerated ageing test conditions was presented. Then, the geometric description of the tested structures and the different materials used are provided. Next, the experimental observations of void formation in the meander structure has been described. The lifetime values for different applied current densities as well as for different substrate temperatures have been summarised and presented for the meander structure. The Time-To-Failure for different applied current densities have been given for the SWEAT structure investigated at room temperature. Afterwards, the different degradation mechanisms during the void formation were presented. The presentation of the experimental results were necessary in order to compare them to the simulation results.

In the second part, the theoretical background of the different diffusion mechanisms that appear during the void growth degradation process was presented. The physical modelling of the massflux induced by the presence of a local current density has been given. In addition, the mathematical form of the massflux caused by the presence of temperature gradient was exposed. Thus, the influence of the thermomechanical stress induced by Joule self-heating on ions diffusion was delivered. The continuity equation representing the time-dependency of the phenomena has been also provided, and the relationship between the

variation of the atomic concentration and the divergence in the massflux was presented. In addition, the massflux divergence values for the mechanisms of electromigration, thermomigration and stressmigration were calculated in order to be used in the static analysis as well as the time-dependency analysis. The massflux induced by the concentration gradient within the metallization structure was not considered in this study.

An other important part of this work has consisted in the retrieval of material physical parameters and properties. The physical constants needed to characterise the contribution of the electromigration in aluminum metallization structures have been summarised and taken from the literature, as well as those integrating the contribution of the phenomenon of thermomigration and stressmigration. A wide range of data for each migration phenomena has been found. In order to perform the thermoelectrical and the thermomechanical investigations, the physical material properties have been extracted from existing references in the literature. Moreover, most of them have been taken being temperature-dependent for the Finite Element Analysis due to the large range of temperatures generally appearing when the metallization structures are tested. The physical constants were considered in the static analysis for the determination of the failure location within the metallization structure and were used for the time-dependending simulation of void formation.

The static analysis used for the determination of the failure location induced by electromigration, thermomigration as well as the stressmigration has been performed. The study includes the investigations for a meander structure and a SWEAT structure. Static results like the temperature gradient distribution as well as the thermomechanical induced hydrostatic stress gradient distribution were presented and the results have been compared to previous work for verification. The study of the temperature variation and the mechanical stress deviation with the applied current have been given in order to be used in the reliability modelling. Then, the failure location determination was performed in the investigated metallization structures. The different influences that contribute to the void formation within the structures have been determined with help of the Finite Element Analysis. The failure locations have been successfully determined for the both structures and found in very good agreement with the experimental results. The stressmigration is determined to be the most important effect playing in the degradation of the meander structure due to the high level of test temperature (180°C). On the other hand, the electromigration is found dominant for the SWEAT structure investigated at room temperature.

Then, the time-dependency analysis of metallization structures degradation due to voids formation has been given and a method for their simulation has been proposed. The degradation process has been first observed and interpreted. The interpretation has permitted the extraction of important guidelines for the definition of a simulation method. The details of the method have been exposed in 2-D for simplification and applied in 3-D analysis in order to approach the reality. Next, a method to solve the continuity equation which takes into account the different parameters like the local current density, the temperature and the temperature gradient as well as the hydrostatic stress gradient is exposed and coupled to the Finite Element Model for void simulation. The method has been integrated in an algorithm giving the opportunity to calculate and to predict automatically the void evolution as well as the electrical resistance change of the metallization structure during the void simulation growth. The results obtained for the degradation of the meander structure is found to be in good agreement with experimental observations and verify the suggested method. The results obtained for the SWEAT structure are also found in concordance with those obtained experimentally. In both cases, the investigation of the different mechanisms during the void growth has shown that the electromigration phenomena prevails just before the failure of the electrical interconnect. The variation study of some physical parameters has shown that the value of the activation energy considered in the algorithm can have an important impact on the determination of the calculated TTF. Nevertheless, the gap found between the measured and the calculated lifetime in both cases may come from the value of the self-diffusion coefficient considered as pure aluminum within the simulations, although the metallization structures were fabricated with an aluminum alloy.

The results concerning the temperature gradient and the hydrostatic stress gradient modelling with the applied current density have been integrated in the formula of the massflux divergence. A transformation of the expression has shown a dependence of the massflux divergence with a current density exponent. The calculated expression also shows that the dominant effects appearing during the degradation of the metallization structure can have an important impact on the current density exponent. The dominant degradation phenomena might be influenced by the geometry of the metallization structures, by the thermophysical properties of the different materials used and also by the conditions of use too.

In this work, a simplified method for the prediction of void formation within metallization structures due to the phenomenon of electromigration, thermomigration and

stressmigration has been proposed. The method has been integrated in an algorithm using the Finite Element Method for the calculations of the massflux divergence values and for 3-D void formation simulation. The method also provides the opportunity to make an evaluation of the corresponding lifetime of the considered metallization structures for particular conditions of test. The method has been tested and verified over two metallization structures investigated experimentally with very good results. The program developed during this thesis work should be useful for the design optimisation of chip-level metallization structures reliability improvement and can be combined with experimental investigations. It should also permit the integration of several fabrication process parameters as well as some operating conditions parameters in further reliability study of metallization structures.

Zusammenfassung

In dieser Arbeit wurde die zeitabhängige Simulation der Lochbildung in Metallisierungsstrukturen, die durch induzierte Materialwanderung auftritt vorgestellt. Die zur Lochbildung führenden Degradierungsmechanismen wie Elektromigration, Thermomigration und Stressmigration wurden untersucht. Zwei unpassivierte Metallisierungsstrukturen sind experimentell bei unterschiedlichen Belastungen mittels Stresstests untersucht worden. Die experimentellen Ergebnisse wurden analysiert und interpretiert. Gleichzeitig wurde das Verhalten der Strukturen unter hohen Belastungen mittels Simulation bestimmen. Um die Lochbildung vorhersagen zu können wurden mehrere Hypothesen aus der Analyse der experimentellen Ergebnisse extrahiert und in einen Algorithmus implementiert. Erstmals wurde eine Routine zur zeitabhängigen Berechnung der Lochbildung sowie zur Vorhersage des TTF erstellt. Die Anwendung des Programms war bei beiden Metallisierungsstrukturen erfolgreich.

Im ersten Kapitel wurden die experimentellen Untersuchungen der Zuverlässigkeit von Metallisierungsstrukturen unter starken Belastungen präsentiert. Danach wurden die getesteten Strukturen beschrieben und die in den Simulationen verwendeten Materialeigenschaften angegeben. Desweiteren wurden die verschiedenen Schritte der Lochbildung in der Mäanderstruktur dargestellt. Der TTF in Abhängigkeit von der Stromdichte sowie der Substrattemperatur wurde für die Mäander und die SWEAT Struktur präsentiert. Anschliessend wurden die verschiedenen Diffusionsmechanismen die zu einer Lochbildung führen können vorgestellt. Für den Vergleich mit den Simulationsergebnissen wurden die experimentellen Ergebnisse der beiden Metallisierungsstrukturen dargestellt.

Im zweiten Kapitel wurden die theoretischen Grundlagen der verschiedenen Diffusionsmechanismen im Degradierungsprozesse dargestellt. Das Modell der von der lokalen Stromdichte anhängigen Elektromigration wurde angegeben. Die von den lokalen Temperaturgradienten abhängige Thermomigration, wurde ebenfalls beschrieben. Der durch thermomechanischen Stress induzierte Stressmigration wurde auch dargestellt, die durch die Selbsterwärmung der Metallisierungsstrukturen und der damit verbundene Ausdehnung hervorgerufen wird. Die Kontinuitätsgleichung, die die Zeitabhängigkeit des Phänomens beschreibt, sowie der Zusammenhang zwischen der Veränderung der Atomdichte und der

Divergenz des Massenflusses wurde angegeben. Die Massenflussdivergenzen der verschiedenen Diffusionsmechanismen wurden berechnet. Sie wurden bei der statische Analyse sowie in den zeitabhängigen Untersuchungen der Degradierung verwendet. Der Massenfluss der Konzentrationsgradienten wurde jedoch nicht berücksichtigt.

In einem weiteren Teil dieser Arbeit wurden die Parameter der Elektromigration, der Thermomigration und der Stressmigration sowie die physikalischen Eigenschaften der Materialien zusammengefasst. Die zur Charakterisierung der Elektromigration, der Thermomigration sowie der Stressmigration verwendeten physikalischen Konstanten wurden der Literatur entnommen. Für einige physikalische Parameter wurde ein breites Spektrum von Daten gefunden. Die thermisch-physikalischen Materialeigenschaften wurden ebenfalls der Literatur entnommen und für die FEM Analyse temperaturabhängig berücksichtigt. Der Einfluss einer Variation der Parameter auf die Lebensdauer wurde ebenfalls untersucht.

Eine statische Analyse der Elektromigration, der Thermomigration sowie der Stressmigration wurde zur Bestimmung des Fehlerortes durchgeführt. Die Untersuchung ist anhand einer Mäanderstruktur und einer SWEAT Struktur durchgeführt worden. Ergebnisse wie die Verteilung der Temperaturgradienten sowie die Verteilung der induzierten thermomechanischen hydrostatischen Stressgradienten sind vorgestellt und mit vorherigen Arbeiten verglichen worden. Die Variation der Temperatur und des mechanischen Stress der Metallisierung in Abhängigkeit von der globale Stromdichte wurde untersucht und für die Modellierung der Zuverlässigkeit verwendet. Danach wurde die Bestimmung des Fehlerortes für die untersuchten Metallisierungsstrukturen vorgestellt. Die unterschiedlichen Degradierungseffekte während der Lochbildung wurden mit Hilfe der Finite Element Analyse bestimmt. Der Fehlerort wurde im Vergleich zum experimentellen Ergebnisse in beiden Fälle erfolgreich bestimmt. Aufgrund der Testtemperatur (180°C) ist die Stressmigration als entscheidender Effekt in der Degradierung der Mäander Struktur festgestellt worden. Bei der Untersuchung der SWEAT Struktur, da die Untersuchungen bei Raumtemperatur durchgeführt wurden wurde jedoch die Elektromigration als entscheidende Degradierungsmechanismus festgestellt. Die Differenzierung der verschiedenen Degradierungsmechanismen unter bestimmte Belastungsbedingungen ist bei der Anwendung des entwickeltes Programm möglich.

Im nächsten Kapitel wurde die zeitabhängige Analyse der Lochbildung in den Metallisierungsstrukturen präsentiert. Eine Interpretation der experimentellen Ergebnisse wurde für die Bestimmung des Berechnungsverfahrens verwendet. Die Details der Methode wurden 2-D dargestellt, aber für die 3-D Analyse programmiert und verwendet. Danach wurde eine Methode zur Lösung der Kontinuitätsgleichung in Abhängigkeit von lokalen Parametern wie Stromdichte, Temperatur und Temperaturgradienten sowie hydrostatischen Stressgradient vorgestellt, die mit dem Finite Elemente Modell zur Lochbildungssimulation gekoppelt sein sollte. Die Methode wurde in einen Algorithmus implementiert, und bietet die Möglichkeit die Berechnung der Lochentwicklung durchzuführen. Weiterhin wird die Veränderung des elektrischen Widerstands der Metallisierungsstrukturen während der Lochbildung erhalten. Die gerechnete Lebensdauer für die Mäanderstruktur wurde mit sehr guter Übereinstimmung im Vergleich zu den experimentellen Ergebnissen gefunden. Die Untersuchung der SWEAT Struktur zeigt ebenfalls eine gute Übereinstimmung zwischen Berechnung und Test. Die Variation der physikalischen Parameter zeigt eine grosse Abhängigkeit der gerechnete Lebensdauer von der Aktivierungsenergie E_A . Die Gültigkeit der eingesetzte Methode wurde durch die erfolgreiche Anwendung der zwei getestete Strukturen bestätigt.

Die Modellierung der Temperaturgradienten und des hydrostatischen Stressgradienten in Abhängigkeit von der globalen Stromdichte wurde in einer Formel zur Berechnung der Gesamtmassenflussdivergenz zusammengefasst. Eine Umwandlung diese Gleichung zeigt die Abhängigkeit der Massenflussdivergenz vom Exponent der Stromdichte. Die erhaltene Gleichung zeigt, dass der jeweilige Degradierungsmechanismus einen grossen Einfluss auf den Wert des Exponents haben kann. Ausserdem wird gezeigt, dass sowohl die Geometrie der Metallisierungsstrukturen, als auch die Materialeigenschaften sowie die Betriebsbedingungen einen grossen Einfluss auf den entscheidenden Degradierungsmechanismen hat.

In dieser Arbeit wurde eine einfache Methode zur Vorhersage der Lochbildung in Metallisierungsstrukturen vorgestellt. Die Degradierungsmechanismen wie Elektromigration, Thermomigration sowie Stressmigration wurden dabei berücksichtigt. Die Methode wurde in einen Algorithmus implementiert. Die Berechnung der Massenflussdivergenzen und der 3-D Lochbildungssimulation wurden mittels in Fortran geschriebenen Programmen und der Methode der Finite Elemente (ANSYS) durchgeführt. Zusätzlich bietet die Methode die Gelegenheit die Lebensdauer von Metallisierungsstrukturen für besondere

Belastungsbedingungen zu bewerten. Die Methode wurde mit Hilfe von zwei unterschiedlichen Metallisierungsstrukturen erfolgreich getestet und mit sehr guter Übereinstimmung verifiziert. Das Programm, das während dieser Arbeit entwickelt wurde, kann für die Optimierung des Designs von Metallisierungsstrukturen genutzt werden, und kann mit experimentellen Untersuchungen gekoppelt werden. Die Berücksichtigung mehrerer Parametern der Herstellungsprozesse sowie der Belastungsbedingungen in der Simulation sind für die Untersuchung der Zuverlässigkeit von künftigen Metallisierungsstrukturen von grossem Vorteil.

References

- [1] Blech I.A., Diffusional Back Flow During Electromigration, *Acta Materialia*, Vol. 46, n°11, pp. 3717-3723, 1998.
- [2] Petrescu V., Moushaan A.J., Schoenmaker W., Salm C., Mechanical Stress Evolution and the Blech length: 2-D Simulation of Early Electromigration Effects, *Microelectronics Reliability*, n°38, pp. 1047-1050, 1998.
- [3] Yeo I.-S., Ho P.S. Stress Relaxation and Void Formation in Passivated Al(Cu) Line Structures, *Stress Induced in Metallization: 4th International Workshop*, AIP, pp. 262-276, 1998.
- [4] Lee S.H., Kwon D., The analysis of thermal stress effect on electromigration failure time in Al alloy thin-film interconnects, *Thin Solid Films*, n° 341, pp. 136-139, 1999.
- [5] Trattles J.T., O'Neill A.G., and Mecrow B.C., Computer Simulation of electromigration in thin-film conductors, *Journal of Applied Physics*, Vol. 75, n°12, pp. 7799-7804, 1994.
- [6] Rzepka S., Korhonen M.A., Weber E.R., and Li C.-Y., 3-D Finite Element Simulation of electro and Stress Migration Effects in Interconnect Lines, *Materials Reliability in Microelectronics VII. Symposium*, Pittsburgh, PA, USA: Mater. Res. Soc, pp. 329-335, 1997.
- [7] Sasagawa K., Naito K., Saka M., Abé H., A method to predict electromigration failure of metal lines, *Journal of Applied Physics*, Vol. 86, n° 11, pp. 6043-6051, 1999.
- [8] Bruschi P., Nannini A., Piotta M., Three-dimensional Monte-Carlo simulations of electromigration in polycrystalline thin films, *Computational Material Science* n°17, pp. 299-304, 2000.
- [9] Yu X., Untersuchungen zum Einfluß von mechanischen Stress auf die Migration in Metallisierungsstrukturen integrierter Schaltungen, Ph. D. Thesis, University of Hannover, Germany, 2000.
- [10] Junhui L., Dasgupta A., Failure Mechanism models for material Aging due to Interdiffusion, *IEEE Transactions on Reliability*, Vol. 43, n°1, pp. 2-10, 1994.
- [11] Schreiber H.-U., Grundlagen der Elektrodifusion zur Zuverlässigkeitsverbesserung von Al-Leitbahnen für Hoch integrierte Schaltungen, *Fortschrittberichte VDI Reihe 9 Nr. 54*, Düsseldorf : VDI-Verlag, 1985.
- [12] Huang H.L. and Chang C.-Y., Electromigration mechanisms in Thin-Film conductors, *Chinese Journal of Physics*, Vol. 11, n°1, pp. 18-22, 1973.

- [13] Rosenberg R. and Ohring M., Void Formation and Growth During Electromigration in Thin Films, *Journal of Applied Physics*, Vol. 42, n° 13, pp. 5671-5679, 1971.
- [14] Reiss G. und Schührer H., Elektromigrationsvorgänge, *Physik in unserer Zeit*, 28 Jahrgang, n°2, 1997.
- [15] Aschmoneit E.-K., "Elektronenwind" schädigt Mikrochips, *Elektronik Magazin*, Vol. nr. 3, 1998.
- [16] Christou A., Electro-thermomigration in Al/Si, Au/Si interdigitized test structures, *Journal of Applied Physics*, Vol. 44, n°7, July 1973.
- [17] Trattles J. T., Finite Element Simulation of VLSI Interconnections with application to reliability design optimisation and electromigration modelling, Ph. D. thesis, University of Newcastle, 1993.
- [18] Weide K., Untersuchungen von Stromdichte-, Temperatur- und Massenflußverteilungen in Viastrukturen integrierter Schaltungen, VDI-Verlag, 1994.
- [19] Burkhard E., Messungen des Thermo- und Elektro- transports in Aluminium und Niob, Ph. D. Thesis, University of Berlin, 1993.
- [20] Limoge Y., Electromigration dans l'aluminium, 19ème Colloque de Metallurgie, INSTN, Juin 1976, I.N.S.T.N., C.E.N. Saclay, p. 971, 1976
- [21] Hoebbel H., Ein Computermodell zur Simulation des Einflusses der Kornstruktur auf das Elektromigrationsverhalten von Leiterbahnen in integrierter Schaltkreisen, Ph. D. Thesis, Technical University of Illmenau, Germany, 1994.
- [22] Huang J. M., Yang W., Zhao Z.J., Interconnect Damage by electromigration: experiment and numerical simulation, *Acta Materialia*, Vol. 47, n°1, pp. 89-99, 1999.
- [23] Schoenmaker W., Petrescu V., Modelling electromigration as a fluid-gas system, *Microelectronics Reliability*, Vol. 39, pp. 1667-1676, 1999.
- [24] Shingubara S., Utsunomiya I., Fujii T., Molecular Dynamics simulation of void electromigration under High-Density Electric current stress in an aluminum interconnection, *Electronics and Communications in Japan, Part 2*, Vol. 78, n° 12, pp. 82-95, 1995.
- [25] Dekker J. P. and Lodder A., Calculated Electromigration wind force in face-centered-cubic and body-centered-cubic metals, *Journal of Applied Physics*, Vol. 84, n° 4, pp. 1958-1962, 15 Aug. 1998.
- [26] Christou, A., *Electromigration and electronic device degradation*, Wiley, 1994.
- [27] Van-Gurp G. J. and F. J. du Chatenier, Measurement of Thermomigration in thin metal films, *Thin Solid Films*, n°131, pp. 155-162, 1985.

- [28] Kraft O., Untersuchung und Modellierung der Elektromigrationschädigung in miniaturisierten Aluminium Leiterbahnen, Ph.D. thesis, University of Frankfurt, May 1995.
- [29] Wever H., Elektro-und Thermotransport in Metallen, J.A. Barth Verlag, Leipzig, 1972.
- [30] Ernst D., Froberg G., Kraatz K. H. and Wever H., Bulk Elektro- and Thermotransport in Al, Defect and Diffusion Forum, Vol. 143-147, pp. 1649-1654, 1997.
- [31] Gangulee A. and D'Heurle F.M., Mass Transport during Electromigration in aluminum-magnesium Thin Films, Thin Solid Films, Vol. 25, pp. 317-325, 1975.
- [32] Schreiber H.-U., Activation Energy for the different Electromigration Mechanisms in Aluminum, Solid State Electronics, Vol. 24, pp. 583-589, 1981.
- [33] Hagedorn F.B. and Hall P.M., Right-Angle Bends in thin Strip conductors, Journal of Applied Physics, Vol. 34, n° 1, pp. 128-133, 1963.
- [34] Gupta D. and Ho P. S., Diffusion phenomena in thin films and microelectronics materials, Park-Ridge, N.J.: Noyes Publ., 1998.
- [35] Sasagawa K., Yamauchi T., Saka M., Abe H., Numerical Simulation of electromigration in Angled metal line, Proceedings of the international Symposium on Microsystems, intelligent materials and Robots, pp. 82-95, 1995.
- [36] Kahn H., Thompson C. V., A statistical Characterization of electromigration induced open failures in 2-level metal structures, Mat. Res. Soc. Symp. Proc., Vol. 225, pp. 15-20, 1991.
- [37] Scheonmaker W., Petrescu V., Modeling electromigration as a fluid-gas system, Microelectronics Reliability, Vol. 39, pp. 1667-1676, 1999.
- [38] Scherge M., Electromigration- Simulation and experiment, AIP Conference Proceedings, pp. 290-299, 1994.
- [39] Landhold H., Börnstein R., Materials Properties, New Series III/26, Self-diffusion in solid metallic elements and in aluminum group metals, Physikalisch-Chemische Tabellen, 5. Auflage, J. Springer Verlag, Berlin.
- [40] Jacobs L. C., Verbruggen A. H., Kalkman A. J. and Radelaar S., Electromigration and Diffusion in Short Al-Ni-Cr Lines, Mat. Res. Soc. Symp. Proceedings, Vol. 516, pp. 275-280, 1998.
- [41] De Keukeleire C., Tielemans L. and de Pauw P., High resolution electromigration measurements for reduction of the test time, International Integrated reliability Workshop, pp. 80-85, 1997.

- [42] Kononenko O. V., Matveev V. N., and Field D. P., The Energy of Activation of Electromigration in aluminum Conductors tested by the drift-velocity Method, Russian Microelectronics, Vol. 29, N°5, pp. 316-323, 2000.
- [43] Bravman J. C., Marieb T. N., Loyld J. R. , Korhonen M. A., Copper versus magnesium as an alloying element in aluminum interconnects: effects on electromigration, Materials Reliability in Microelectronics Symposium, pp. 269-274, 1998.
- [44] Igit P.M., Mawby P.A., Investigation of the thermal stress field in a multilevel aluminum metallization in VLSI systems, Microelectronics Reliability, Vol. 40, pp. 443-450, 2000.
- [45] Yu X., Untersuchung zur Zuverlässigkeit von Metallisierungsstrukturen, Diplomarbeit, Institut für Halbleitertechnologie und Werkstoffe der Elektrotechnik der Universität Hannover, 1995.
- [46] Touloukian Y. S., Thermophysical properties of matter, Vol.1&2, Plenum Pub. Cop., 1970.
- [47] Sexana, A.N., Bougeois, M.A., "Thermal Conductivity of Thin Dielectric Films and its Impact on Multilevel metallizations", VMIC Conference, 1993 ISMIC, pp. 251-257.
- [48] Hasse W., "Untersuchungen an SWEAT-Strukturen", intern Bericht, Institut für Halbleitertechnologie und Werkstoffe der Elektrotechnik, University of Hannover, Germany.
- [49] Sakimoto M., Yamaguchi H., Ito T., Fuji T. and Eguchi K., "Temperature Measurement of Al Metallization and the Study of Black's Model in High Current Density", IEEE 33rd annual edition, International Reliability Physics Symposium Proceedings, pp. 333-341, 1995.
- [50] Banerjee K., Thermal Design Guidelines for Future Deep Submicron VLSI Interconnects, text accessible electronically at:
<http://buffy.eecs.berkeley.edu/IRO/Summary/97abstracts/kaustav.2.html>
- [51] Dion M. J., Finite Element Analysis of a SWEAT Structure with a 3-D, Non-linear, Coupled Thermal-Electric Model, Proceedings IEEE 1992, Int. Conference on Microelectronics Test Structures, Vol. 5, March 1992.
- [52] "Intel Processor IV Datasheet, Intel Corporation".
- [53] Dilhaire S., Phan T., Schaub E., Claeys W., Thermomechanical effects in metal lines on integrated circuits analysed with a differential polarimetric interferometer, Microelectronics Reliability, n°38, pp. 1591-1597, 1998.

- [54] Lowry L.E., Tai B.H., Mattila J., and Walsh L.H., Mechanical stress effects on Electromigration voiding in a meandering test Stripe, Materials reliability in Microelectronics III Symposium, Pittsburgh, PA, UAS, pp. 205-210, 1993.
- [55] Giroux F., Gounelle C., Vialle N., Mortini P. and Ghibaudo G., Current and temperature Distribution Impact on Electromigration Failure Location in SWEAT Structure, Proc. IEEE 1994 Int. Conference on Microelectronic Test Structures, Vol. 7, pp. 214-217, 1994.
- [56] ANSYS ®, "User's manuals", Swanson Analysis Systems Inc., Johnson Road, P.O. Box 65, Houston, PA.
- [57] Doan J.C., Bravmann J. C., Flinn A. and Marieb T. N., The Relationship between Resistance changes and void Volume Changes in Passivated Aluminum interconnects, IEEE 37th Annual International Reliability Physics Symposium , San-Diego, California, pp. 206-212, 1999.
- [58] Kraft O., Möckl U.E., and Arzt E., Numerical Simulation of surface Diffusion controlled motion and shape change of electromigration voids, Mat. Res. Soc. Symp. Proc. Vol. 428, pp. 161-165, 1996.
- [59] Sukharev V., LSI Logic Corporation, Milpitas CA, Private communications.
- [60] Grosjean D. E. and Okabayashi H., 1-D Model of current Distribution and Resistance Changes for Electromigration in Layered Lines, IEEE Transactions on Electron Devices, Vol. 44, n° 5, pp. 744-750, May 1997.
- [61] Kondo S, Ogasawara K. and Hinode K., Thermographic analysis of electromigration phenomena in aluminum metallization, Journal of Applied Physics, Vol. 79, n°2, pp. 736-741, 1996.
- [62] Lloyd J. R., Electromigration for designers, text accessible electronically at: <http://www.seeit.simplex.com/udsm/whitepapers/electromigration1/>
- [63] Baugess S., Liu L.H., Dreyer M.L., Griswold M., and Hurley E., The effects of accelerated stress conditions on electromigration Failure Kinetics and Void morphology, Mat. Res. Soc. Symp. Proc. Vol. 428, pp. 93-99, 1996.
- [64] Van-Gurp G. J., Electromigration in Al Films containing Si, Applied Physics Letters, Vol. 19, n°11, 1971.
- [65] Black, J.R. "Aluminum Conductor Failure by Mass Transport", Proc. of 3rd. Int. Conf. On Microelec., München, pp. 141-162, Nov. 1968.

Lebenslauf

Name David André Dalleau
Geburtstag 28.08.1974
Geburtsort Saint-Denis, Réunion.
Staatsangehörigkeit Französisch

1980 - 1984 Grundschule in Le Port, Réunion.

1984 - 1992 Gymnasium Le Port / Saint-Paul, Réunion.
Abschluss: Baccalauréat "E"

1992 - 1998 Studium in Bordeaux, Frankreich

1992/93 Mathématiques Supérieures & Technologiques, Bordeaux

1993/95 Techniker Studium der Elektrotechnik, Fachhochschule Bordeaux
Abschluss: DUT GEII

1995/98 Hauptstudium der Elektrotechnik, Universität Bordeaux

1998 Diplomarbeit am Laboratoire de Microélectronique IXL
Abschlüsse: DEA Electronique & DESS de Microélectronique

Sept.- Nov.1998 Mitarbeiter Industrieprojekt beim FCI (Framatome Connectors
International): Stand der Technik der Mikropackaging Technologien

Seit Jan. 1999 Stipendiat des Graduiertenkollegs: "Vernetzte Entwicklung
umweltgerechter Produkte und Prozesse", und Mitarbeiter am Projekten
am Laboratorium für Informationstechnologie, Universität Hannover